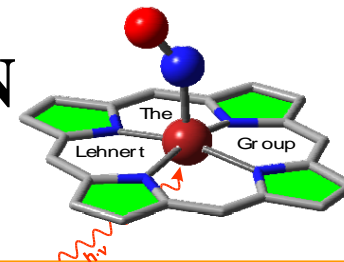




THE UNIVERSITY OF MICHIGAN

DEPARTMENT OF CHEMISTRY

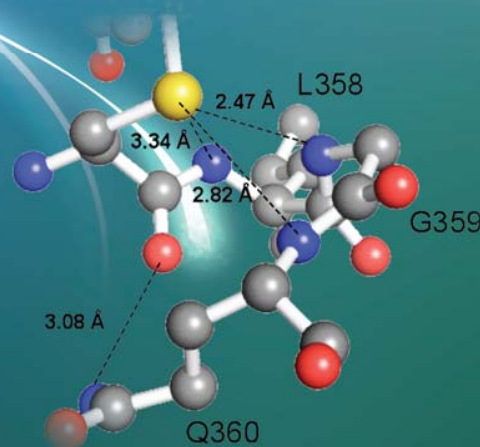
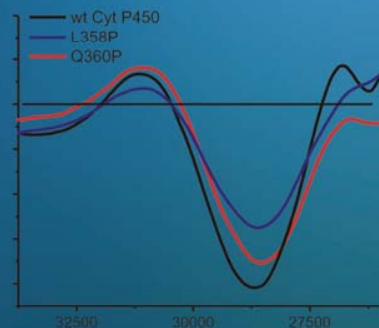
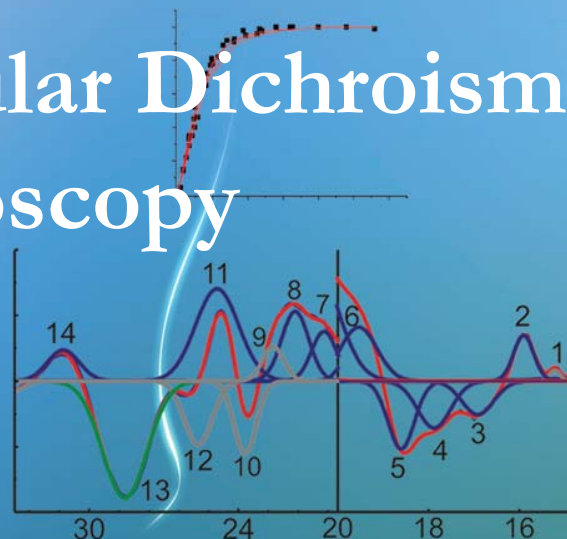


Dr. Nicolai Lehnert

Magnetic Circular Dichroism Spectroscopy



Bioinorganic Workshop
Penn State, 2012

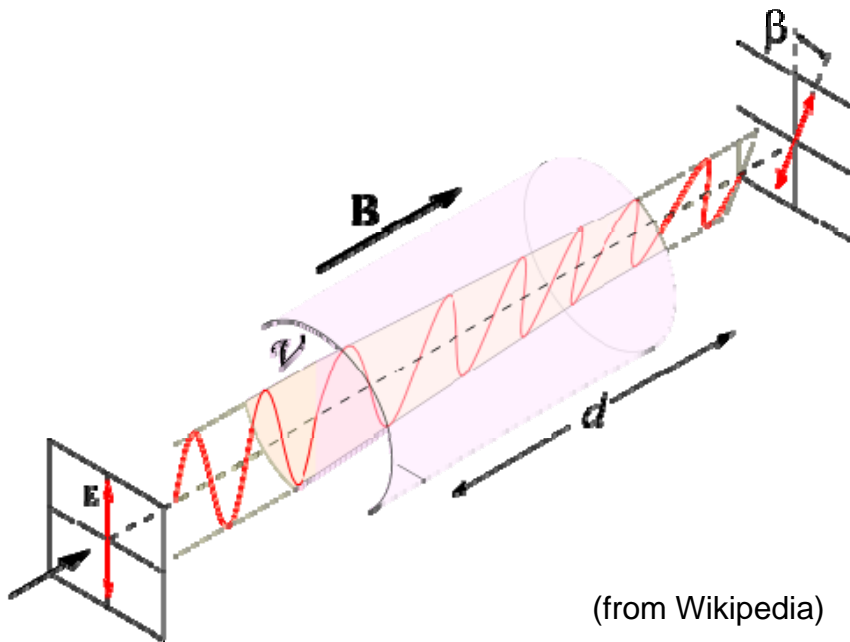


Overview

- The Theory of Magnetic Circular Dichroism
 - The Stephens Equation
 - MCD **A**, **B**, and **C** Terms
 - General Equations for **C** Term Intensity by Neese and Solomon
 - Case Studies: Applications to Metalloporphyrins
 - The Optical Spectra of Metalloporphyrins
 - MCD of Five-Coordinate High-Spin Ferrous Hemes
 - Charge-Transfer Transitions in [Fe(TPP)(Cl)] – a Five-Coordinate High-Spin Ferric Heme
 - Cytochrome P450cam and Cys-Pocket Mutants
-

Faraday Effect

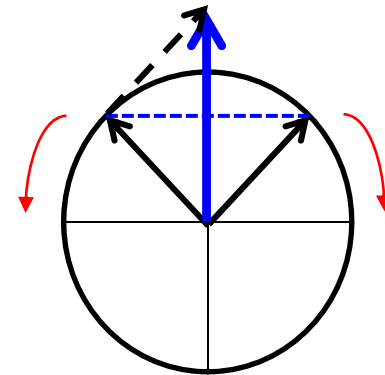
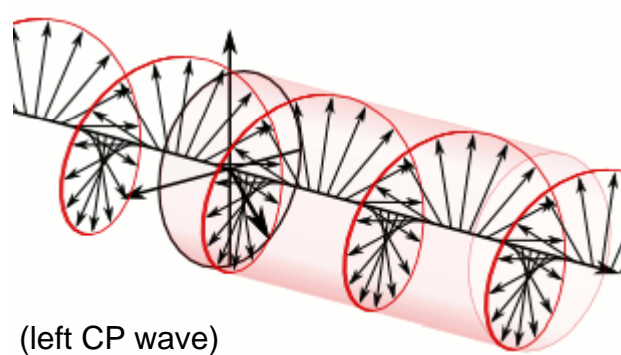
- In 1845 Michael Faraday discovered the magneto-optical effect: the plane of linearly polarized light is rotated when light passes through a medium in the presence of a magnetic field!



M. Faraday

Faraday Effect

- A wave of linearly polarized light is composed of a superposition of two equal-amplitude circularly polarized (CP) waves of opposite handedness and different phase



- Magnetic field causes the left and right circularly polarized waves to propagate through the medium at slightly different speeds
- This causes a phase shift of the circular polarized beams, which rotates the plane of the linearly polarized light

Faraday Effect and Circular Dichroism

- The Faraday effect is caused by the difference in the **real** parts of the refractive indices of the medium for left and right circular polarized light
 - Assumes that light is not absorbed by the medium
 - What if there is a difference in absorption of left and right circular polarized light in the medium?
 - The linearly polarized light becomes elliptically polarized, due to the fact that the left and right circular polarized planes now differ in amplitude!
 - Magnetic Circular Dichroism is caused by the difference in the **imaginary** parts of the refractive indices (absorption) of the medium for left and right circular polarized light
-

CD and MCD

- Both CD and MCD measure the difference, $\Delta\varepsilon$, between the extinction (coefficients) of left and right circular polarized light:

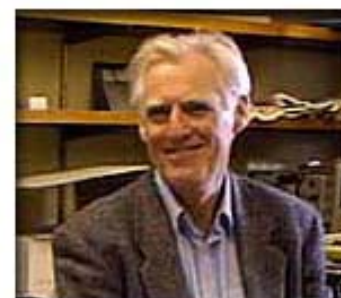
$$\Delta A = A_L - A_R \rightarrow \Delta\varepsilon = \varepsilon_L - \varepsilon_R = \frac{\Delta A}{l \cdot c} \left[\text{M}^{-1} \text{cm}^{-1} \right]$$

A = extinction, absorbance

l = path length [cm]

c = concentration [M]

→ Lambert-Beer Law



P. J. Stephens

- MCD: CD spectroscopy in a longitudinal magnetic field, usually at low temperature (lq. helium)
- Theoretical framework of MCD spectroscopy was first described by Philip J. Stephens (USC) around 1970

Experimental Setup



Lehnert Laboratory, University of Michigan

The Master Equation of MCD

- Fundamental Equation of MCD Spectroscopy:

$$I \sim \text{const} \cdot \left[\mathbf{A}_1 \left(\frac{-\partial f(E)}{\partial E} \right) + \left(\mathbf{B}_0 + \frac{\mathbf{C}_0}{kT} \right) f(E) \right] \cdot \beta \cdot \mathbf{B}$$

$E = h \cdot \nu$ (energy of light)

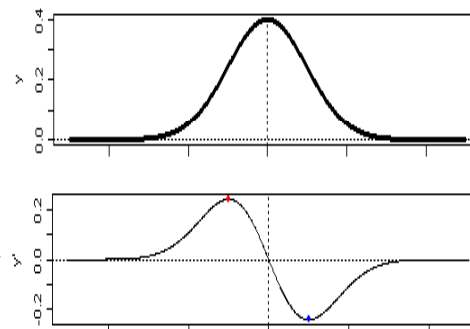
$f(E)$ = absorption band shape

$\frac{-\partial f(E)}{\partial E}$ = derivative band shape

$\mathbf{A}_1, \mathbf{B}_0, \mathbf{C}_0 \rightarrow$ MCD $\mathbf{A}, \mathbf{B}, \mathbf{C}$ Terms

β = Bohr magneton ($9.27402 \cdot 10^{-24}$ J/T)

B = magnetic flux density [T]



The Master Equation of MCD

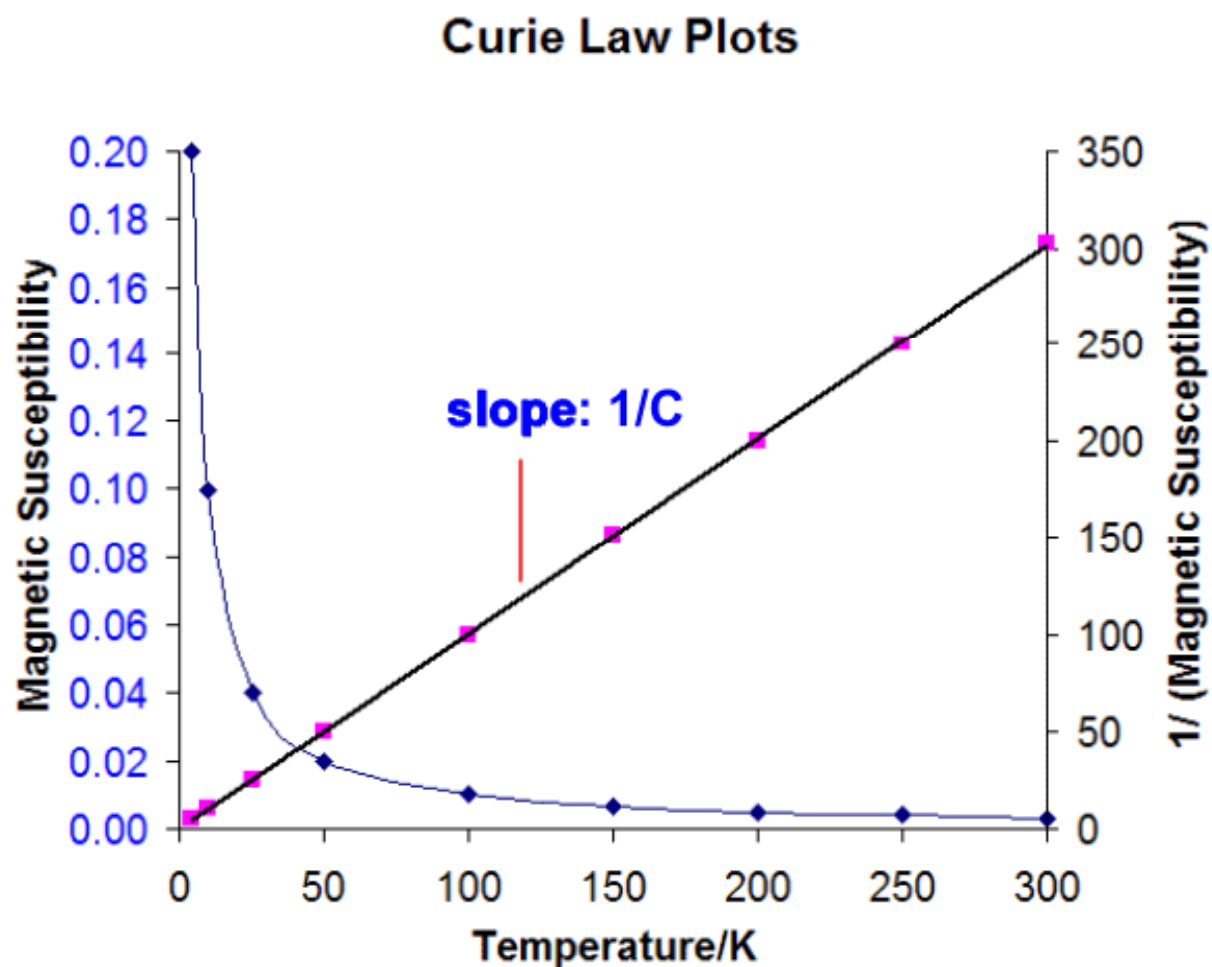
- Fundamental Equation of MCD Spectroscopy:

$$I \sim \text{const} \cdot \left[\mathbf{A}_1 \left(\frac{-\partial f(E)}{\partial E} \right) + \left(\mathbf{B}_0 + \frac{\mathbf{C}_0}{kT} \right) f(E) \right] \cdot \beta \cdot \mathbf{B}$$

- MCD intensity is linear with the magnetic field
- \mathbf{C} term intensity is temperature-dependent:

$$I \sim \frac{\mathbf{C}_0}{kT} \cdot \beta \cdot \mathbf{B} \quad \rightarrow \text{Curie Law} \quad \rightarrow \quad \chi_{\text{mol}} = \frac{\mathbf{C}}{T}$$

The Curie Law



$$\chi_{\text{mol}} = \frac{C}{T}$$

The Master Equation of MCD

- Fundamental Equation of MCD Spectroscopy:

$$I \sim \text{const} \cdot \left[\mathbf{A}_1 \left(\frac{-\partial f(E)}{\partial E} \right) + \left(\mathbf{B}_0 + \frac{\mathbf{C}_0}{kT} \right) f(E) \right] \cdot \beta \cdot \mathbf{B}$$

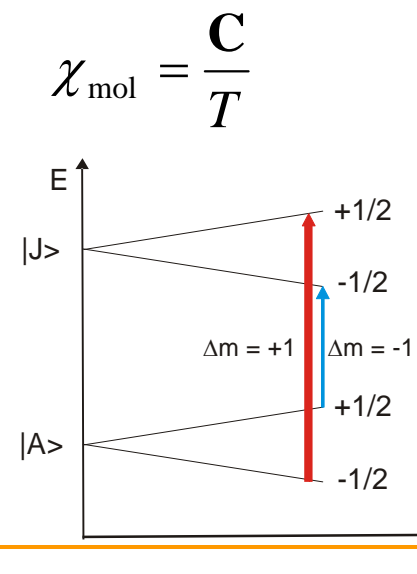
- MCD intensity is linear with the magnetic field
- \mathbf{C} term intensity is temperature dependent:

$$I \sim \frac{\mathbf{C}_0}{kT} \cdot \beta \cdot \mathbf{B} \quad \rightarrow \text{Curie Law} \quad \Rightarrow \quad \chi_{\text{mol}} = \frac{\mathbf{C}}{T}$$

- MCD Selection Rule:

Left Circular Polarized Light (LCP): $\Delta m = +1$

Right Circular Polarized Light (RCP): $\Delta m = -1$



The A Term Mechanism

- Requirement: **degenerate excited states**
- Here: transition from $|A\rangle \rightarrow |J\rangle$, magnetic field along the z direction:

$$A_1^{(z)} = \frac{1}{|d_A|} \sum \left(\overbrace{\langle J | \underline{L}_z + 2\underline{S}_z | J \rangle - \langle A | \underline{L}_z + 2\underline{S}_z | A \rangle}^{\text{Zeeman part}} \times \left(\overbrace{\left| \langle A | \underline{\mu}_- | J \rangle \right|^2 - \left| \langle A | \underline{\mu}_+ | J \rangle \right|^2}^{\text{Electric dipole part}} \right) \right)$$

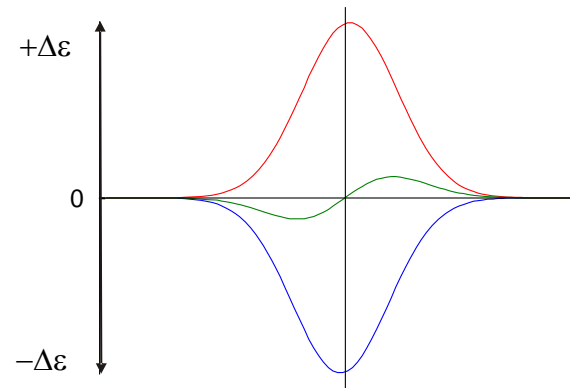
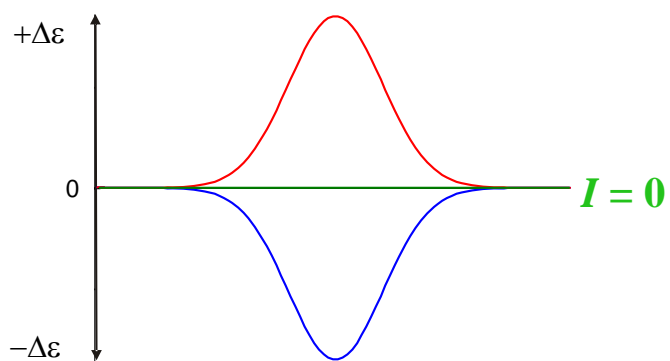
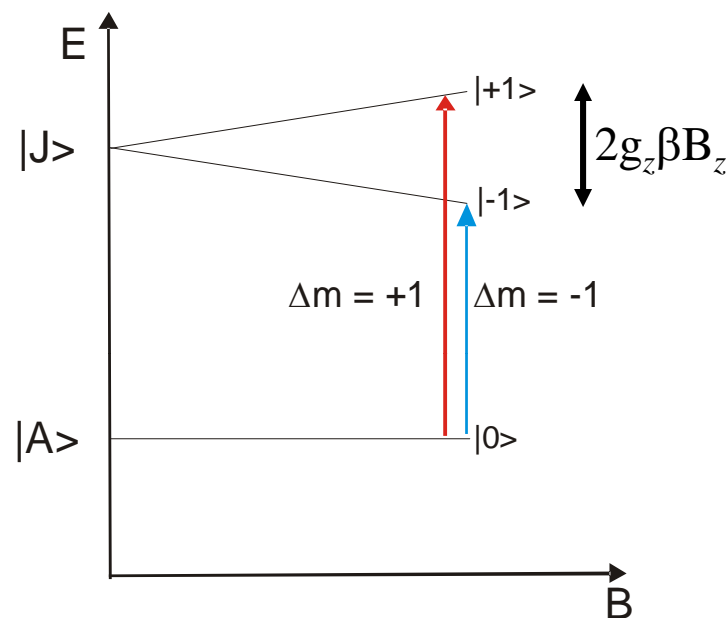
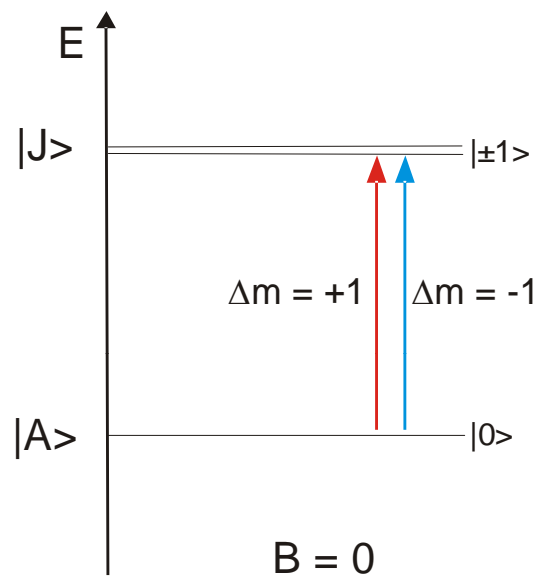
$1/|d_A|$ = degeneracy of the ground state

$\underline{L}_z + 2\underline{S}_z$ = Zeeman operator

$\underline{\mu}_\pm = \frac{1}{\sqrt{2}} (\underline{\mu}_x \mp i \underline{\mu}_y)$ = electric dipole operators for LCP ($\underline{\mu}_+$)
and RCP ($\underline{\mu}_-$)

→ with magnetic field along the z axis, transitions have to be x, y polarized!

The A Term Mechanism



 Works for diamagnetic compounds!

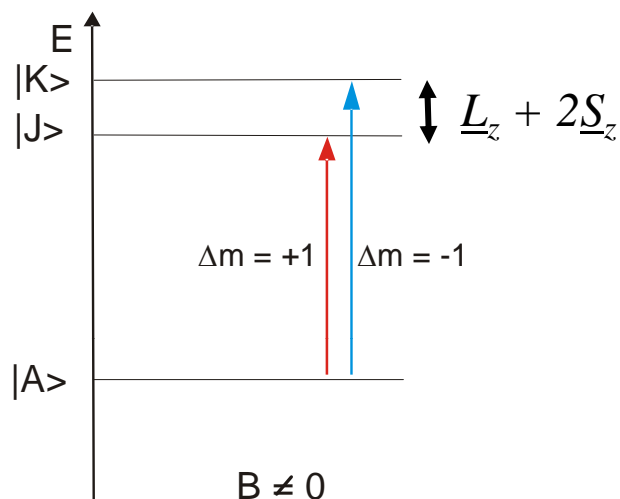
The **B** Term Mechanism

- Requirement: **magnetic-field induced mixing between energetically close states**
- Here: transition from $|A\rangle \rightarrow |J\rangle$, magnetic field along the z direction:

$$\mathbf{B}_0^{(z)} = \frac{2}{|d_A|} \text{Re} \left[\overbrace{\sum_{K \neq J} \frac{\langle J | \underline{L}_z + 2\underline{S}_z | K \rangle}{\Delta E_{KJ}}}_{\text{Zeeman part}} \times \overbrace{\left(\langle A | \underline{\mu}_- | J \rangle \langle K | \underline{\mu}_+ | A \rangle - \langle A | \underline{\mu}_+ | J \rangle \langle K | \underline{\mu}_- | A \rangle \right)}^{\text{Electric dipole part}} \right. \\
 \left. + \sum_{K \neq A} \frac{\langle K | \underline{L}_z + 2\underline{S}_z | A \rangle}{\Delta E_{KA}} \times \left(\langle A | \underline{\mu}_- | J \rangle \langle J | \underline{\mu}_+ | K \rangle - \langle A | \underline{\mu}_+ | J \rangle \langle J | \underline{\mu}_- | K \rangle \right) \right]$$

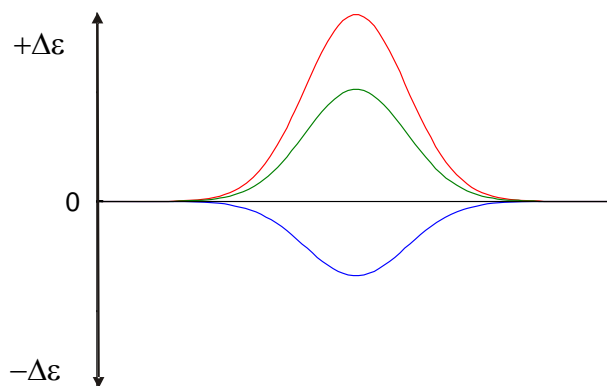
- Two possibilities: either field-induced mixing of the excited state, $|J\rangle$, or the ground state, $|A\rangle$, with the auxiliary state $|K\rangle$ (\rightarrow two parts of the Eqn.)
- **B** terms scale with ΔE , are usually weak!

The **B** Term Mechanism



- Since the transitions $|A\rangle \rightarrow |J\rangle$ and $|A\rangle \rightarrow |K\rangle$ generally have different transition dipole moments, the two contributions do not cancel, leading to an absorption band shape, $f(E)$, for the **B** term

- Both **A**- and **B**-term intensity is linear with field: $I \sim \text{const} \cdot \beta \cdot B$



➡ Works for diamagnetic compounds!

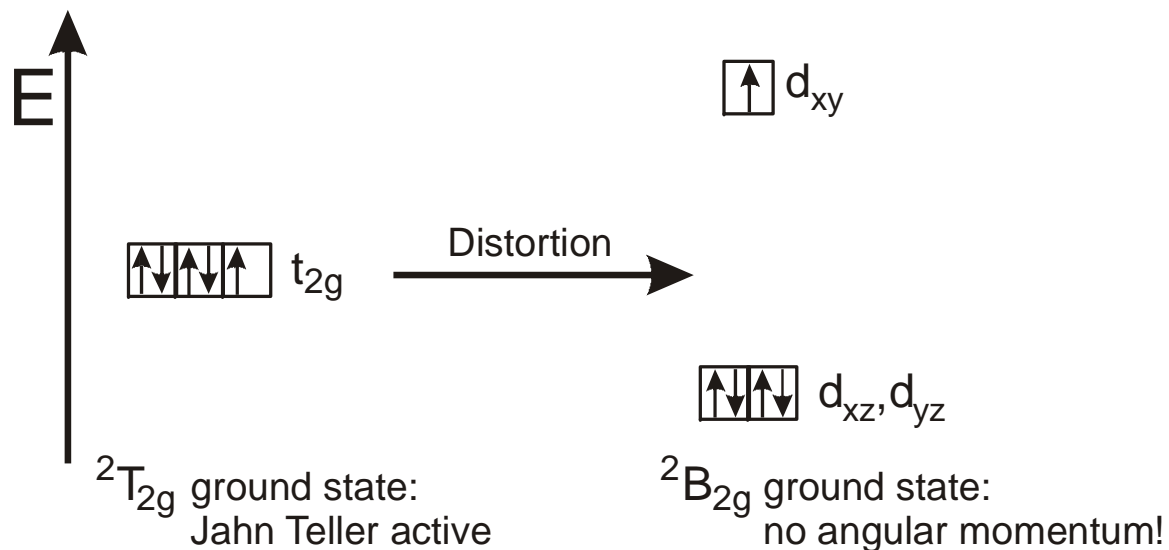
The C Term Mechanism

- Requirement: **non-degenerate ground state**
 - Here: transition from $|A\rangle \rightarrow |J\rangle$, magnetic field along the z direction:
-

The C Term Mechanism

- Requirement: **non-degenerate ground state**
- Jahn-Teller Effect quenches angular momentum (degeneracy) of the ground state:

Example: low-spin Fe(III)

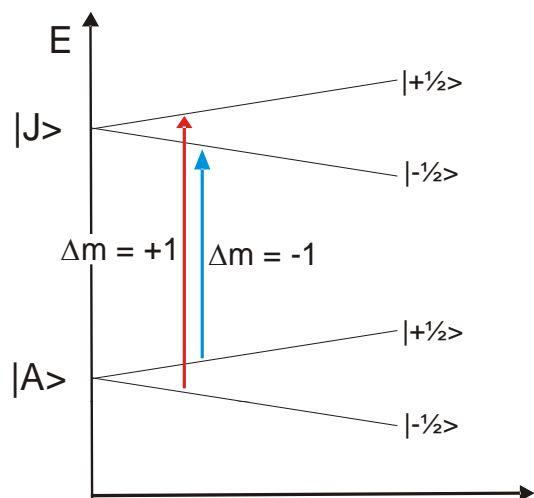


The C Term Mechanism

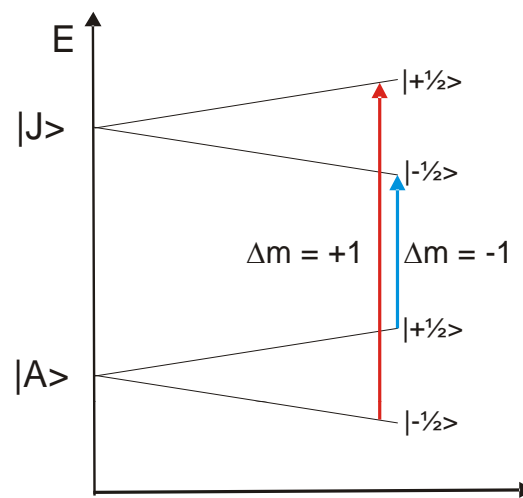
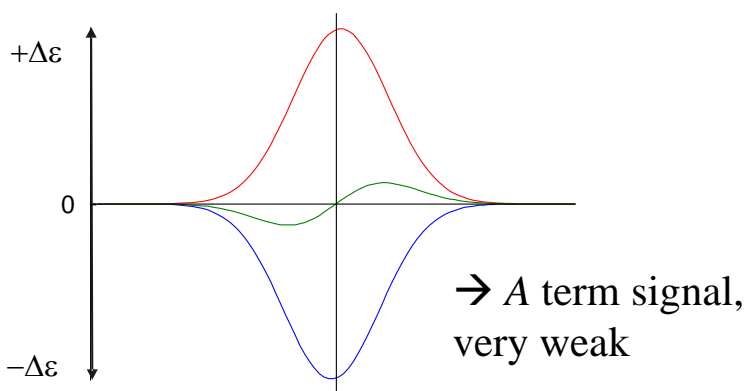
- Requirement: **non-degenerate ground state**
- Due to Jahn-Teller Effect, this is (usually) spin-degeneracy \rightarrow paramagnetic complexes!
- Here: transition from $|A\rangle \rightarrow |J\rangle$, magnetic field along the z direction:

$$C_0^{(z)} = -\frac{1}{|d_A|} \sum \overbrace{\langle A | \underline{L}_z + 2\underline{S}_z | A \rangle}^{\text{Zeeman part}} \times \overbrace{\left(\left| \langle A | \underline{\mu}_{--} | J \rangle \right|^2 - \left| \langle A | \underline{\mu}_{-+} | J \rangle \right|^2 \right)}^{\text{Electric dipole part}}$$

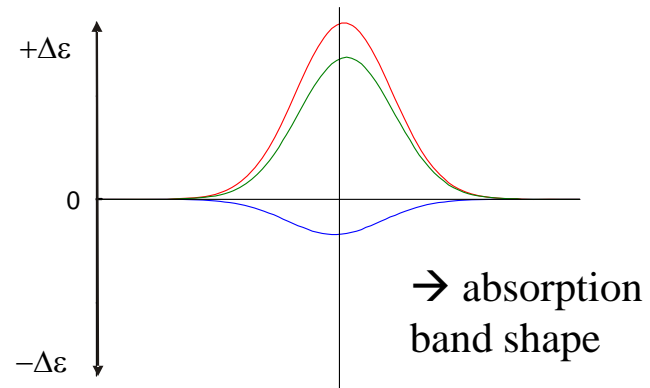
The C Term Mechanism



Small B and/or high T :
Both spin sublevels of the ground state are equally populated



Large B and/or low T :
The $|+1/2\rangle$ spin sublevel of the ground state is becoming depopulated



Lehnert, DeBeer George & Solomon, *Curr. Op. Chem. Biol.* **2001**, 5, 173-184
Solomon, Pavel, Loeb & Campochiaro, *Coord. Chem. Rev.* **1995**, 144, 369-460

The **C** Term Mechanism

- **C** terms are temperature- and field-dependent
- **C** terms **saturate** at low T and high B when the higher spin sublevels of the ground state become completely depopulated (see later)
- At lq. helium temperature: **C** terms are 2 – 3 orders of magnitude more intense than **A** and **B** terms
- For systems with orbitally non-degenerate ground and excited states, $|A\rangle$ and $|J\rangle$, spin-orbit coupling (SOC) must exist in order for MCD intensity to arise
- Since SOC is large for metals, but small for light elements (C, N, O, etc.), **C** term intensity scales with metal contribution: $I(d-d) > I(CT) \gg I(\pi \rightarrow \pi^*, \text{ligand})$

The $S = 1/2$ System

$$C_0 = -\frac{1}{6} \sum_{u,v,w} \varepsilon_{uvw} \mathbf{g}_w \left[\sum_{K \neq A, J} \frac{(\vec{M}_u^{KA} \times \vec{M}_v^{AJ}) \cdot \bar{L}_w^{KJ}}{\Delta E_{KJ}} + \frac{(\vec{M}_u^{AJ} \times \vec{M}_v^{JK}) \cdot \bar{L}_w^{KA}}{\Delta E_{KA}} \right]$$

$(u, v, w) = (x, y, z)$; $\varepsilon_{uvw} \rightarrow$ 3-dimensional orthogonality

\vec{M}_u^{KA} = transition dipole moment for the transition $|A\rangle \rightarrow |K\rangle$ in direction u :

$$\langle \Psi_K | \underline{\mu}_u | \Psi_A \rangle$$

$\bar{L}_w^{KJ} = \text{IM} \langle \Psi_K | \underline{H}_{SOC}^w | \Psi_J \rangle$ = reduced SOC matrix element between states $|K\rangle$ and $|J\rangle$ in direction w , and

$$\underline{H}_{SOC}^w = \sum_A \xi(\mathbf{r}_A) \mathbf{l}_{-A}(A)$$

(sum over all atoms, A , of the system)

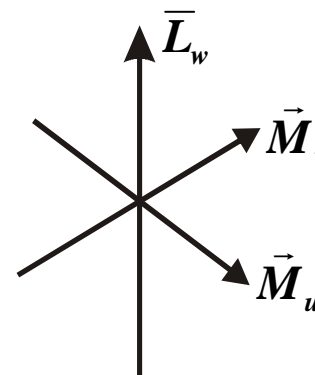
\rightarrow SOC required for MCD C term intensity!

The $S = 1/2$ System

$$C_0 = -\frac{1}{6} \sum_{u,v,w} \varepsilon_{uvw} g_w \left[\sum_{K \neq A, J} \frac{(\vec{M}_u^{KA} \times \vec{M}_v^{AJ}) \cdot \bar{L}_w^{KJ}}{\Delta E_{KJ}} + \frac{(\vec{M}_u^{AJ} \times \vec{M}_v^{JK}) \cdot \bar{L}_w^{KA}}{\Delta E_{KA}} \right]$$

$(\vec{M}_u \times \vec{M}_v) \cdot \bar{L}_w \neq 0$ requires two states with orthogonal transition dipole moments that are spin-orbit coupled in the remaining third direction in space!

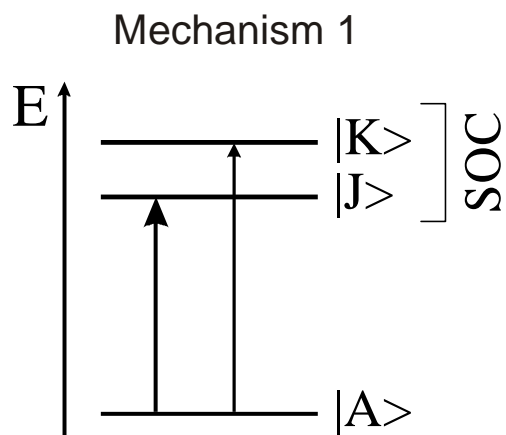
→ Very strict selection rule!



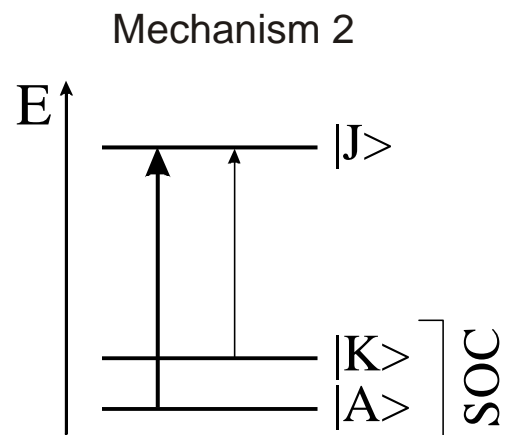
The $S = 1/2$ System

$$C_0 = -\frac{1}{6} \sum_{u,v,w} \varepsilon_{uvw} \mathbf{g}_w \left[\sum_{K \neq A, J} \frac{\overbrace{\left(\vec{M}_u^{KA} \times \vec{M}_v^{AJ} \right) \cdot \vec{L}_w^{KJ}}^{\text{Mechanism 1}}}{\Delta E_{KJ}} + \frac{\overbrace{\left(\vec{M}_u^{AJ} \times \vec{M}_v^{JK} \right) \cdot \vec{L}_w^{KA}}^{\text{Mechanism 2}}}{\Delta E_{KA}} \right]$$

Two mechanisms for MCD C term intensity:

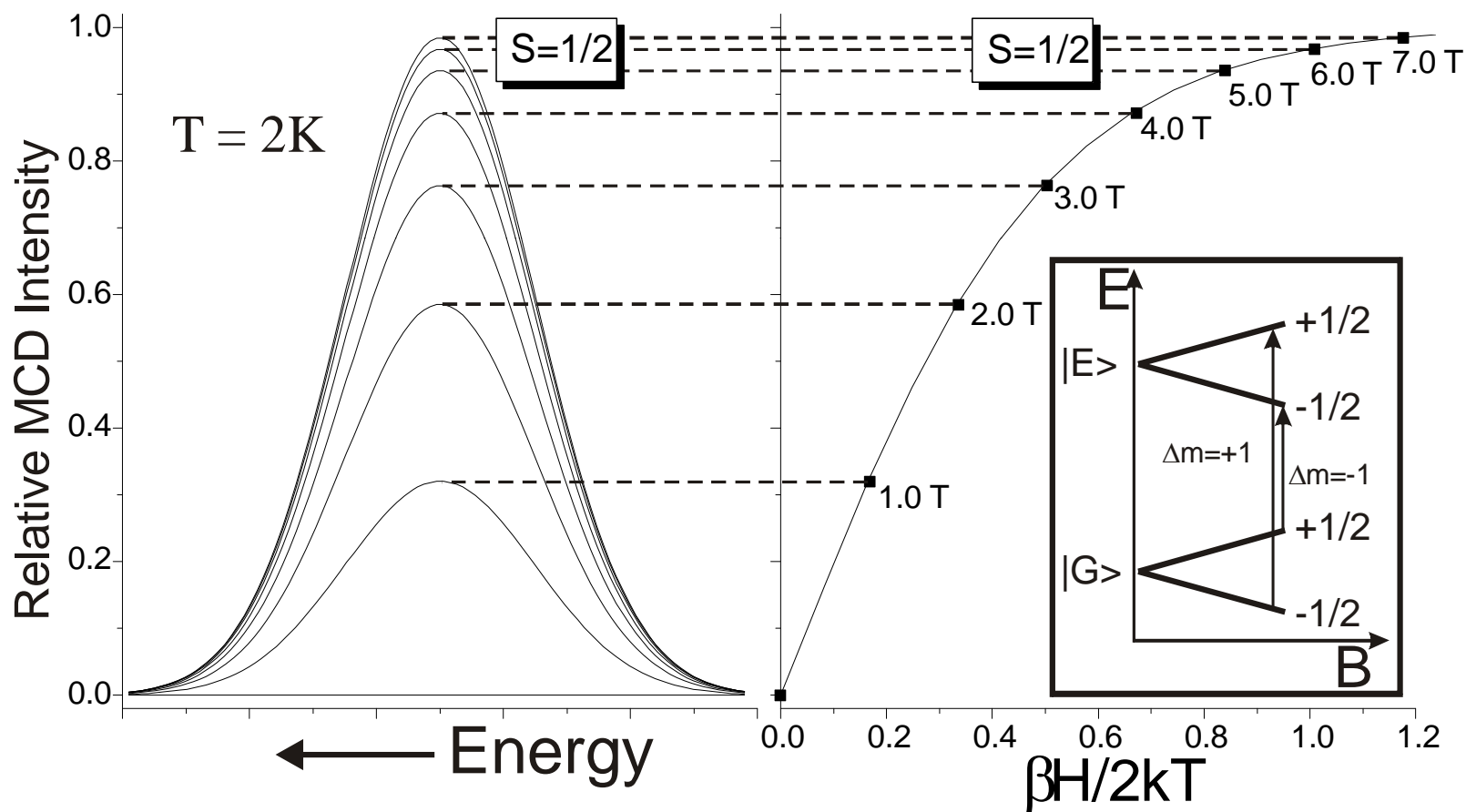


$$I^{MCD} \sim \Delta_{KJ}^{-1} \cdot \left(\vec{M}_u^{AJ} \times \vec{M}_v^{AK} \right) \cdot \vec{L}_w^{KJ}$$



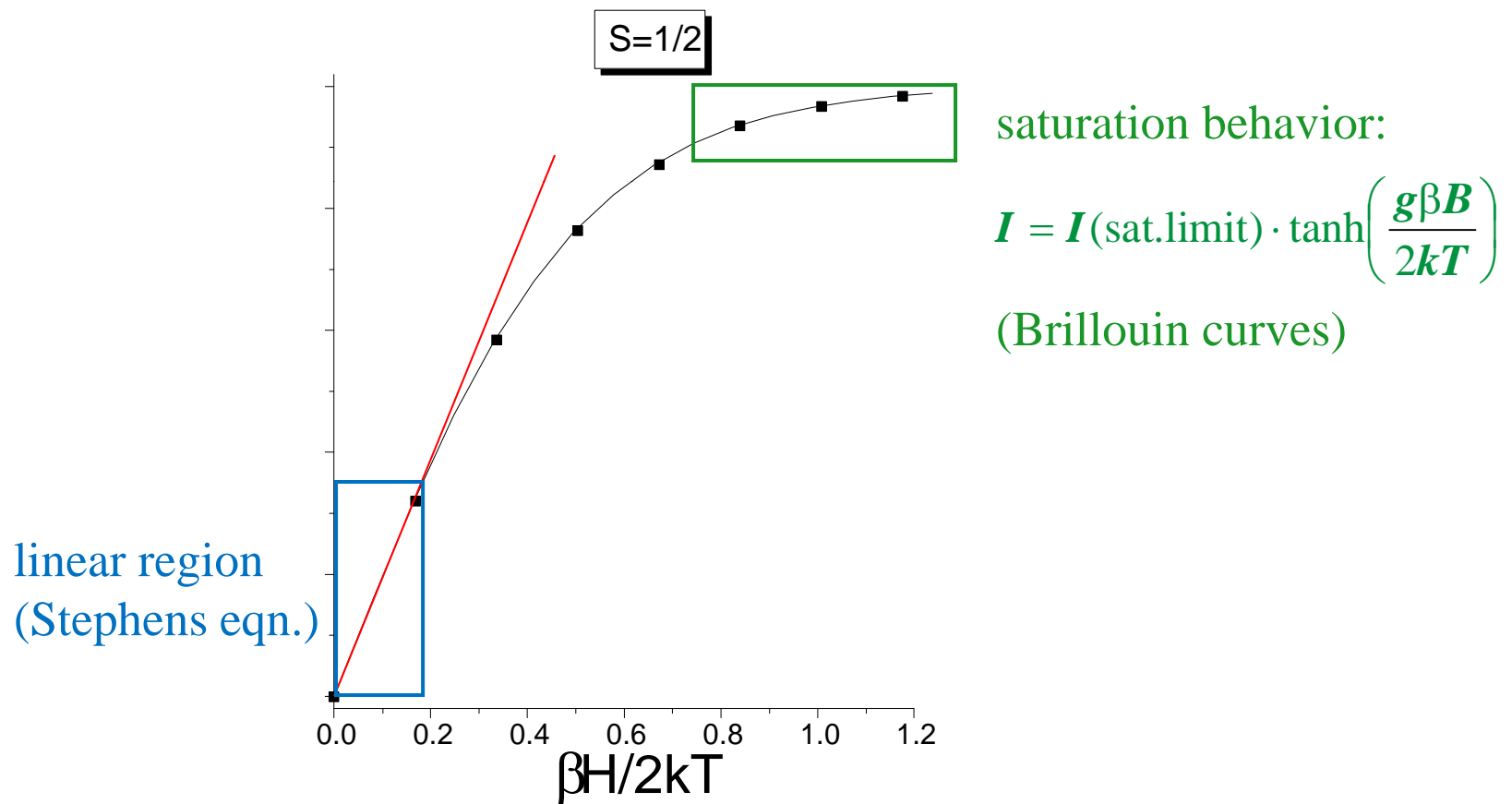
$$I^{MCD} \sim \Delta_{KA}^{-1} \cdot \left(\vec{M}_u^{KJ} \times \vec{M}_v^{AJ} \right) \cdot \vec{L}_w^{KA}$$

MCD Spectrum of the $S = 1/2$ System



MCD Spectrum of the $S = 1/2$ System

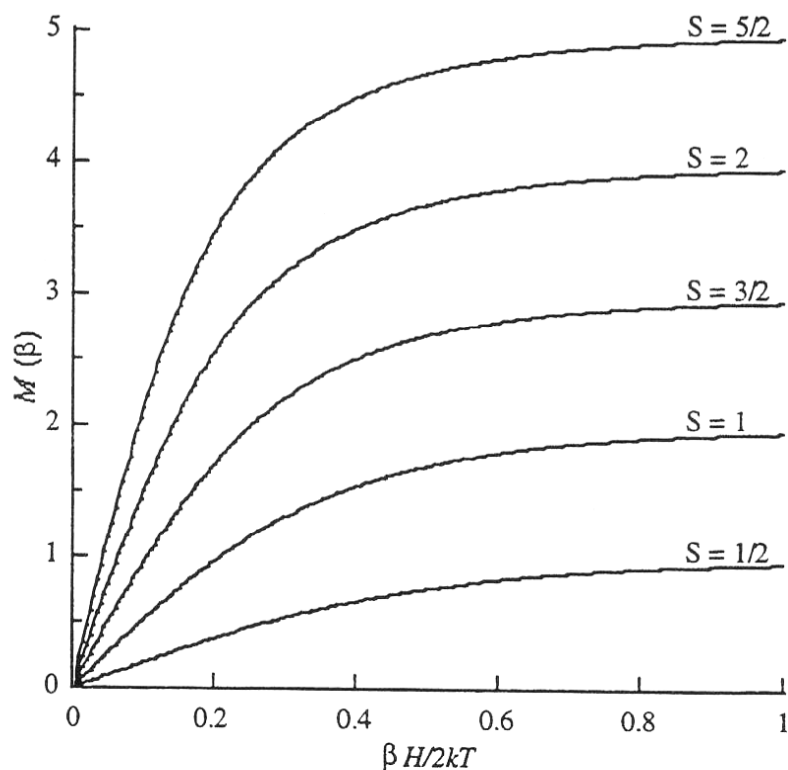
- **C** term saturation magnetization curve, optically detected!



Brillouin Curves: The Rise...

Saturation Magnetization Curves (usually measured by SQUID)

$$M(\beta) = N_g \cdot S \cdot \left[\frac{2S+1}{2S} \coth\left(\frac{2S+1}{2S} \cdot X\right) - \frac{1}{2S} \coth\left(\frac{1}{2S} \cdot X\right) \right] \quad X = \frac{\beta B}{2kT}$$



How to determine the total spin S of your compound?

Susceptibility:

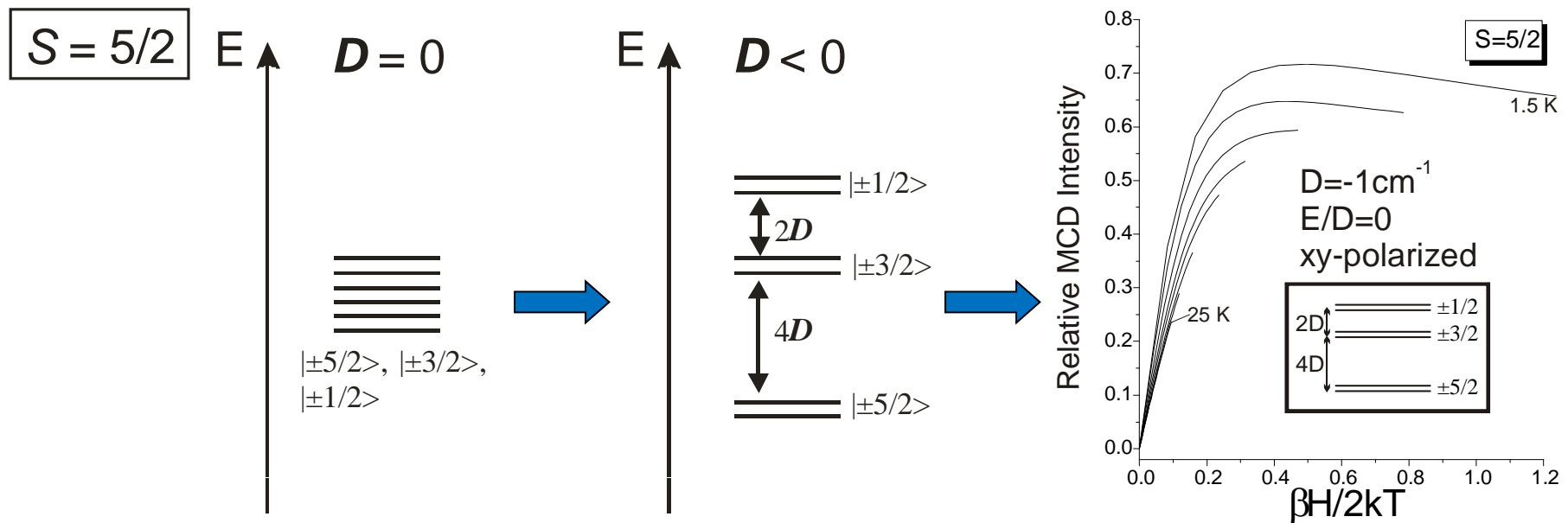
“Height” (Magnetization) \sim total spin S

MCD:

“Height” (MCD intensity) arbitrary, but
Slope \sim total spin S

Brillouin Curves: ... and Fall

- Problem: Brillouin equation assumes that all $2S + 1$ spin sublevels of the ground state are degenerate!
- This is generally **not** the case due to zero-field splitting (ZFS) \rightarrow data show 'nested' magnetization curves for different T that do not superimpose:



MCD Spectrum of the $S > 1/2$ System

$$I = \frac{\gamma}{4\pi \cdot S} \int_0^\pi \int_0^{2\pi} \sum_i N_i \left(l_x \langle S_x \rangle_i M_{yz}^{\text{eff}} + l_y \langle S_y \rangle_i M_{xz}^{\text{eff}} + l_z \langle S_z \rangle_i M_{xy}^{\text{eff}} \right) \sin(\theta) d\theta d\phi$$



F. Neese

Σ_i = sum over all the spin sublevels Θ_i of the ground state (from a Spin Hamiltonian calculation); these might not be pure $|M_S\rangle$ functions:

$$\Theta_i = \sum_{j=1}^N c_j \cdot |M_S\rangle_j \quad (\text{ground state with } N = 2S + 1 \text{ spin functions})$$

N_i = Boltzmann population of Θ_i

$\langle S \rangle_i$ = Spin expectation value for Θ_i : $\langle \Theta_i | \underline{S} | \Theta_i \rangle$

l_x, l_y, l_z : relative orientation of the magnetic field to the molecular coord. system

M_{yz}^{eff} = effective transition dipole moment products:

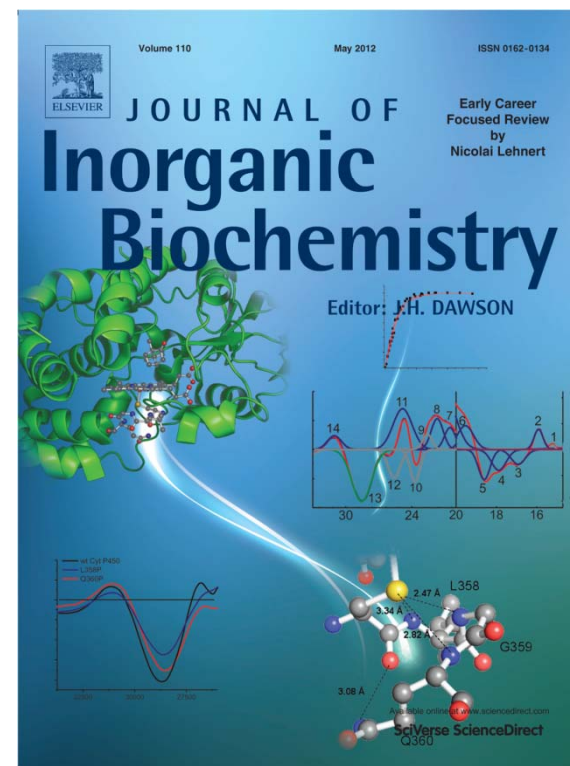
$$M_{yz}^{\text{eff}} = \frac{(\vec{M}_y^{\text{KA}} \times \vec{M}_z^{\text{AJ}}) \cdot \vec{L}_x^{\text{KJ}}}{\Delta E_{\text{KJ}}}$$

→ Polarizations of electronic transitions can be obtained from a fit of the saturation magnetization curves!

→ $S = 1/2$ equation is a special case of this general equation

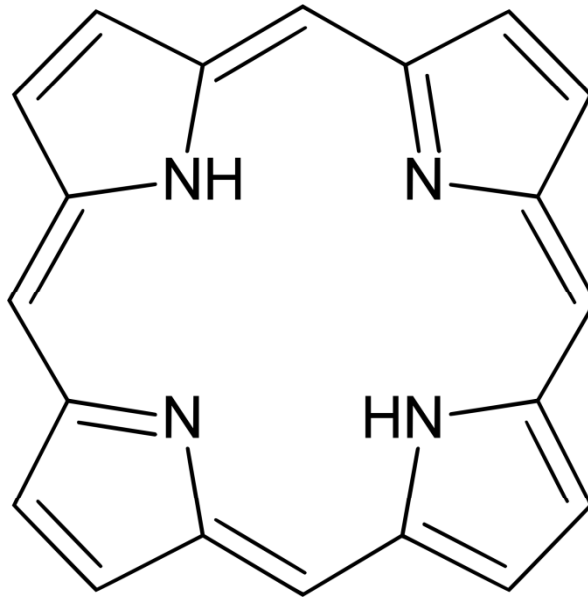
Case Studies: Application to Metalloporphyrins

Lehnert, *J. Inorg. Biochem.* **2012**, *110*, 83-93



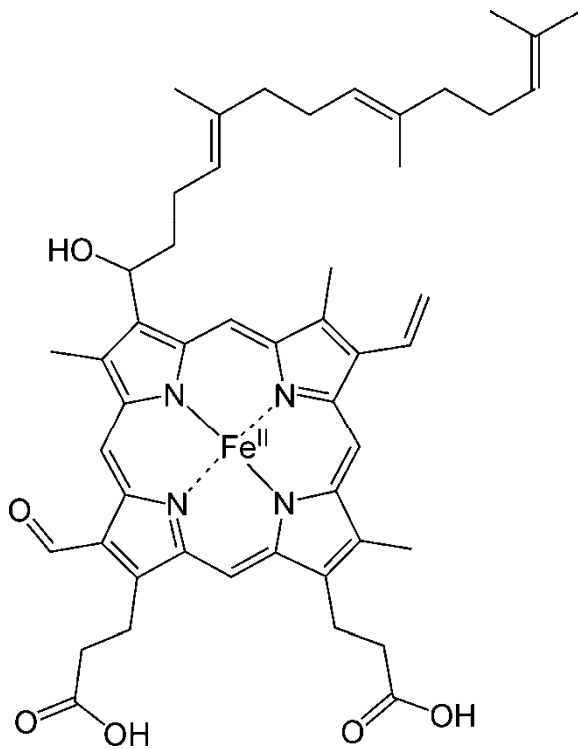
The Heme Cofactor

- The aromatic core of the porphyrin ligand



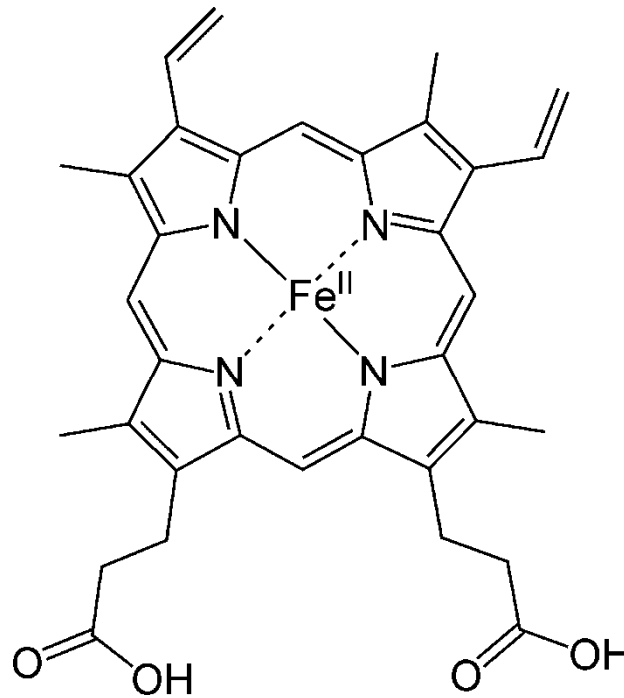
The Heme Cofactor

- Different versions of biological hemes



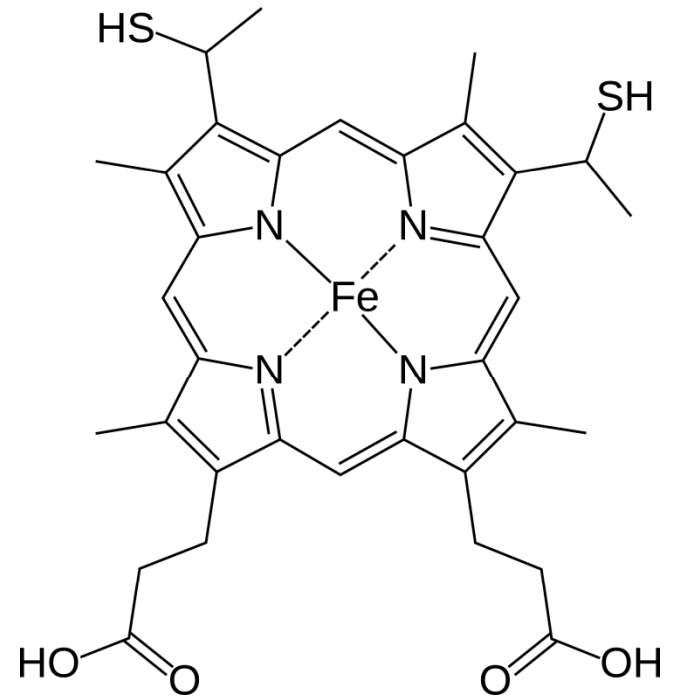
Heme a

(electron transfer)



Heme b (protoporphyrin IX)

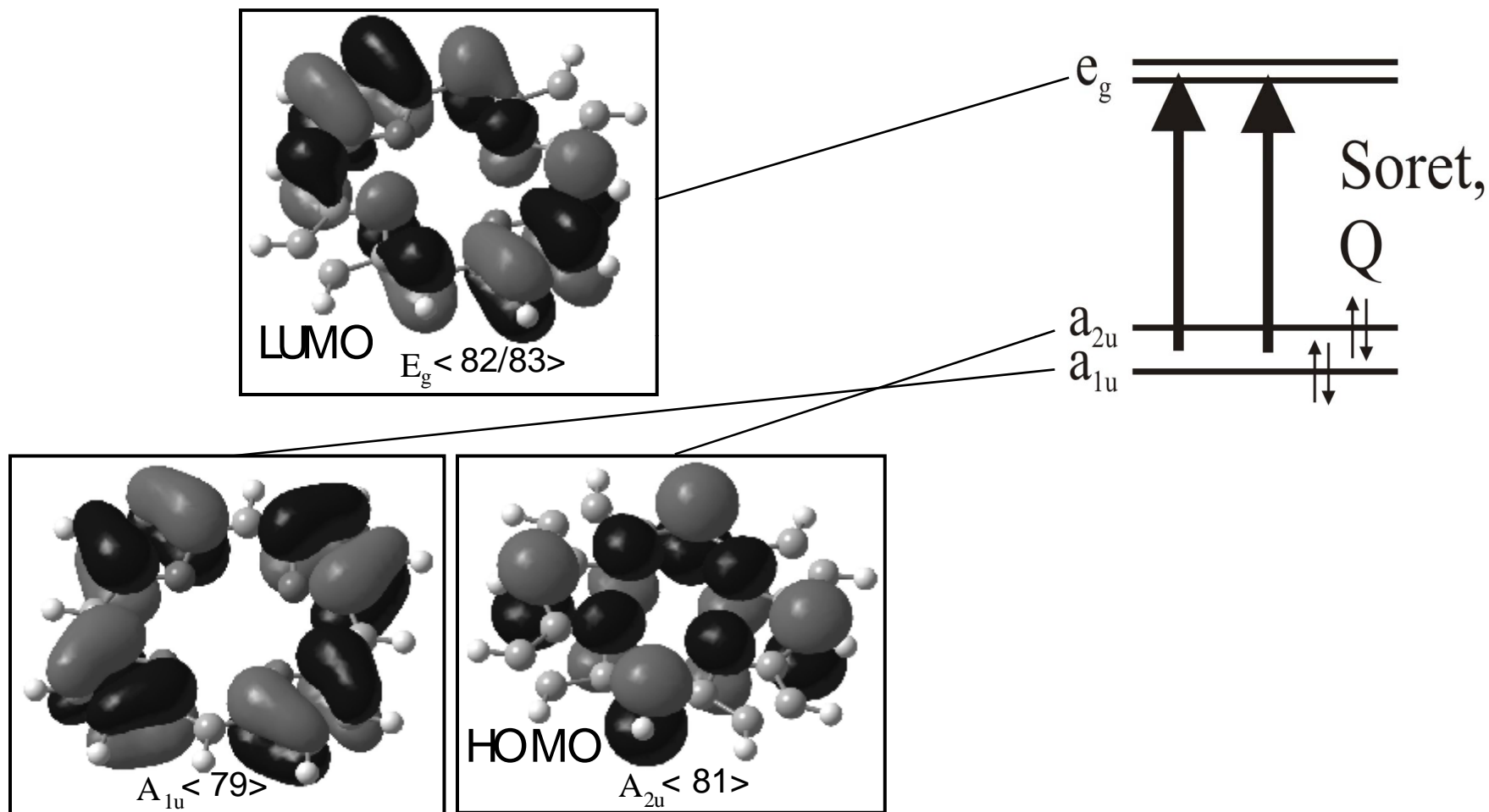
(globins, Cyt. P450s, etc.)



Heme c

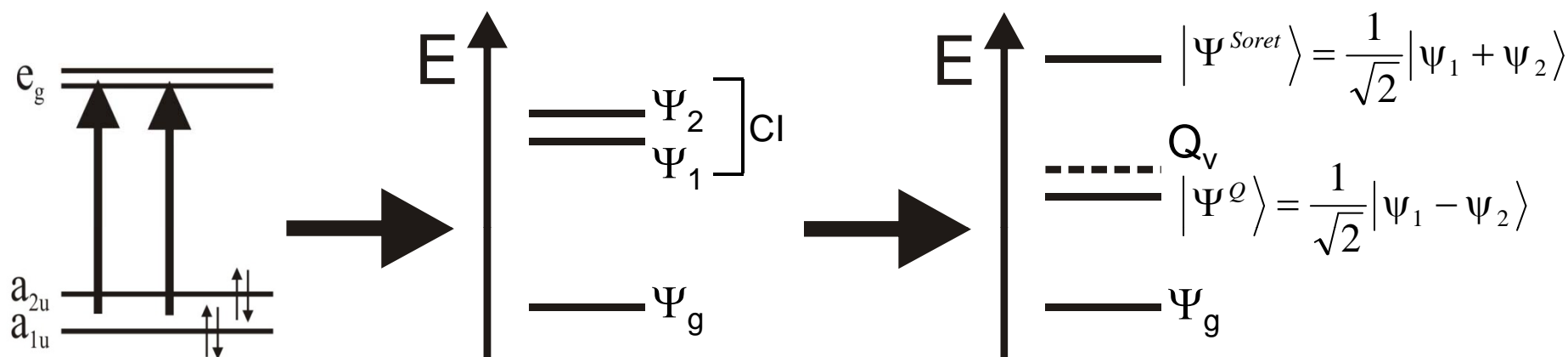
(Cyt. c, electron transfer)

Gouterman's Four Orbital Model



M. Gouterman, in *The Porphyrins*, Vol. III, Part A (Ed.: D. H. Dolphin), Academic Press, New York, 1979, pp. 1-156

Gouterman's Four Orbital Model

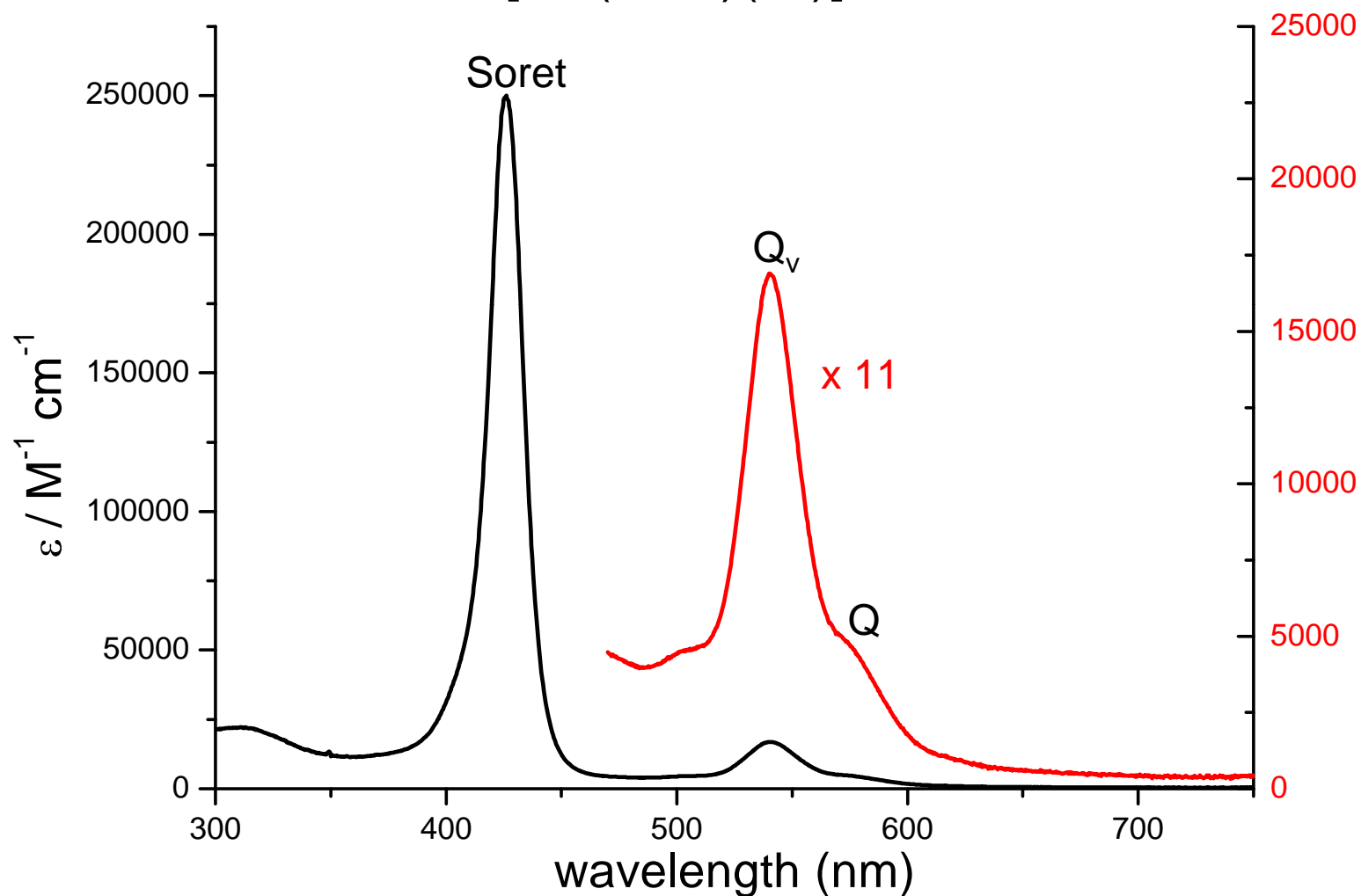


- both excited states Ψ_1 and Ψ_2 that result from the $a_{1u} \rightarrow e_g$ and $a_{2u} \rightarrow e_g$ excitation have E_u -symmetry:
 $(a_{1u} \times e_g = a_{2u} \times e_g = E_u)$

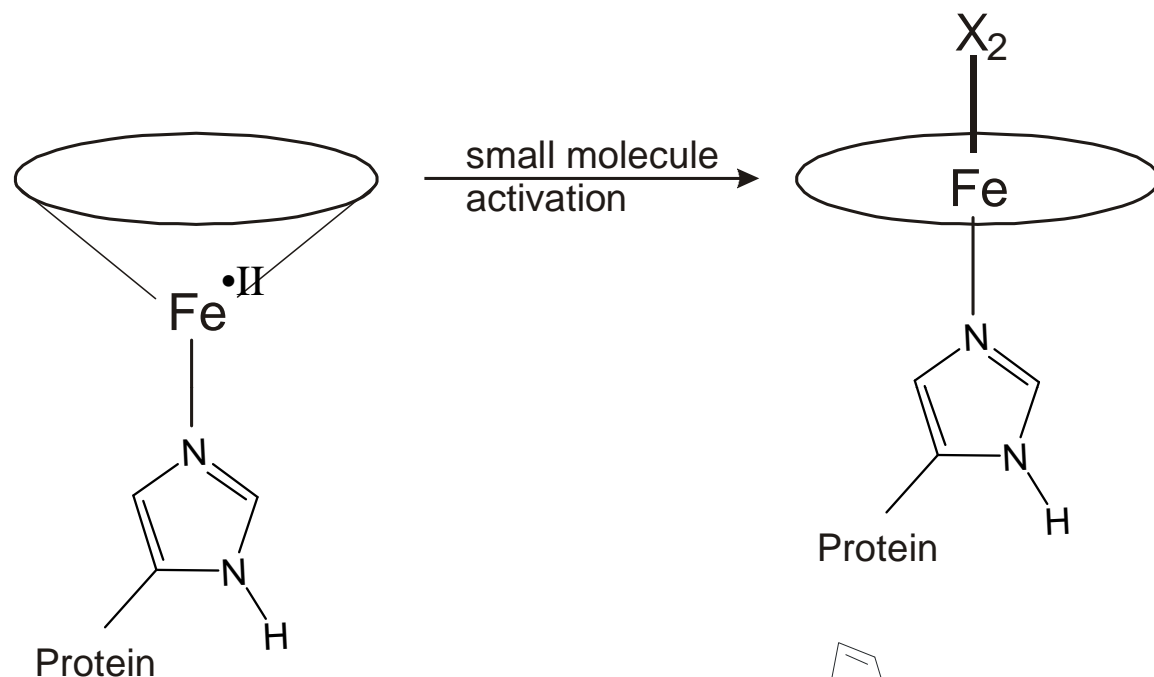
- strong CI leads to large splitting:
➔ Soret and Q band
- Q_v : results from **vibronic coupling** between Soret and Q excited states

Absorption Spectra of Metalloporphyrins

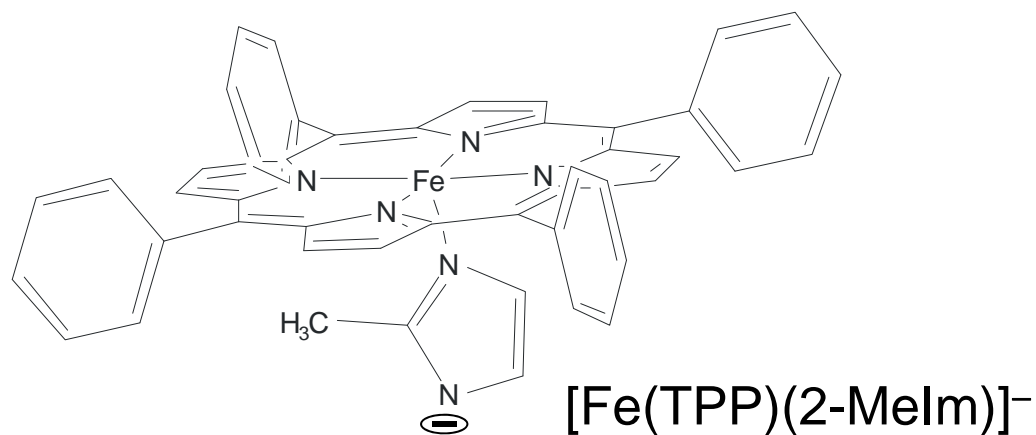
[Co(TPP)(Cl)]



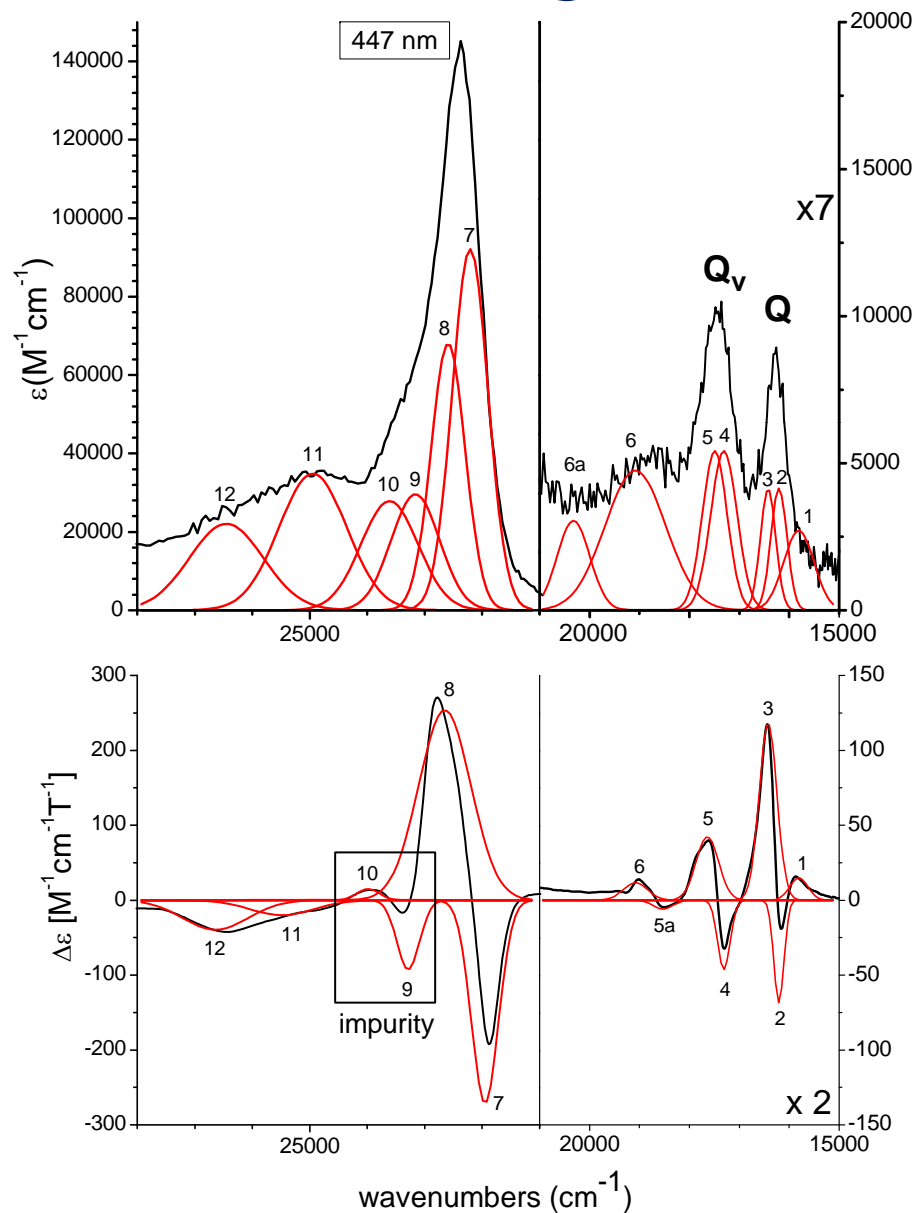
MCD Spectra of Metalloporphyrins



High-spin
ferrous heme
($S = 2$)

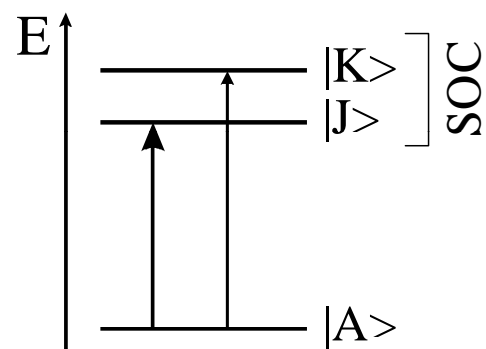


MCD of High-Spin Ferrous Hemes



The Soret, Q, and Q_V states give rise to a “pseudo **A** term” signal in low temperature MCD!

Due to Mechanism 1

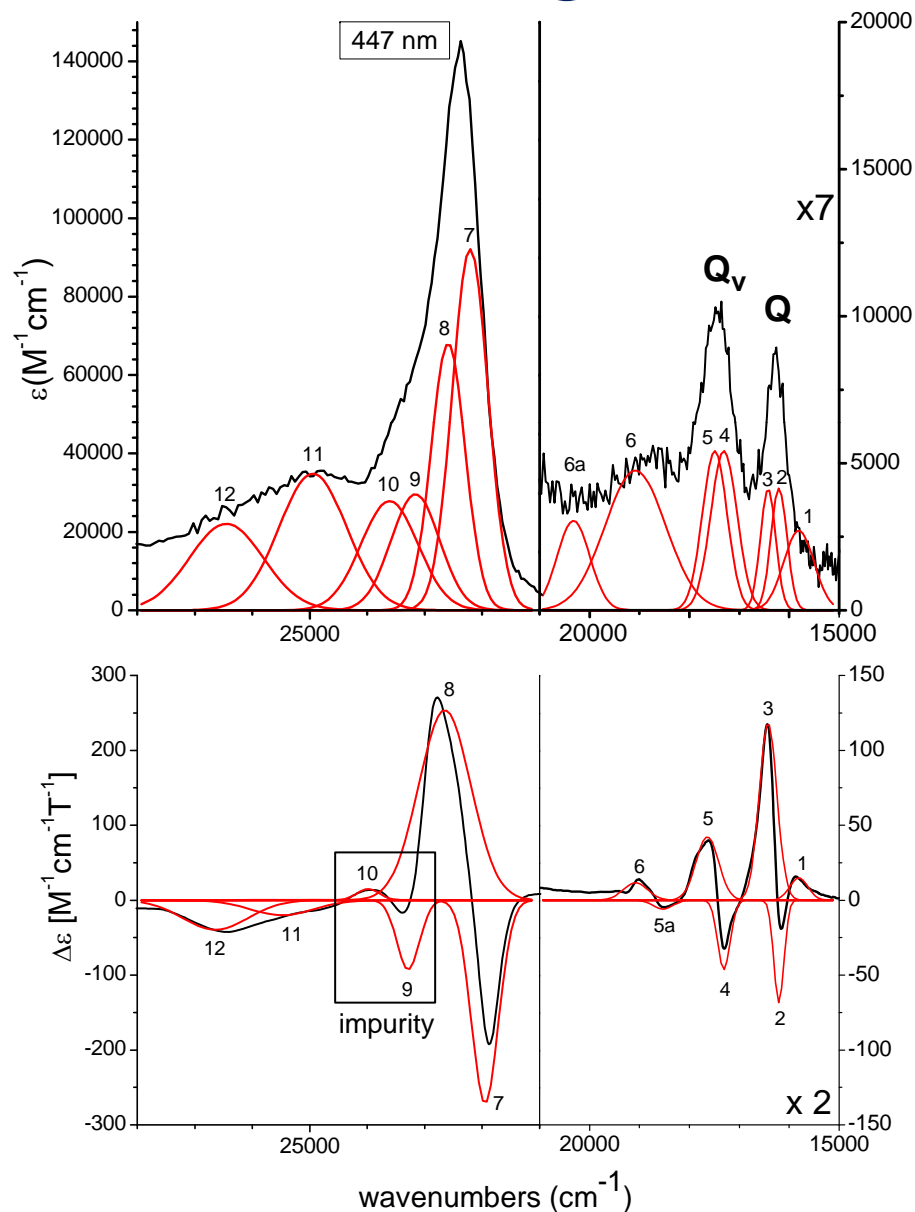


$$I^{MCD} \sim \Delta_{KJ}^{-1} \cdot \left(\vec{M}_u^{AJ} \times \vec{M}_v^{AK} \right) \cdot \vec{L}_w^{-KJ}$$

Here, $|J\rangle$ and $|K\rangle$ are the two components of the Soret, Q, and Q_V states (E_u in D_{4h} symmetry)

[N. Lehnert, in *The Smallest Biomolecules: Diatomics and their Interactions with Heme Proteins* (Ed.: A. Ghosh), Elsevier, Amsterdam, 2008, pp. 147-171]

MCD of High-Spin Ferrous Hemes

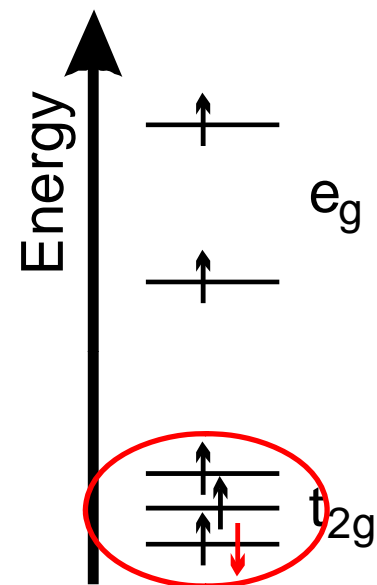


- 12 visible MCD bands
- MCD absolute intensity of the Soret band: $\sim 300 \text{ M}^{-1} \text{cm}^{-1} \text{T}^{-1}$
- All components of the Soret, Q, and Q_v bands are observed
- Shows a slight impurity leading to the bands 9, 10
 - The impurity is believed to be a ferric impurity
- [Fe(TPP)(MeHIm)] and [Fe(TPP)(Cl)]⁻: MCD spectra are overall similar in shape

MCD of High-Spin Ferrous Hemes

- MCD intensities:

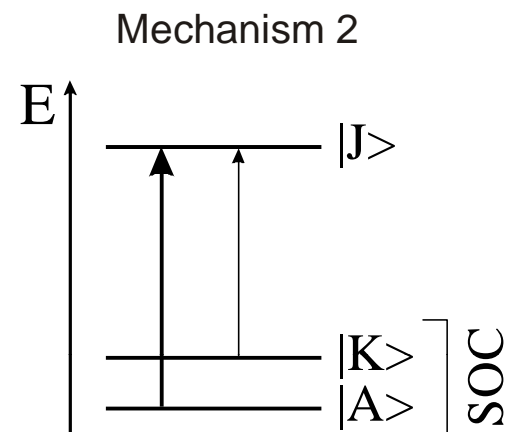
	Intensity [M ⁻¹ cm ⁻¹ T ⁻¹]
[Fe(TPP)(2-MeHIm)]	5000
[Fe(TPP)(2-MeIm)] ⁻	300
[Fe(TPP)(Cl)] ⁻	800



MCD of High-Spin Ferrous Hemes

- MCD intensities:

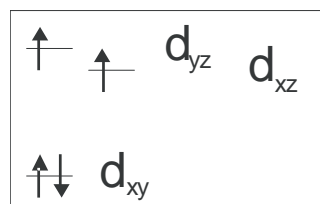
	Intensity [M ⁻¹ cm ⁻¹ T ⁻¹]
[Fe(TPP)(2-MeHIm)]	5000
[Fe(TPP)(2-MeIm)] ⁻	300
[Fe(TPP)(Cl)] ⁻	800



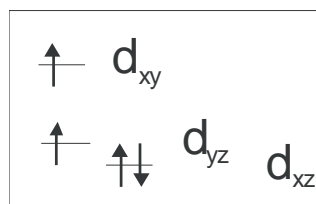
$$I^{MCD} \sim \Delta_{KA}^{-1} \cdot \left(\vec{M}_u^{KJ} \times \vec{M}_v^{AJ} \right) \cdot \vec{L}_w^{KA}$$

- Mechanism 2 results in two possible cases:

Case 1

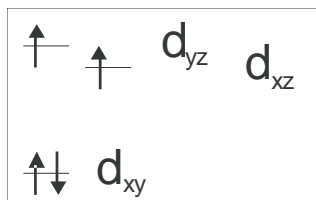


Case 2

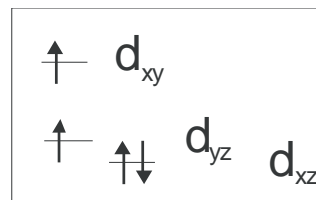


Origin of Intensity Difference?

Case 1



Case 2



■ Case 1

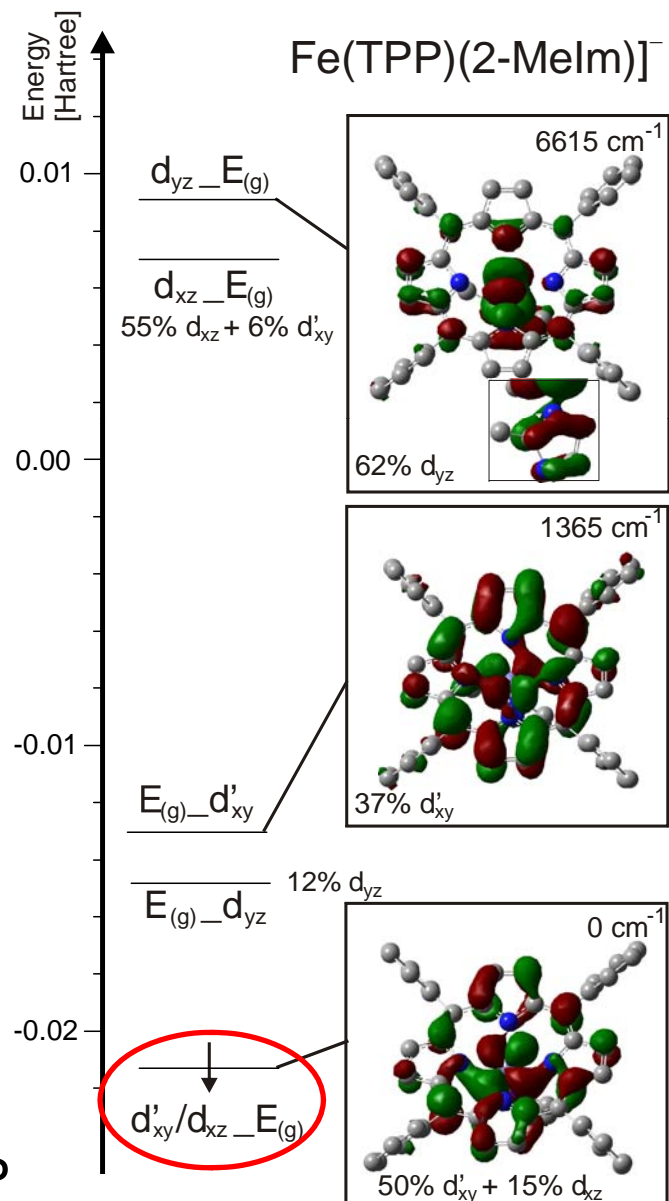
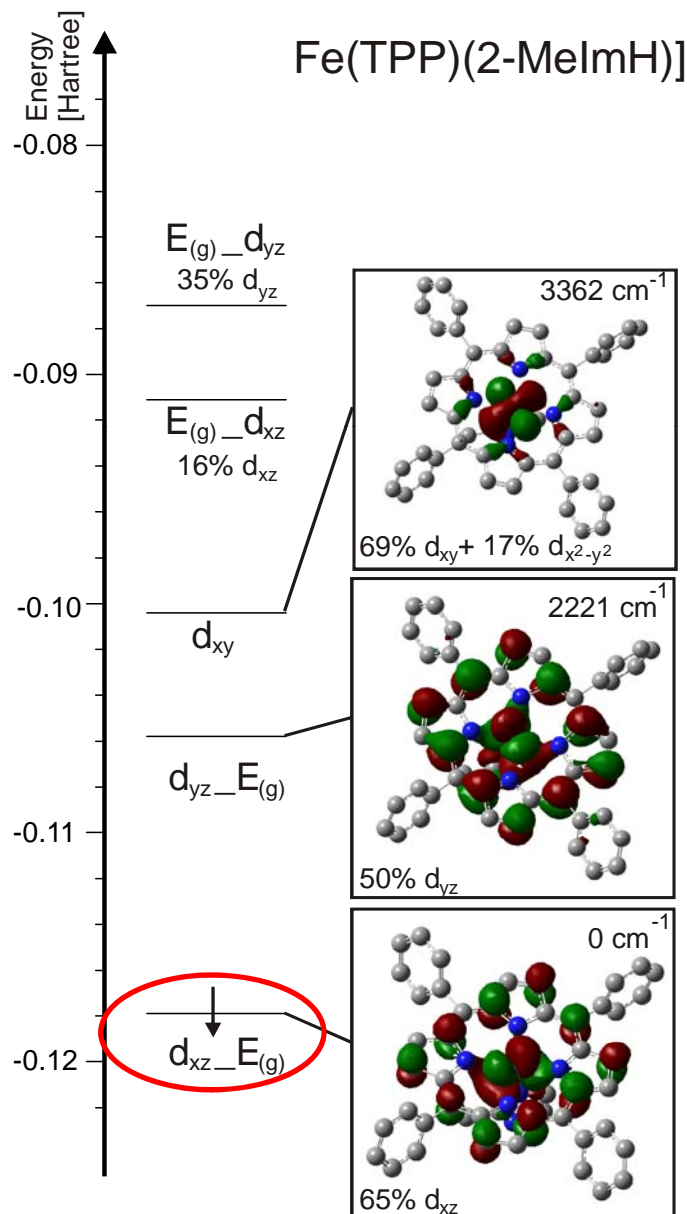
- The ground state is d_{xy} in character, when SOC is applied $\langle d_{xy} | l_z | d_{xz} \rangle$ and $\langle d_{xy} | l_z | d_{yz} \rangle$ are zero resulting in no additional **C**-term intensity

■ Case 2

- The ground state is d_{xz} in character, resulting in a nonzero SOC term $\langle d_{xz} | l_z | d_{yz} \rangle$ and an increase of the **C**-term intensity

 Difference in ground state!

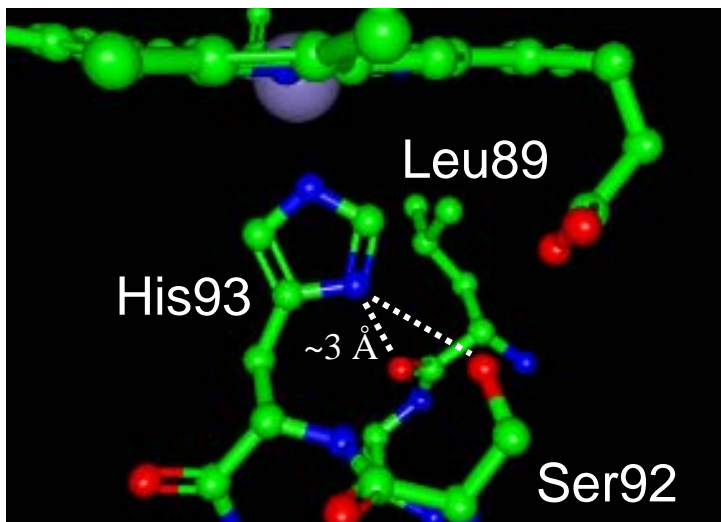
Electronic Structure



BP86/TZVP

Biological Relevance

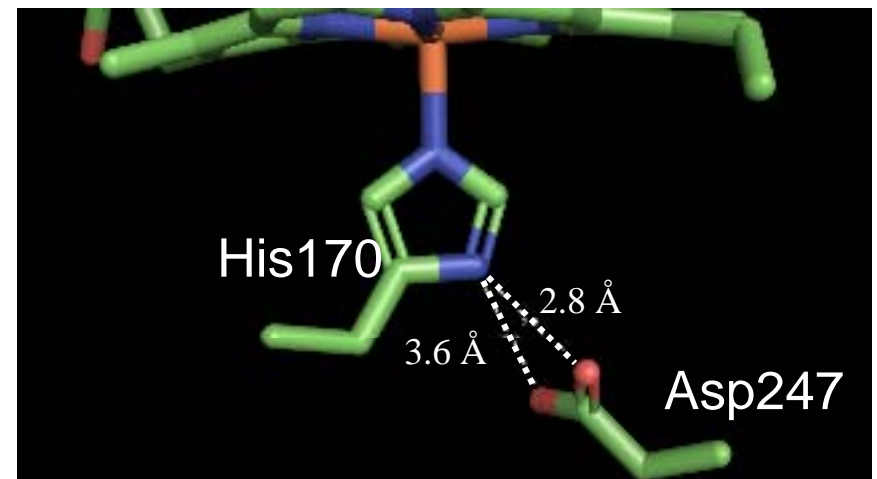
Case 2:
Globins: weak H-bond



Myoglobin. PDB: 2BLI

Nienhaus, Ostermann, Nienhaus, Parak,
Schmidt, *Biochemistry* **2005**, 44, 5095

Case 1:
Peroxidases: strong H-bond



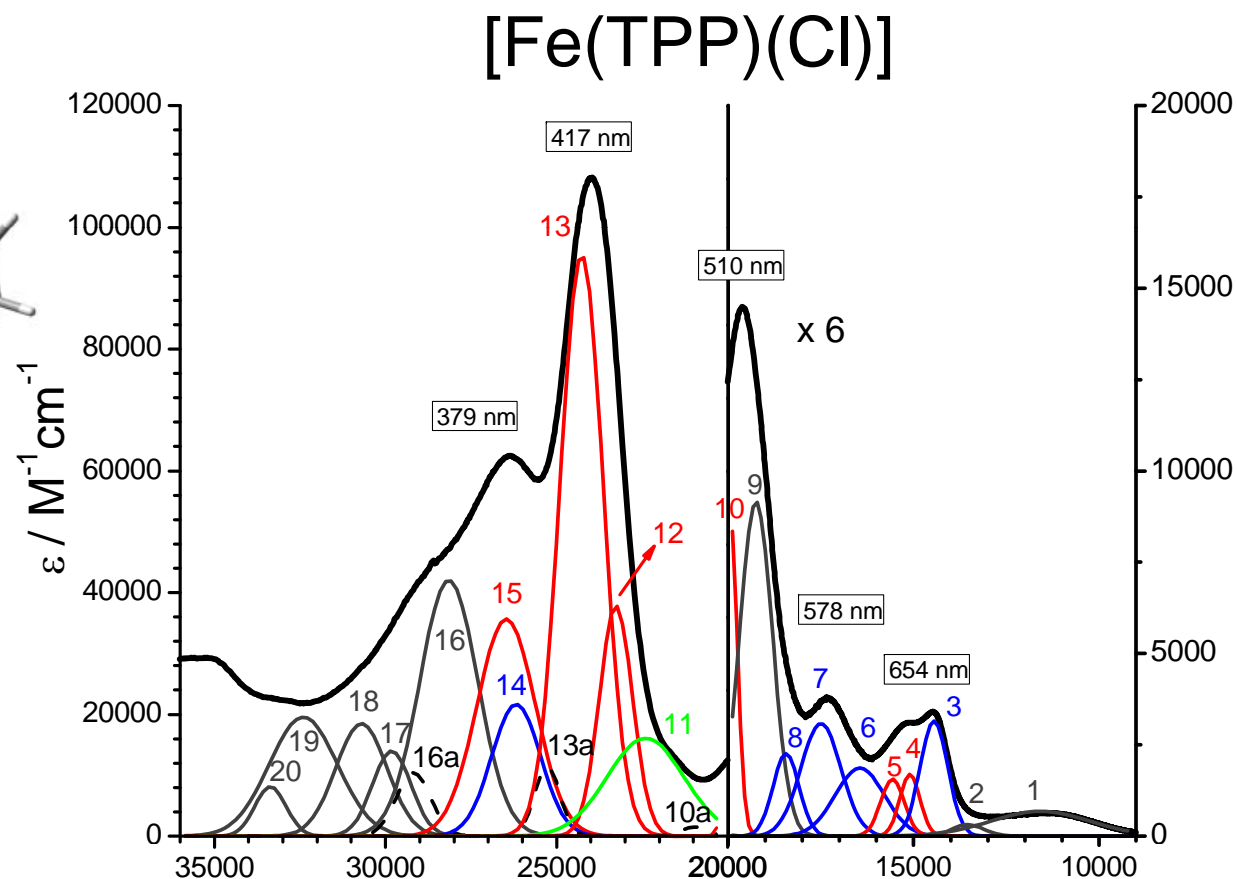
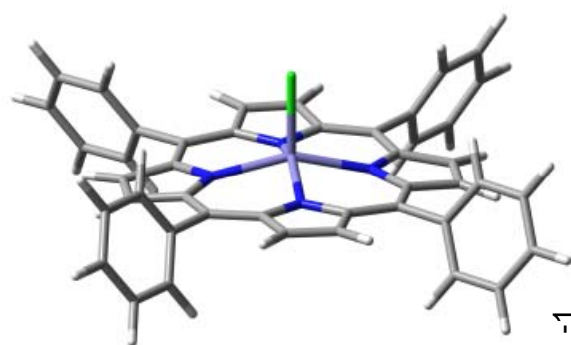
Horseradish Peroxidase. PDB: 1H58

Berglund, Carlsson, Smith, Szoke, Henriksen,
Hajdu, *Nature* **2002**, 417, 463

➡ The Strength of the H-bond determines the ground state!

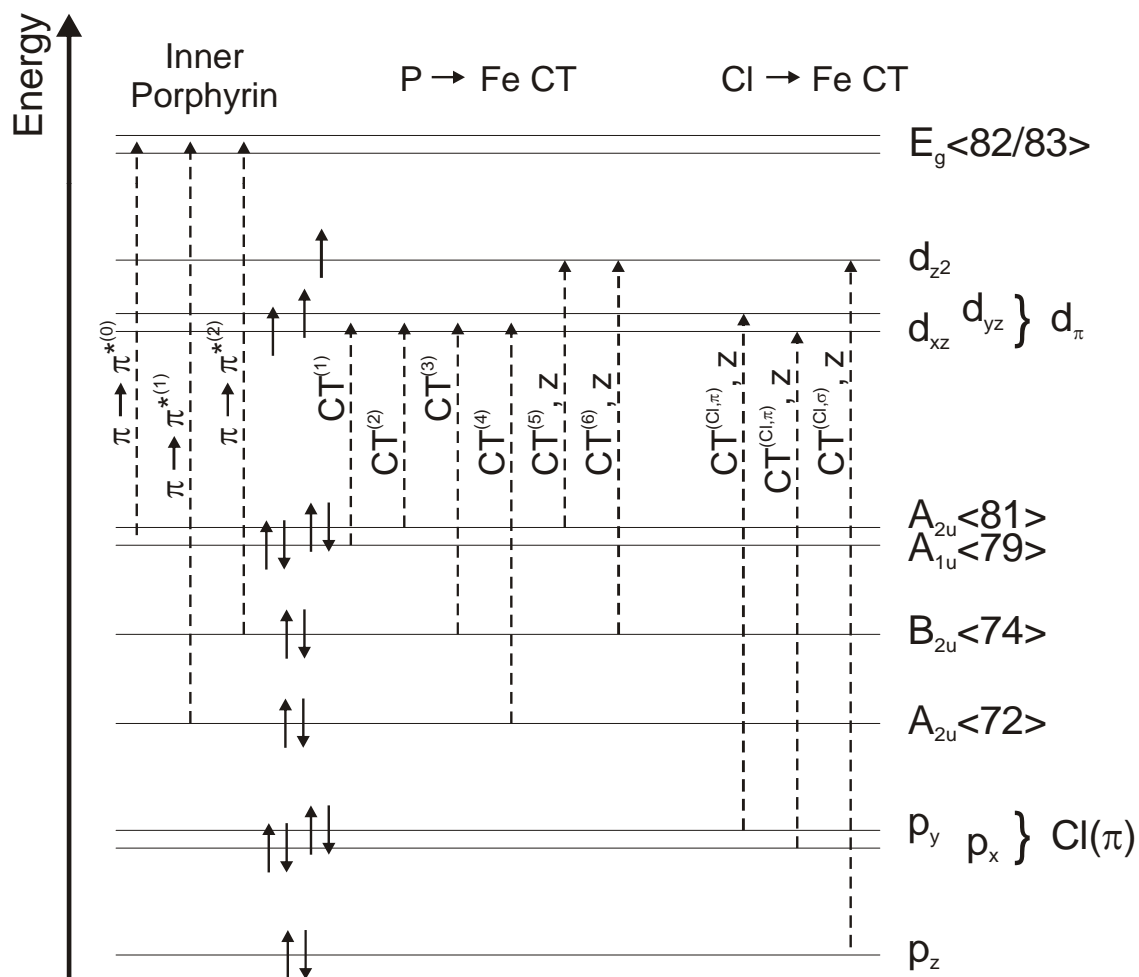
High-Spin Ferric Hemes ($S = 5/2$)

- Very rich electronic spectra! → Assignment?



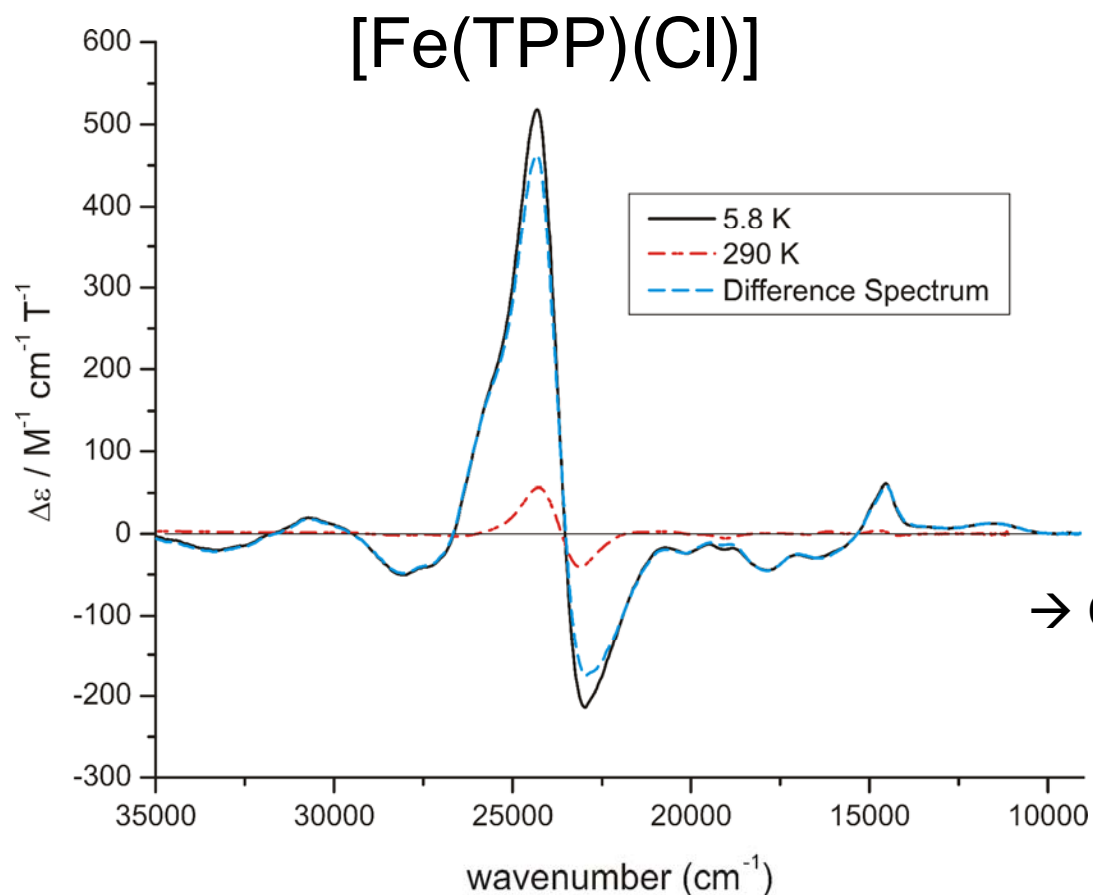
High-Spin Ferric Hemes ($S = 5/2$)

- Due to the half-filled d^5 configuration that allows for a multitude of CT transitions \rightarrow use MCD!



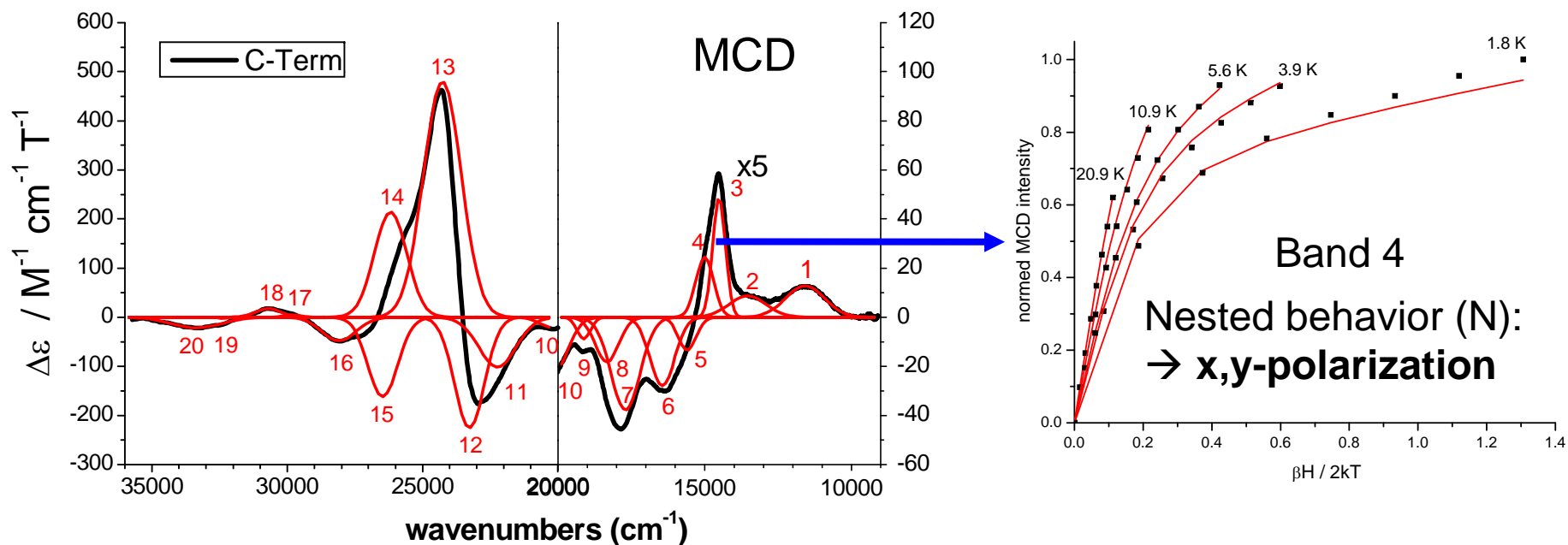
The MCD C Term Spectrum

- Calculate from low- and high-temperature data



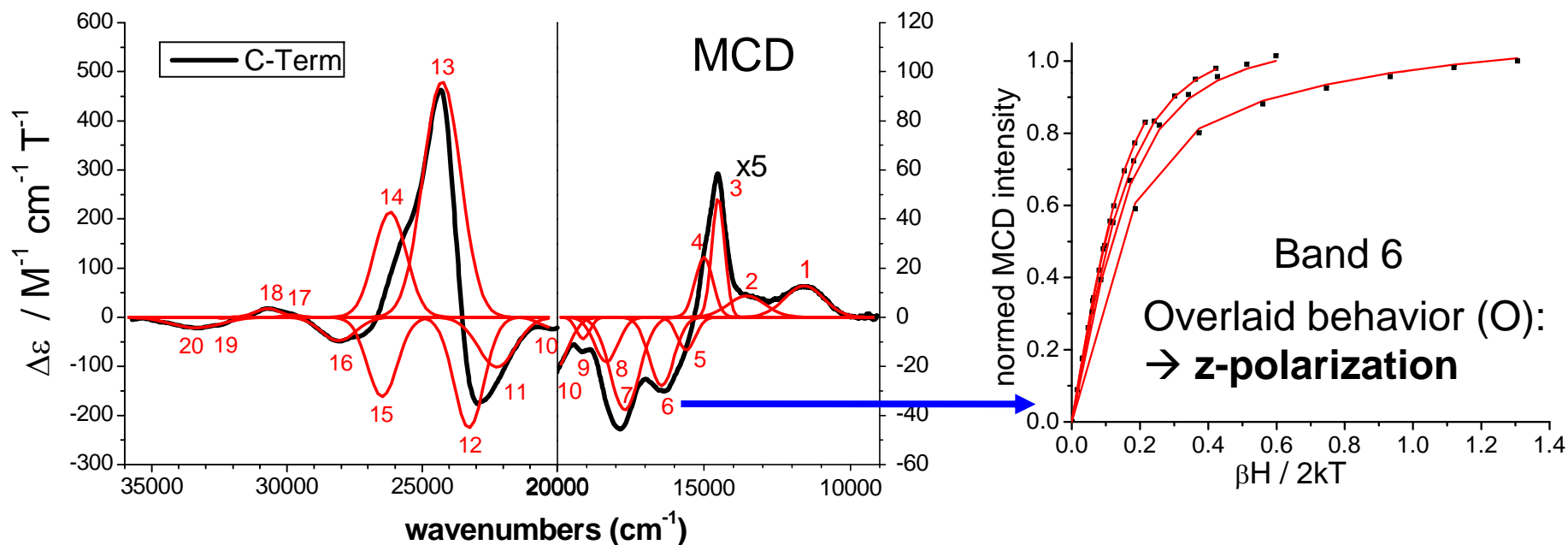
MCD of [Fe(TPP)(Cl)]

- Use VTVH saturation measurements to identify axial (Cl → Fe) CT transitions!



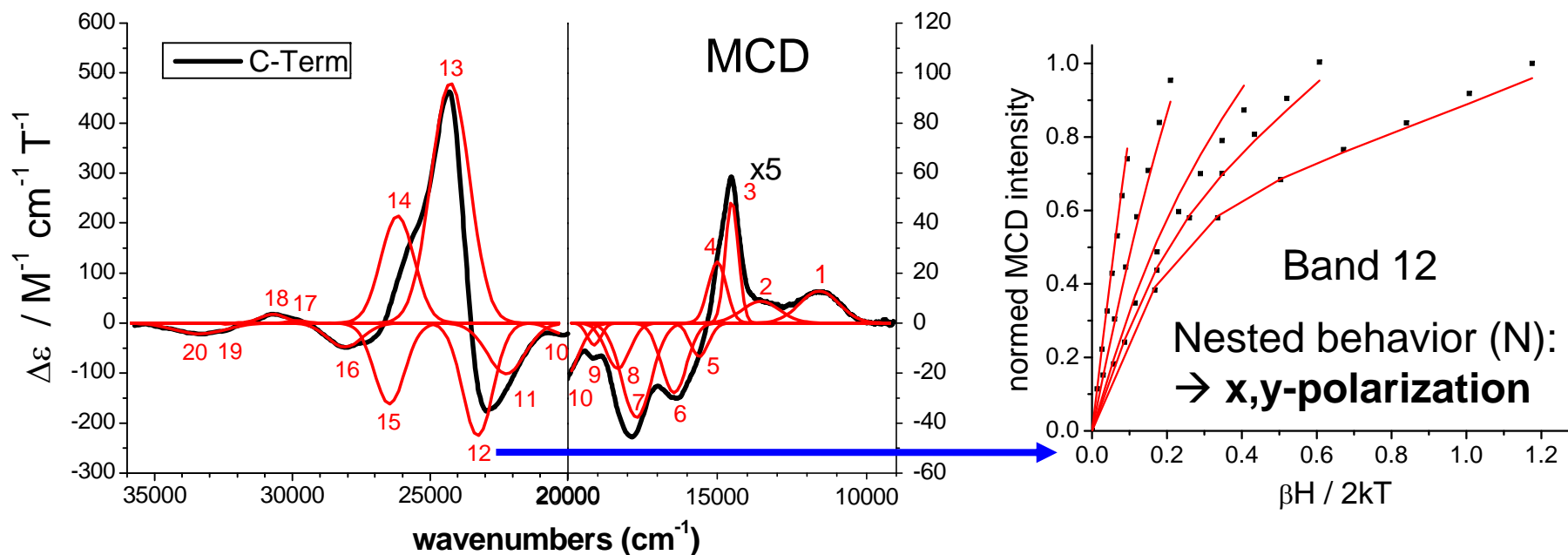
MCD of [Fe(TPP)(Cl)]

- Use VTVH saturation measurements to identify axial (Cl → Fe) CT transitions!

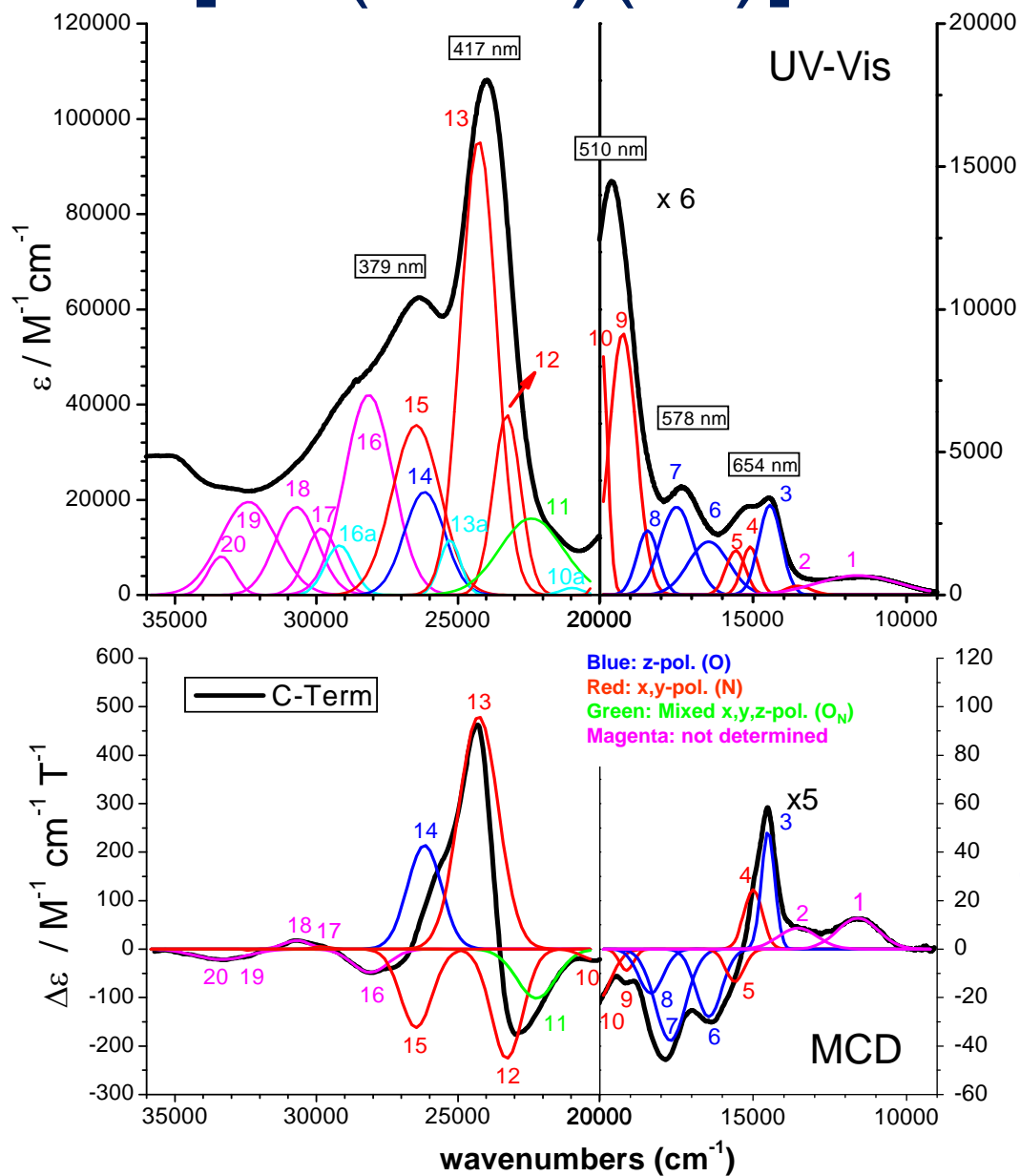


MCD of [Fe(TPP)(Cl)]

- Use VTVH saturation measurements to identify axial (Cl → Fe) CT transitions!

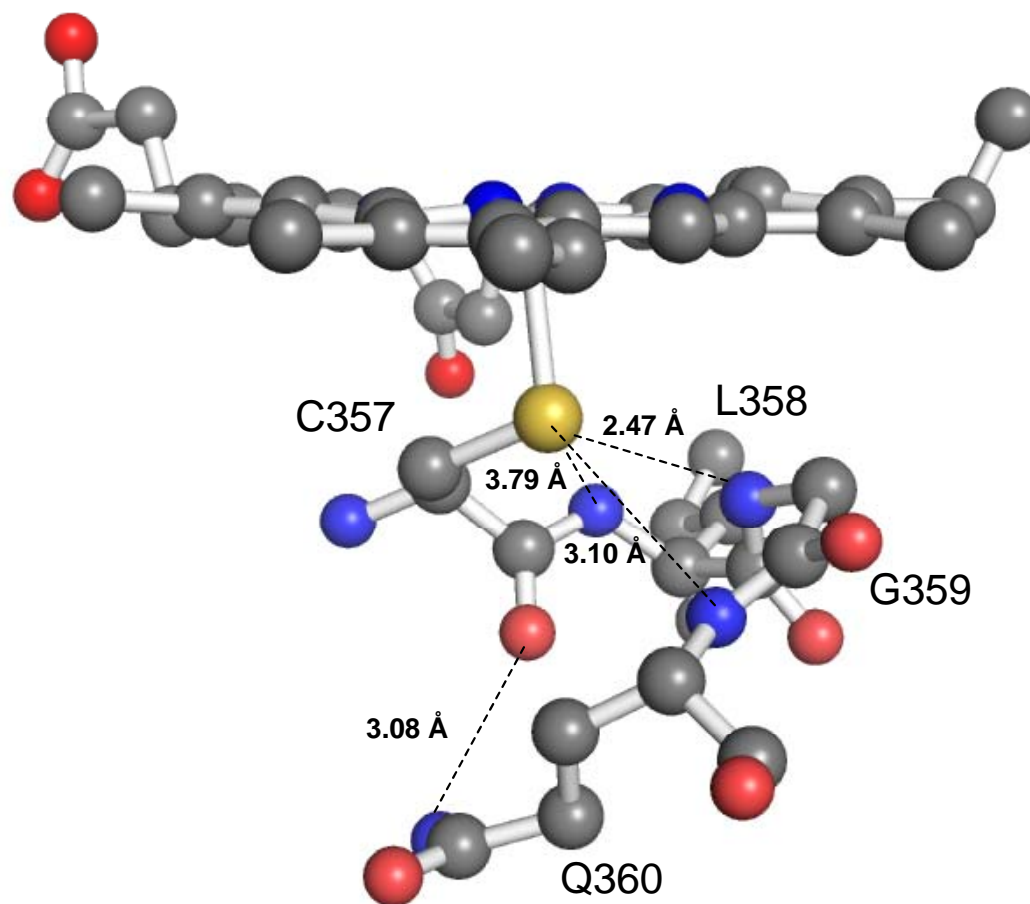


MCD of [Fe(TPP)(Cl)]



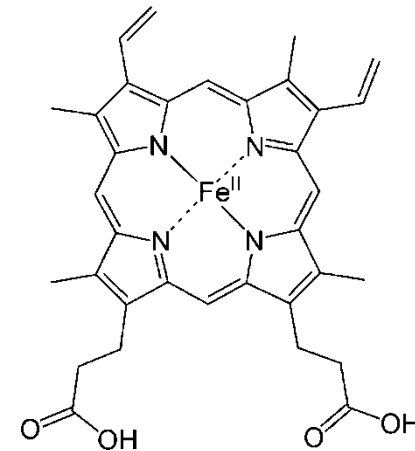
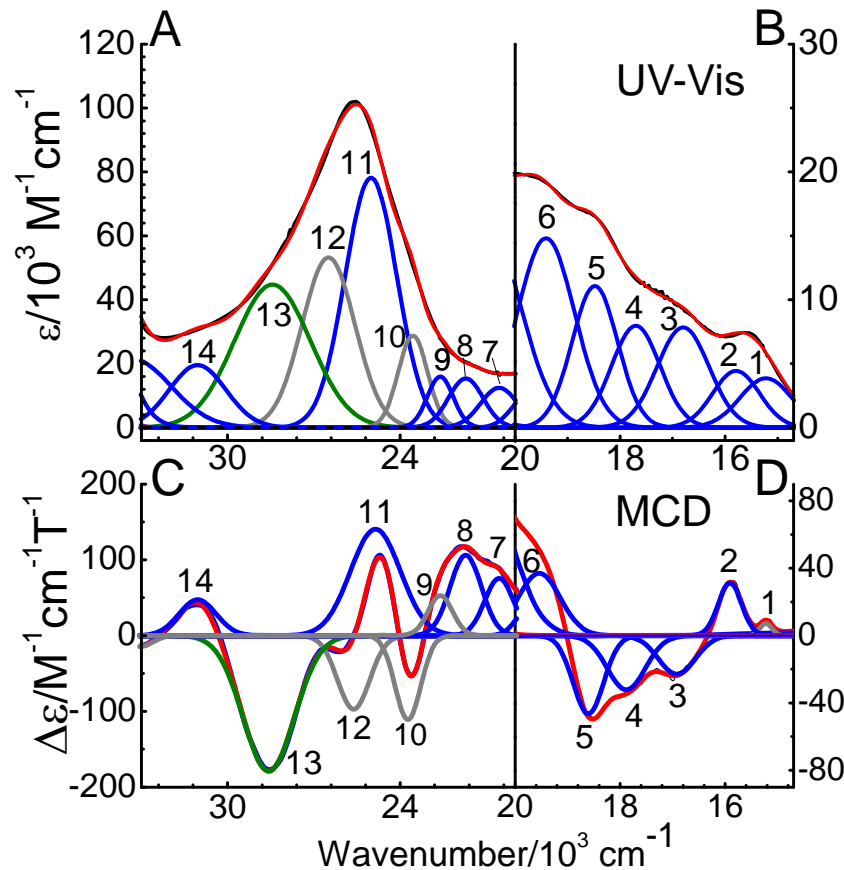
Transitions with significant Cl \rightarrow Fe CT character

The Cys Pocket and Mutants



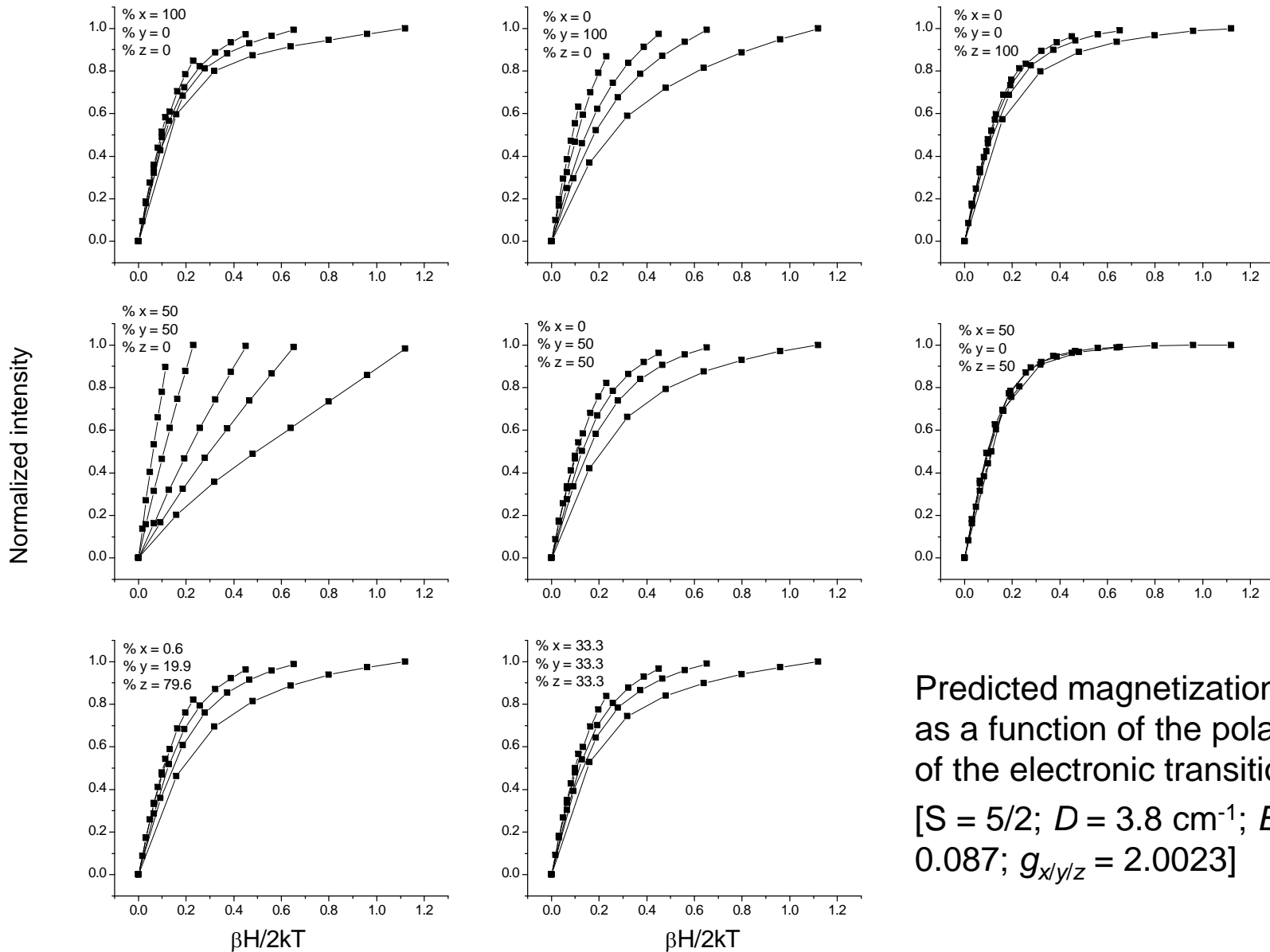
The Q360P Mutant

- Remains high-spin at lq. helium temperature (wt and most mutants form high/spin/low-spin mixtures)!



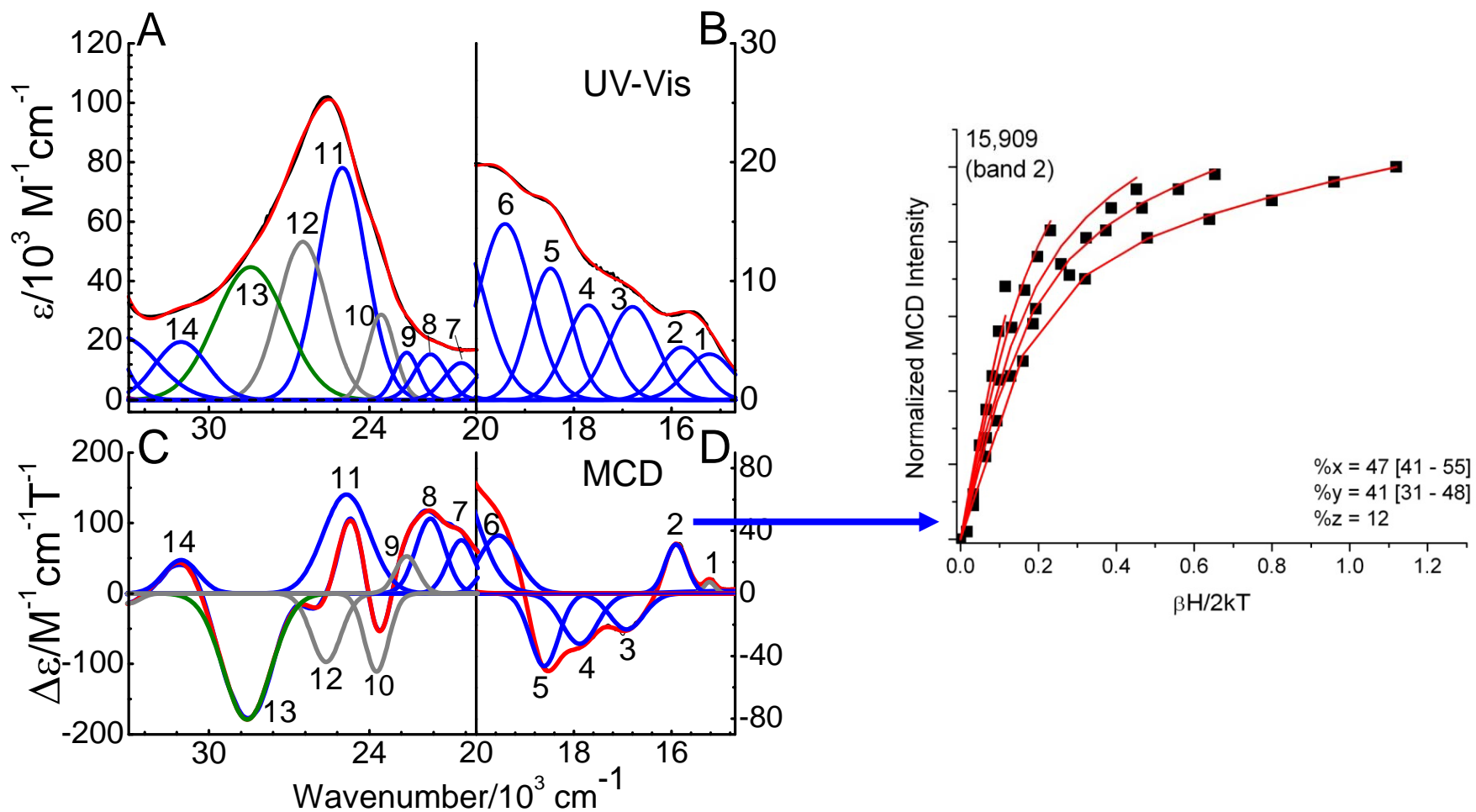
Low-symmetry heme
(heme *b*)
 → EPR: $E/D = 0.087$
 → Is the VTVH
 methodology going to
 work?

Magnetic Saturation Curves

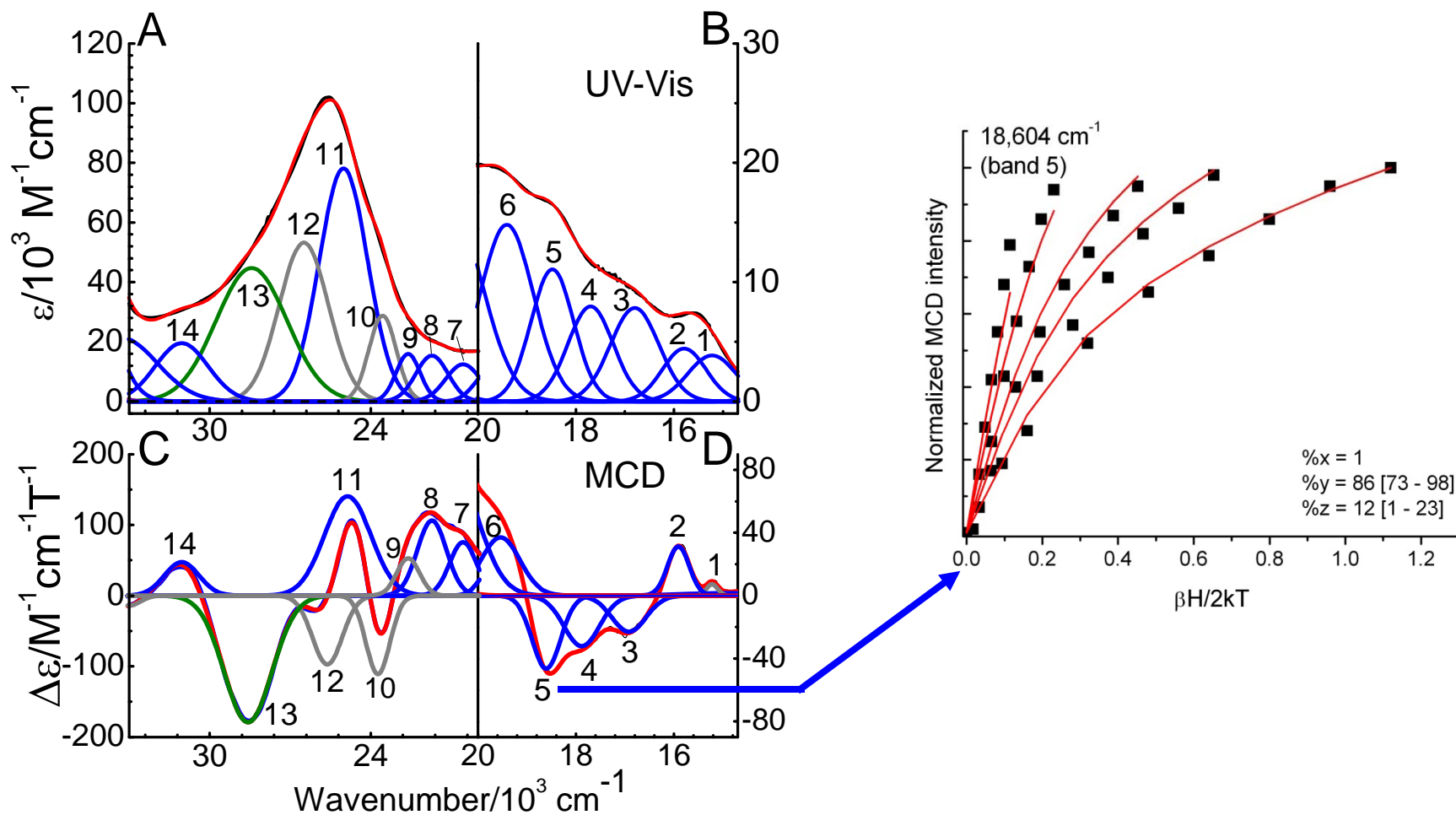


Predicted magnetization curves
as a function of the polarization
of the electronic transitions
[$S = 5/2$; $D = 3.8 \text{ cm}^{-1}$; $E/D = 0.087$; $g_{x/y/z} = 2.0023$]

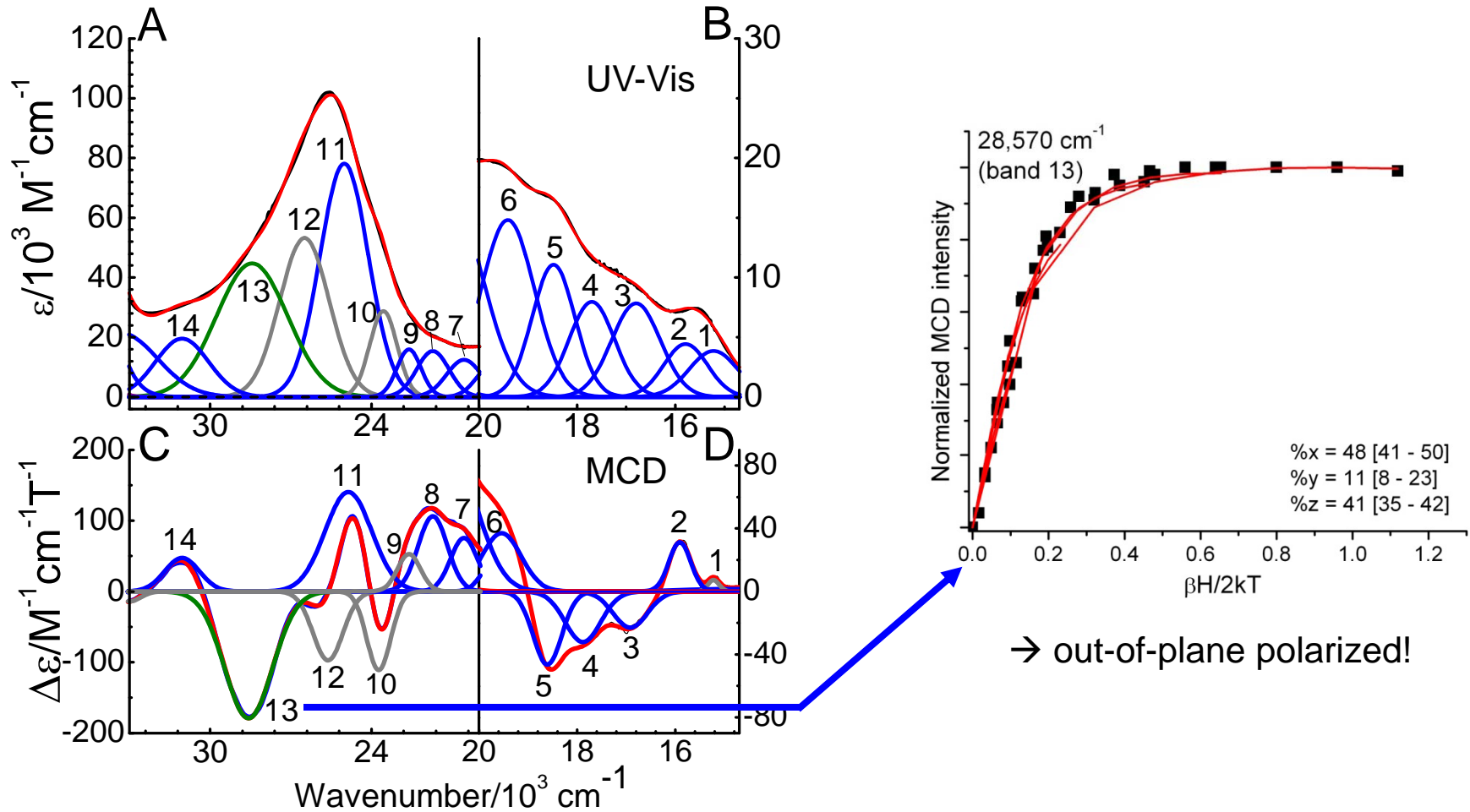
The Q360P Mutant



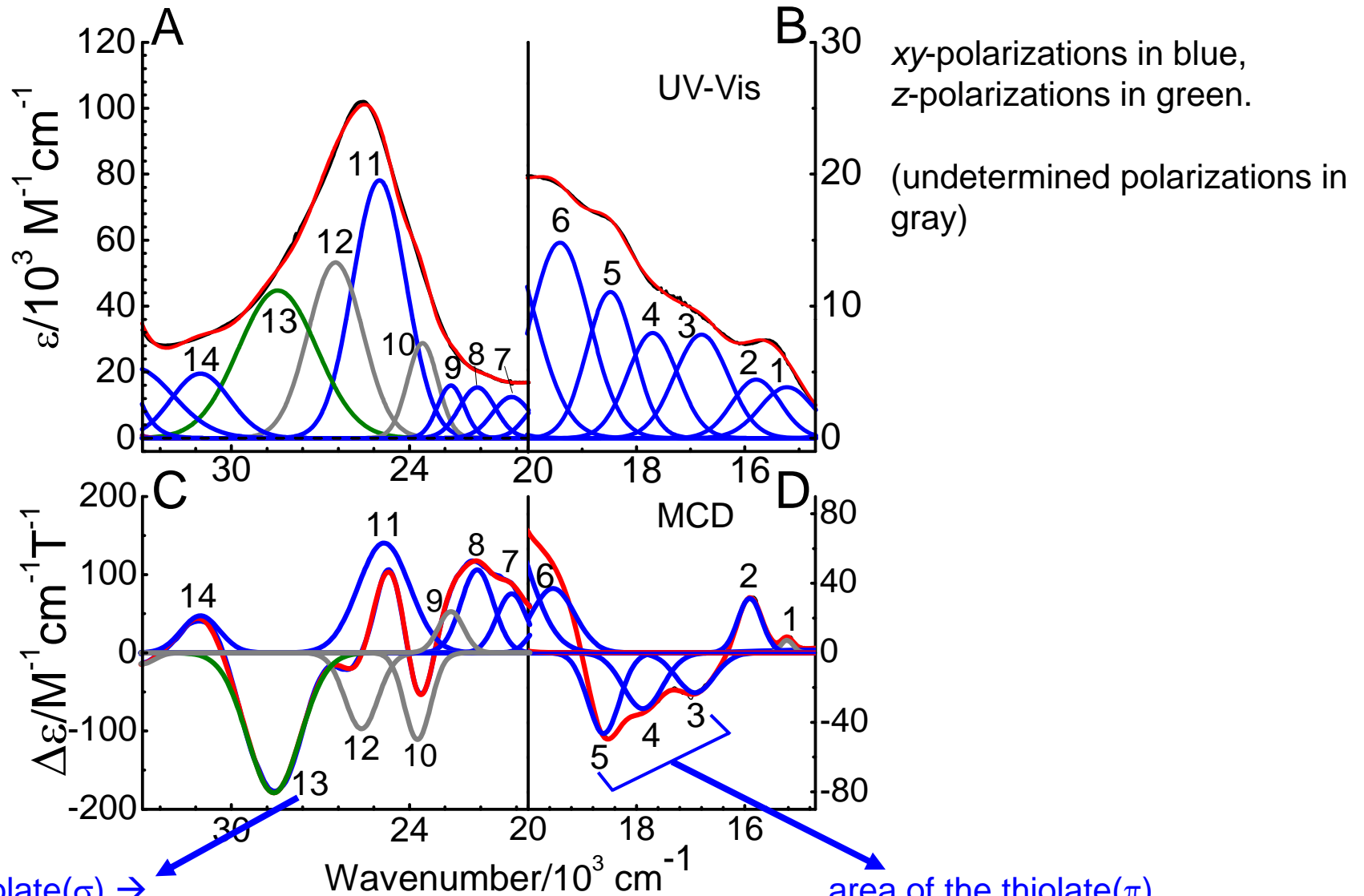
The Q360P Mutant



The Q360P Mutant



The Q360P Mutant

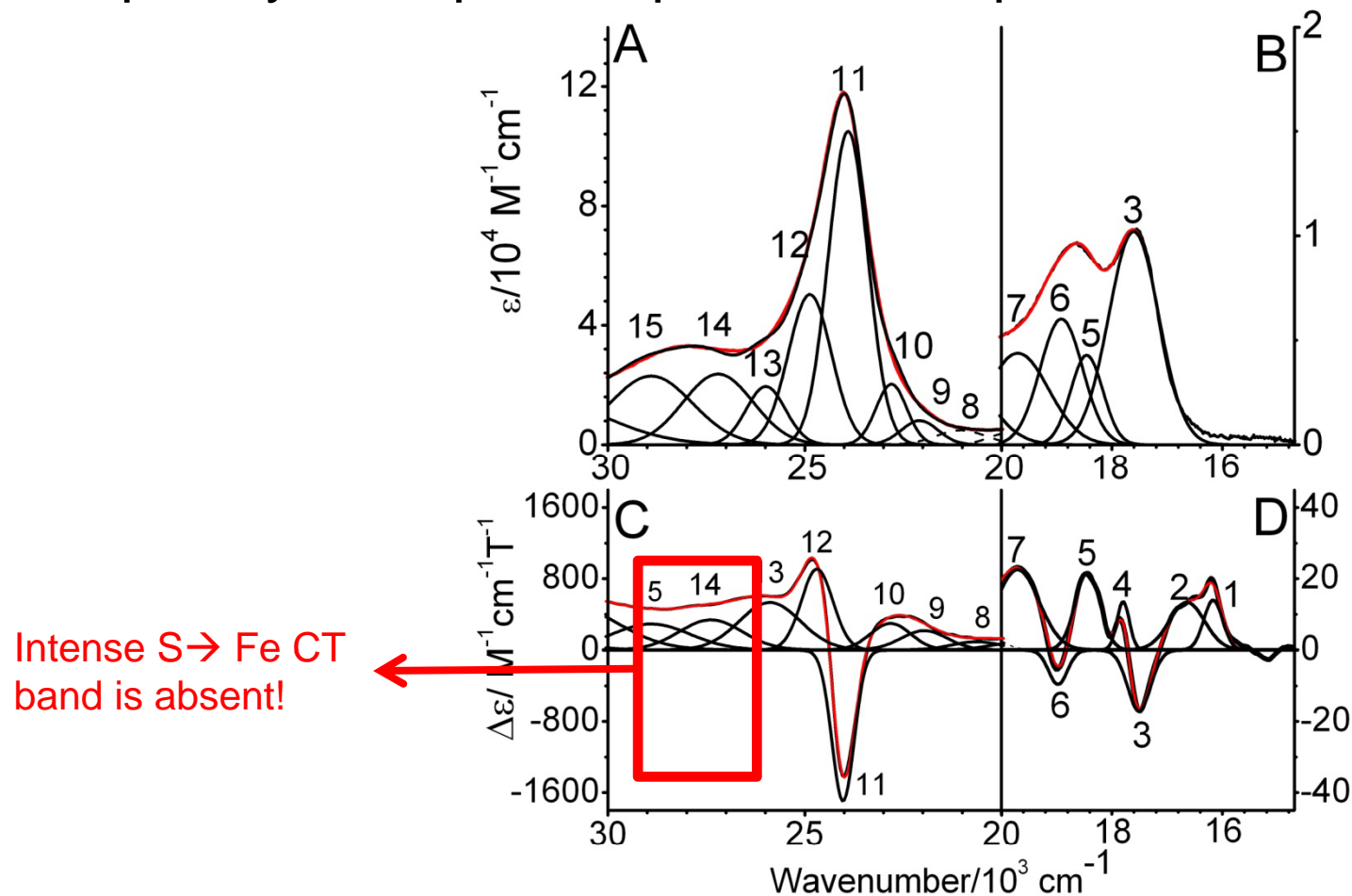


thiolate(σ) \rightarrow
Fe(III) CT

area of the thiolate(π)
 \rightarrow Fe(III) CT

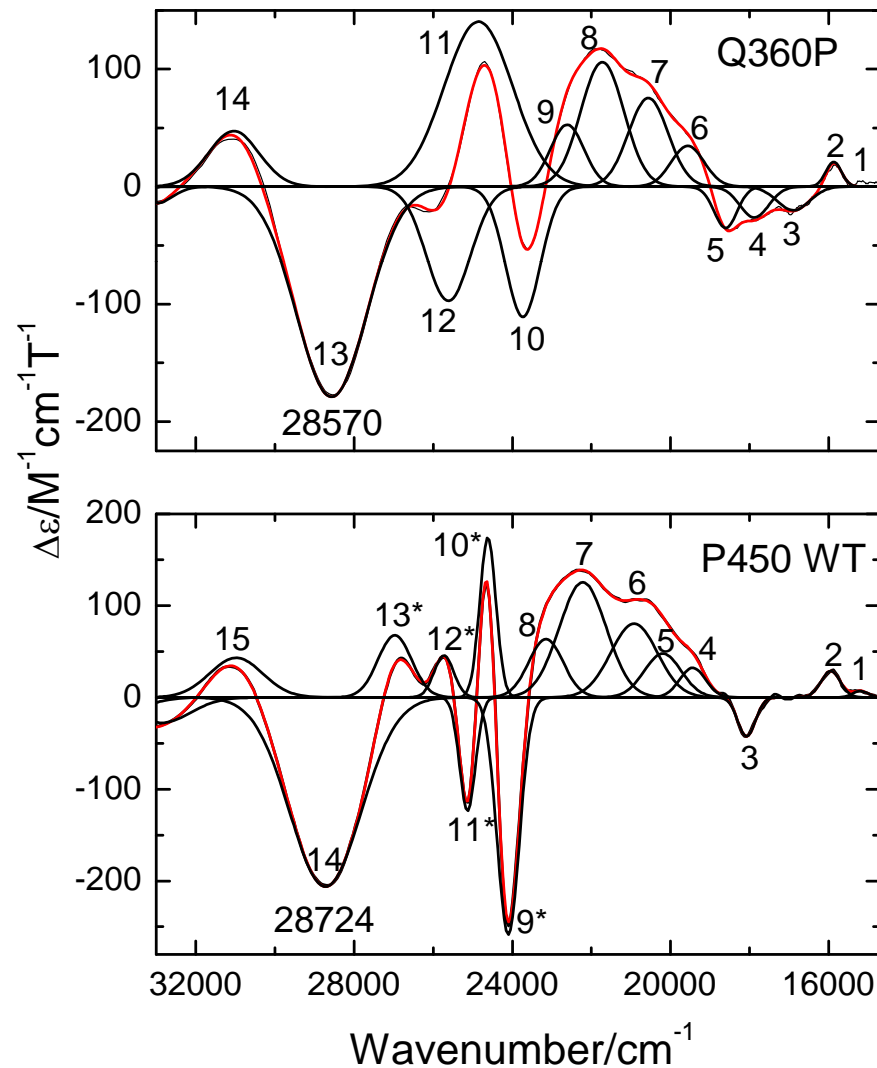
The Y96W Mutant

- Completely low-spin at lq. helium temperature!



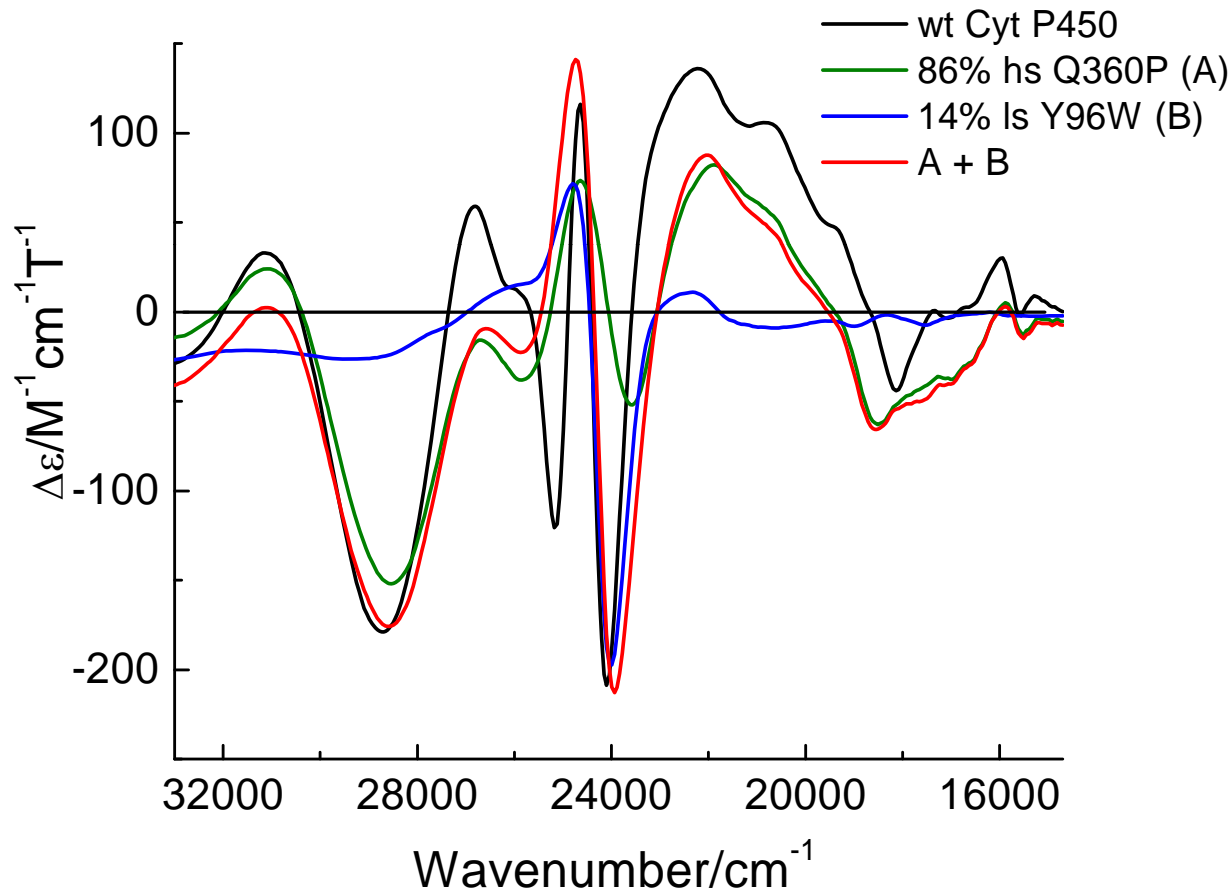
The MCD Spectrum of wt P450_{cam}

- High- and low-spin mixture at lq. helium temperature!



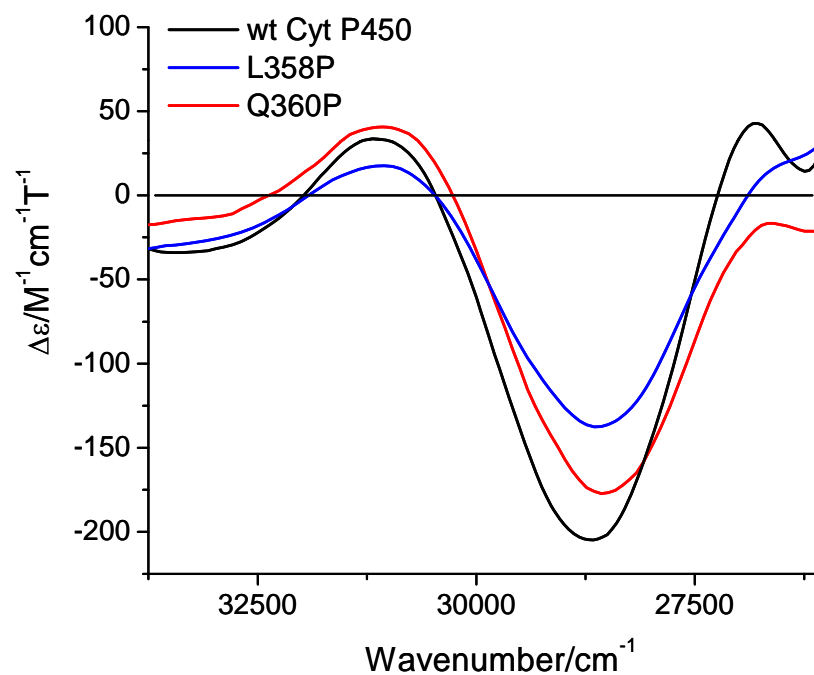
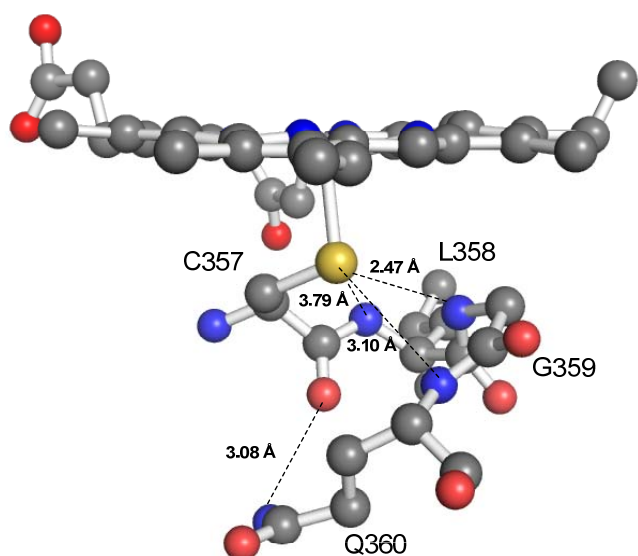
The MCD Spectrum of wt P450_{cam}

- High- and low-spin mixture at lq. helium temperature!



The Role of the Cys Pocket

- Mutation of the Cys pocket: Effect on S \rightarrow Fe(III) CT ?

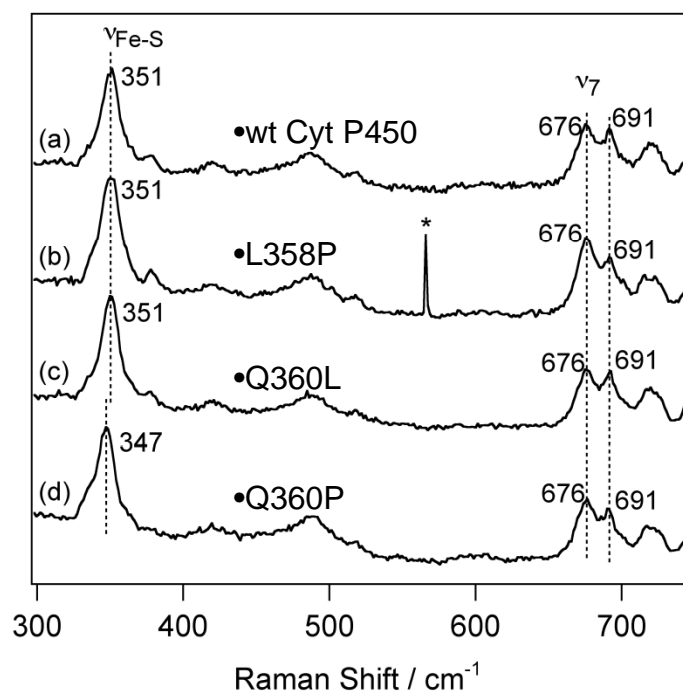


The Role of the Cys Pocket

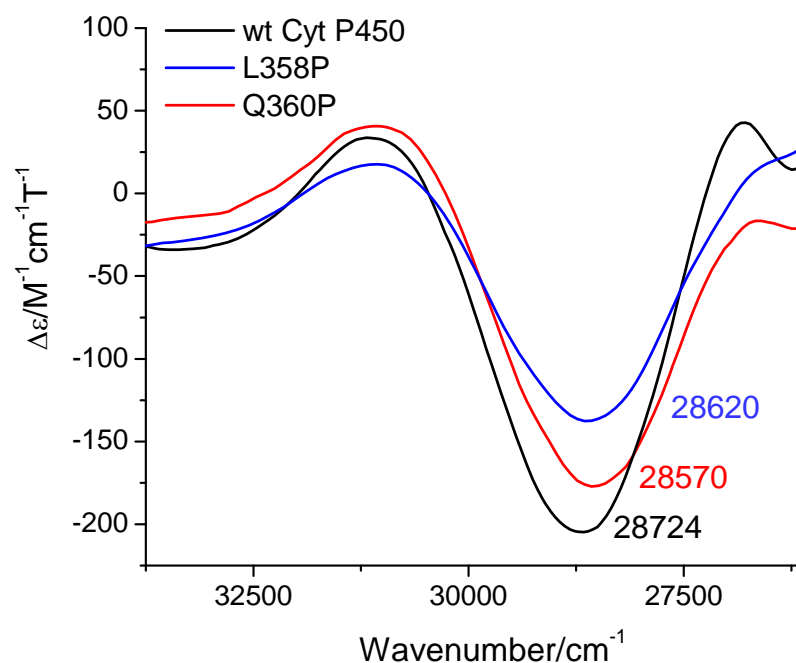
■ Comparison to resonance Raman Spectroscopy

(Yoshioka, Tosha, Takahashi, Ishimori, Hori & Morishima, *J. Am. Chem. Soc.* **2002**, 124, 14571-14579)

Resonance Raman



Magnetic Circular Dichroism (MCD)



Implications for Cyt. P450 Catalysis

- The hydrogen bonds from L358 and Q360 are weak and only have a minor effect on the properties of the Fe-S bond
- The hydrogen bonds are therefore important for a **stabilization** of the thiolate against protonation or reaction with diatomics compared to a fine-tuning of the Fe-S bond
- Weak H-bonds are the best compromise between stabilization of the thiolate, and strong S → Fe(III) donation, advantageous for:
 - Cleavage of the O-O bond (the “Push Effect”, John Dawson)
[Dawson, Holm, Trudell, Barth, Linder, Bunnenberg, Djerassi & Tang, *J. Am. Chem. Soc.* **1976**, 98, 3707-3709]
 - Basicity of the oxyl ion of the Fe=O unit in Compound I (Mike Green)
[Green, *Curr. Opin. Chem. Biol.*, **2009**, 13, 84-88]
- Future work: investigate G359 mutant!

Acknowledgement

Current Coworkers

Tim Berto

Katie CRAIGO

Shawn Eady

Deidra Gerlach

Lauren Goodrich

Ashley McQuarters

Amy Speelman

Matt Forster

Rohan Modak

Sheng Zheng



The MCD Team



Tim Berto



Grace Galinato



Florian Paulat



Amy Speelman

Recent advances in bioinorganic spectroscopy

Nicolai Lehnert, Serena DeBeer George and Edward I Solomon*

Spectroscopic methods covering many energy regions together provide complementary insight into metalloenzyme active sites. These methods probe geometric and electronic structure and define these contributions to reactivity. Two recent advances – determination of the polarizations of electronic transitions in solution using magnetic circular dichroism, electron paramagnetic resonance and quantum chemistry, and experimental estimation of covalency using metal L-edges and ligand K-edges – are particularly important.

Addresses

Department of Chemistry, Stanford University, Stanford, CA 94305, USA
*e-mail: edward.solomon@stanford.edu

Current Opinion in Chemical Biology 2001, 5:176–187

1367-5931/01/\$ – see front matter
© 2001 Elsevier Science Ltd. All rights reserved.

Abbreviations

ABLM	activated bleomycin
ABS	electronic absorption spectroscopy
BLM	bleomycin
CD	circular dichroism
CT	charge-transfer
ENDOR	electron nuclear double-resonance
EPR	electron paramagnetic resonance
ESEEM	electron spin-echo envelope modulation
HOMO	highest-occupied molecular orbital
LT MCD	low-temperature MCD
LUMO	lowest unoccupied molecular orbital
MCD	magnetic CD
MOT	molecular orbital theory
VTVH	variable-temperature variable-field
XAS	X-ray absorption spectroscopic
ZFS	zero field splitting

Introduction

Figure 1 gives the complete energy level diagram of a transition metal site (using $D_{4h}^- [CuCl_4]^{2-}$ as an example) [1]. Spectroscopic methods that probe different energy regions in this diagram cover over 10 orders of magnitude in photon energy [2]. The theme of this *Current Opinion* review is that different methods give different types of information and the appropriate combination of methods provides maximum insight into the geometric and the electronic structure of an active site and defines these contributions to reactivity.

At lowest energy is the ground state. The ligand field environment of the metal site splits its d orbitals in energy. The highest energy orbitals are partially occupied and these contribute to the magnetic properties of the active site. Covalency further extends these magnetic orbitals onto the ligands involved in specific bonding interactions with the metal ion. To probe the ground state, complexes with unpaired electrons are placed in an external magnetic field and studied at low resolution by magnetic susceptibility and at high resolution by magnetic Mössbauer (for iron) and electron paramagnetic resonance (EPR)-based methods. The dominant information

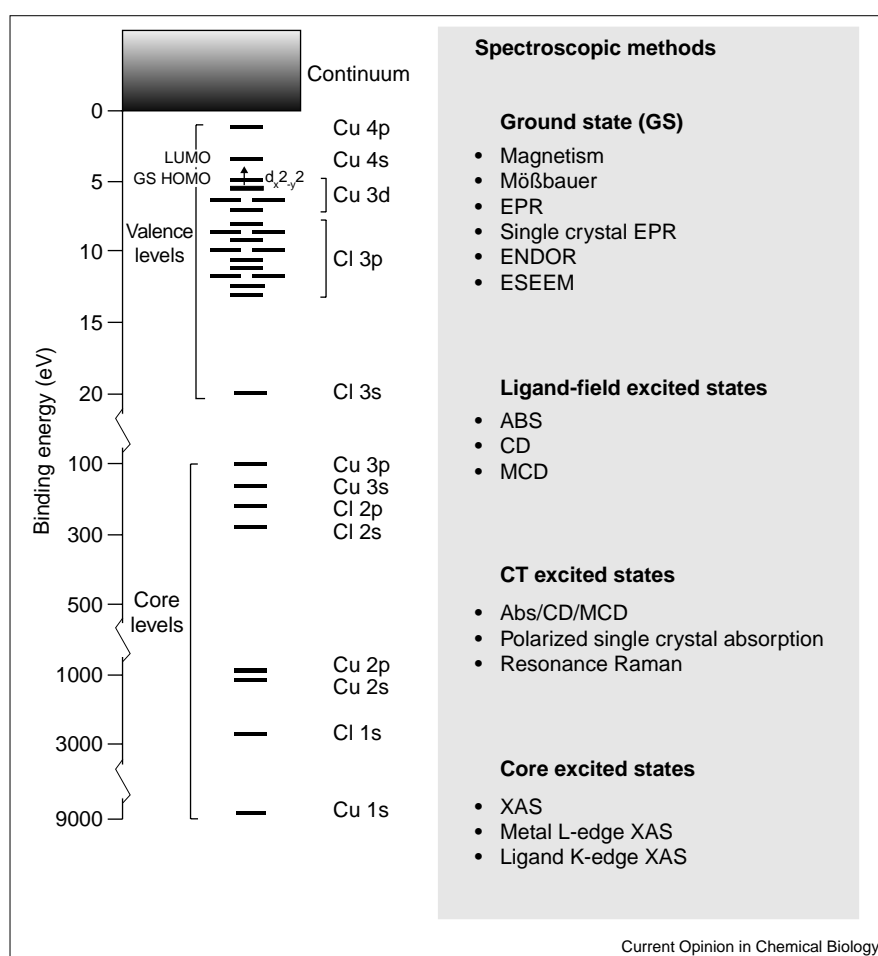
available from these methods is the anisotropy of the **g** tensor (formally a matrix), which is governed by the nature of d orbitals containing the unpaired electrons. From a single-crystal study, the orientation dependence of the **g** matrix defines the orientation of the half-occupied orbitals of the metal site. Magnetic Mössbauer and EPR also exhibit hyperfine couplings of the unpaired electrons to the nuclear spins on the metal and the ligands (the latter called superhyperfine coupling). These provide direct probes of the covalency (i.e. the metal and ligand contributions to the valence orbitals). The superhyperfine coupling is a very direct probe of the ligand character in a metal d-derived molecular orbital; however, this coupling is often too small to resolve in a continuous wave single-resonance EPR study. Superhyperfine coupling can alternatively be measured using double resonance (i.e. in electron nuclear double-resonance [ENDOR]) and pulsed (i.e. electron spin-echo envelope modulation [ESEEM]) methods. For ground states with $S > 1/2$, the spin degeneracy can be split even in the absence of a magnetic field. This is known as zero field splitting (ZFS) and is described below.

To higher photon energy (i.e. the near infra red and visible spectral regions), the electrons are excited from the filled d to the half-occupied or unoccupied metal valence orbitals. These are called ligand field or d–d transitions. The energy splitting of the metal-based d orbitals is accurately given by ligand-field theory as long as the site is not overly covalent. These transitions provide a very sensitive probe of the geometric and electronic structure of an active site. The ligand-field transitions are studied in small molecule inorganic complexes with electronic absorption spectroscopy (ABS). These transitions are Laporté forbidden and often cannot be observed in the absorption spectrum of metalloproteins. However, different spectroscopic methods are governed by different selection rules. Absorption intensity is governed by the square of the electric dipole transition moment. Alternatively, circular dichroism (CD) is dependent on the product of the electric and magnetic dipole transition moments. Because ligand-field transitions are often magnetic dipole allowed, these can be intense in the CD spectrum relative to the absorption spectrum. Magnetic circular dichroism (MCD) requires contributions from two perpendicular electric dipole transition moments. In low-symmetry sites, electronic transitions can only be unidirectional. Therefore, paramagnetic active sites derive low-temperature MCD (LT MCD; called **C** term) intensity by spin-orbit coupling between excited states. (A second mechanism for MCD intensity involves spin-orbit coupling between the ground state and an excited state.) Because the metal has a much larger spin-orbit coupling constant than the ligand, metal-centered d–d transitions will generally also be more intense in the LT MCD relative to the absorption spectrum.

Overlapping the ligand field transitions in the visible/UV spectral regions are the charge-transfer (CT) transitions,

Figure 1

Complete molecular orbital diagram of $[\text{CuCl}_4]^{2-}$ with an overview of different spectroscopic methods to probe the ground state and various excited states.



which involve excitation of electrons from filled valence orbitals on the ligand to the half occupied or unoccupied valence orbitals on the metal center. Because the intensity of a CT transition reflects the overlap of the donor and acceptor orbitals involved, these are very sensitive probes of specific ligand–metal bonding interactions. From the above discussion, CT transitions can be distinguished from the ligand-field transitions by the different selection rules involved in ABS/CD/MCD spectroscopies. CT transitions are generally intense in absorption (because they are electric-dipole allowed) and weak in the CD and LT MCD spectra. The specific assignment of these transitions requires additional spectral insight. In single crystals, the polarizations of the electronic transitions allow their assignments to specific ligand–metal bonds. This, however, is a very difficult experiment and new methodologies have been developed that allow these polarizations to be obtained for metalloproteins in solution (see below). A complementary probe is resonance Raman spectroscopy. The high intensity of the CT transitions ($\epsilon \geq 1000 \text{ M}^{-1}\text{cm}^{-1}$) allows resonance enhancement of Raman vibrations, and the vibrations that are resonance enhanced reflect the change in bonding that occurs in the electronic transition.

At still higher energy (X-ray region) are transitions from the filled core orbitals on the metal and ligand into the partially occupied or unoccupied valence orbitals on the metal ion and into the continuum. The most well known X-ray absorption spectroscopic (XAS) method is metal K-edge spectroscopy, in which the ionized metal 1s electron reflects off the ligand atoms leading to interference effects on the metal K-edge (i.e. extended X-ray absorption fine structure [EXAFS]). On the low-energy side of the metal K-edge are bound-state transitions of the metal 1s electrons into the metal 3d and 4p orbitals. These can provide insight into the oxidation state, spin state and coordination number of the metal center. Whereas the metal K-edge is a low-resolution probe of the active site (this is because of its high energy and the fact that the $1s \rightarrow 3d$ transition is not electric-dipole allowed), the metal L-edge and ligand K-edge can provide higher resolution probes of a metal center and, in particular, their intensities provide a very direct method to quantitate covalency of the metal d-based molecular orbitals. This is described in a later section.

While spectroscopy provides experimental probes of the energy level diagram in Figure 1, major advances have also

recently been made in calculating the electronic structures of metalloenzyme active sites. The traditional methods of ligand-field theory, and extended Hückel, semi-empirical and *ab initio* (with correlation) molecular orbital theories (MOTs) have been strongly complemented by density functional theory (DFT). These theoretical methods ($X\alpha$, local density approximation [LDA], generalized gradient approximation [GGA] and hybrid [for example, B3LYP]), for the first time, routinely allow high-level calculations on large transition metal systems, as is required for metalloprotein active sites. Here it should be emphasized that it is critically important to evaluate DFT methods with spectroscopic data. There is a tendency in DFT calculations, for at least some metal ions, to overemphasize the covalency (the amount of ligand character in a metal d orbital), which will strongly affect total energies. Methods that adjust these calculations on the basis of experimental data are now being developed. Calculations supported by data can be used to define new bonding interactions, and extend our understanding from known species (reactants, products and intermediates) to obtain total reaction energies and evaluate reaction coordinates and transition states in catalysis.

This brings us to the goals of spectroscopy in bioinorganic chemistry. Generally, these are to define active site geometric and electronic structure and to use these to develop structure/function correlations in biology. Combined with perturbations (i.e. substrate, co-factor and small-molecule binding, etc.), spectroscopy will provide insight into a reaction mechanism on a molecular level. Rapid freeze quench and related kinetic methods allow one to identify and trap the intermediates in a reaction, the nature of which can be determined through detailed spectroscopic study.

In a number of important areas of bioinorganic chemistry, new spectroscopic methods have been required to study metal centers. One example is the area of non-heme iron active sites, which are found in a wide range of mononuclear and binuclear enzymes. They do not exhibit the intense spectral features of heme sites. Many non-heme iron sites are catalytically active from their high-spin ferrous states, which do not exhibit the intense ligand-to-metal CT absorption bands associated with ferric sites and are integer spin non-Kramers systems, which generally do not exhibit an EPR signal. Variable-temperature variable-field (VTVH) MCD in the near IR spectral region has now been developed and provides detailed insight into these active sites. This methodology has recently been reviewed [3]. Finally, many metalloenzymes exhibit unique spectroscopic features as compared to small-molecule complexes of the same metal ion. As these unique features are becoming understood through a combination of different spectroscopic methods, they are found to reflect new geometric and electronic structures that activate the metal site for catalysis. The unique spectral features include intense absorption bands that are low-energy ligand-to-metal CT transitions. Because CT intensity derives from orbital

overlap, these transitions reflect highly covalent bonds. Definitive spectroscopic data are required to assign these transitions and, below, an MCD/EPR/MOT methodology is presented that allows their polarizations to be obtained in solution. Because covalency plays a key role in reactivity, a spectroscopic methodology combining metal L-edge and ligand K-edge XAS has been developed, and is presented in a later section, which allows covalency to be experimentally quantitated for metalloenzyme active sites. In both cases, the functional significance of the spectroscopic data is emphasized.

Recent advances

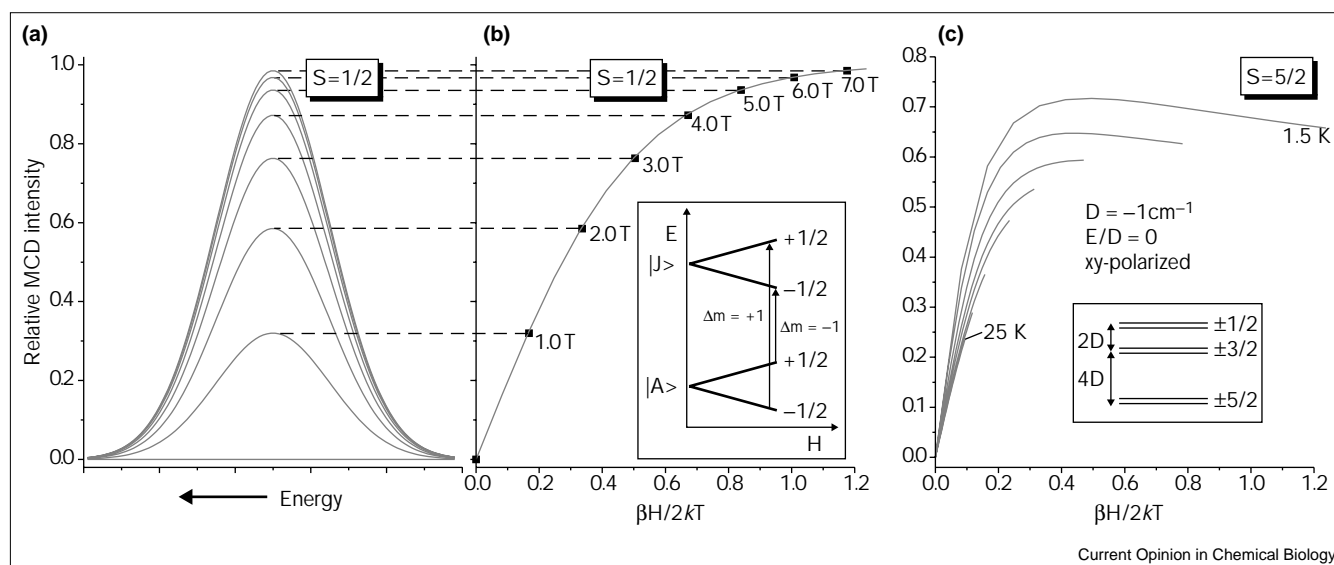
Polarizations of electronic transitions in solution (VTVH MCD/EPR/MOT)

Polarizations of absorption bands [4] and resonance Raman profiles [2] provide important spectroscopic insight into the assignment of electronic transitions. Rigorously assigned electronic absorption bands combined with vibrational force constants are experimental tests of the accuracy of quantum-chemical calculations. Determining the polarizations of electronic transitions requires polarized single-crystal absorption spectroscopy. In many cases, however, suitable single crystals are not experimentally accessible. In recent years, a methodology has been developed that allows the determination of absolute polarizations from samples of randomly oriented molecules in frozen solutions or powders. The polarizations gained from fitting MCD saturation curves ([5••–7••]; see below) are relative with respect to the \mathbf{g} matrix or \mathbf{D} tensor of the molecule. With the help of quantum-chemical calculations, their orientations in the molecular framework can be determined and this way the absolute orientation of the polarization tensor is obtained [8••]. In this section, we will introduce this methodology and apply it to activated bleomycin (ABLM) [3], the oxygen intermediate involved in the cleavage of DNA by this anticancer drug.

Magnetic circular dichroism spectroscopy

CD spectroscopy that is performed in a longitudinal magnetic field (relative to the light beam) is known as MCD spectroscopy. Both CD and MCD measure the difference in the extinction, $\Delta\epsilon$, between left and right circular polarized light; $\Delta\epsilon = \epsilon_l - \epsilon_r$. Three different types of transitions are observed in the MCD experiment, which are designated as **A**, **B** and **C** terms [9–13]. **C** terms are indicative of a paramagnetic ground state and their intensity is inversely proportional to temperature and, hence, they usually dominate the MCD spectra of paramagnetic species at low temperature. Below, we deal with the properties of **C** term signals. Figure 2a schematically shows the field dependence of an MCD **C** term band simulated for an $S = \frac{1}{2}$ system. At low fields, the intensity of the band is directly proportional to the applied field at a given temperature. At higher fields, the signal levels off and saturates. The dependence of the MCD intensity on temperature and field is explored by the VTVH experiment, in which the intensity at a given wavelength is

Figure 2



VTVH MCD data for $S = 1/2$ and $S = 5/2$ systems. (a) Simulated MCD spectra using Gaussian band shapes at $T = 2\text{K}$ with isotropic g values ($g = 2.00$) and polarizations ($M_{xy} = M_{xz} = M_{yz}$). (b) Resulting VTVH saturation curve. Note that for $S = 1/2$ all the VTVH isotherms overlay. The insert shows a schematic representation of the transitions for left ($\Delta m = +1$) and right ($\Delta m = -1$) circular polarized light from the

ground state ($|A\rangle$) to the excited state ($|J\rangle$) sublevels. In a magnetic field, the $m_s = \pm 1/2$ sublevels split by $g\beta H$ (cf. Equation 3), giving rise to a C term signal at low temperature. (c) Axial $S = 5/2$ system with negative ZFS (see insert). This leads to the nesting behaviour of the VTVH curves with the isotherms at lower temperature saturating at higher intensity.

plotted against $\beta H/2kT$ (β is the Bohr magneton and k the Boltzmann constant). Figure 2b shows the resulting VTVH curve for the MCD signal in Figure 2a (at 2K), illustrating the saturation of the signal at higher fields. The insert in Figure 2b shows the origin of this saturation behaviour. The $S = 1/2$ ground state, $|A\rangle$ (orbitally non-degenerate), is linearly split into its two components with $m_s = -1/2$ at lower energy than $m_s = +1/2$ in a magnetic field. In the case of a spin-allowed transition, a similar splitting occurs for the $S = 1/2$ excited state, $|J\rangle$. For left circular polarized light, the MCD selection rule is $\Delta m = +1$, which corresponds to the transition from $m_s = -1/2$ (ground state) to $m_s = +1/2$ (excited state). The second transition indicated in Figure 2b corresponds to right circular polarized light with the selection rule $\Delta m = -1$. Because the splitting of the $m_s = \pm 1/2$ sublevels is small compared with the thermal energy at high temperature, both components with $m_s = -1/2$ and $m_s = +1/2$ of the ground state are equally populated and the intensity difference between the $\Delta m = +1$ and $\Delta m = -1$ transition (the MCD intensity) is zero. (A very weak derivative shaped MCD signal will be observed at high temperatures because of the difference in energy between the $\Delta m = +1$ and $\Delta m = -1$ transition.) At lower temperatures, the $m_s = -1/2$ component at lower energy will become preferably Boltzmann populated, creating an MCD signal that is then dependent on the temperature and field corresponding to changes of the relative populations of the $m_s = \pm 1/2$ sublevels of $|A\rangle$. At very low temperatures and high magnetic fields, only the $m_s = -1/2$ component will be populated and the MCD

signal reaches its intensity maximum; this is known as saturation. For an $S = 1/2$ system, this behaviour is described by the equation [5•]:

$$\frac{\Delta\epsilon_{av}}{E} = \frac{\text{const}}{4\pi} \int_{\theta} \int_{\phi} \tanh\left(\frac{\gamma\beta H}{2kT}\right) \times \frac{\sin\theta}{\gamma} (I_x^2 g_x M_{yz}^{eff} + I_y^2 g_y M_{xz}^{eff} + I_z^2 g_z M_{xy}^{eff}) d\theta d\phi \quad (1)$$

with $E = h\nu$ being the energy of the incident light; **const** is a collection of constants; θ and ϕ are the angles between the incident light and the molecular z axis and xy plane, respectively; I_x , I_y and I_z describe the orientation of the magnetic field relative to the molecular coordinate system; g_x , g_y and g_z are the g -values of the molecule; M_{ij}^{eff} are products of the relative polarizations of two electronic transitions (see below) and γ is defined:

$$\gamma = \sqrt{(G_x^2 + G_y^2 + G_z^2)}$$

and $G_p = I_p g_p$ with $p = x, y, z$. As can be seen from Equation 1, all the VTVH isotherms of a single transition recorded at different temperatures will overlay when plotted against $\beta H/2kT$. This means that the curve shown in Figure 2b not only represents the isotherm at 2K of the C term signal in Figure 2a, but also all isotherms recorded at other temperatures. The shape of the isotherm is related to the g -values of the system and the products of the relative polarizations (cf. Equation 1). Two perpendicular transition dipole moments are needed for non-zero MCD intensity.

In a low-symmetry protein active site in which all transitions are unidirectional, this is achieved by spin-orbit coupling of the excited state $|J\rangle$ to another intermediate excited state $|K\rangle$. (There is a second mechanism for MCD intensity, which is based on spin-orbit coupling between the ground state $|A\rangle$ and an intermediate excited state $|K\rangle$; see [5**].) This way, the transition moment of the excitation from the ground state $|A\rangle$ to $|K\rangle$ (m_y^{KJ} ; in this example y polarized) is mixed into m_x^{AJ} for the transition from $|A\rangle$ to $|J\rangle$ (for this example x polarized). Importantly, the spin-orbit coupling between $|J\rangle$ and $|K\rangle$ (corresponding to the matrix element \bar{L}_z^{KJ}) has to be effective in the direction *orthogonal* to the plane formed by the two transition dipole moments. In this example, the corresponding effective polarization product is defined as:

$$M_{xy}^{eff} = m_x^{AJ} m_y^{KJ} \bar{L}_z^{KJ} \Delta_{KJ}^{-1}$$

with $\Delta_{KJ} = E_K - E_J$. As presented above, the products of the relative polarizations M_{ij}^{eff} are extracted from the shapes of the VTVH saturation curves (see below). A complementary methodology has also been developed to determine relative polarizations from Raman-detected EPR spectroscopy for $S = 1/2$ systems [14•,15], which is particularly useful for systems with small g anisotropies.

In the case of a system with $S > 1/2$, there is an important additional property of the VTVH saturation magnetization data of **C** term signals, as shown in Figure 2c: the isotherms recorded at different temperatures do not necessarily overlap; the set of saturation curves is ‘nested’. This is caused by ZFS of the ground state, as indicated in the insert in Figure 2c for a $S = 5/2$ system. ZFS is described by the Spin-Hamiltonian [16]:

$$H = D(\mathcal{S}_z^2 - \frac{1}{3}\mathcal{S}^2) + E(\mathcal{S}_x^2 - \mathcal{S}_y^2) \quad (2)$$

with D being the axial and E the rhombic ZFS parameter ($0 \leq E \leq 1/3 D$) and the \mathcal{S} are spin operators. D and E are calculated from the elements D_{ii} of the diagonalized **D** tensor with the equations:

$$D = D_{zz} - \frac{1}{2}(D_{xx} + D_{yy})$$

$$E = \frac{1}{2}(D_{xx} - D_{yy})$$

The isotherms in Figure 2c have been simulated for the simple case of negative axial ZFS ($E = 0$) and an xy-polarized ($M_{xy}^{eff} \neq 0$) **C** term. Because of the axial ZFS, the ground state is split into three doublets corresponding to the three $M_s = \pm 5/2$, $\pm 3/2$ and $\pm 1/2$ pairs with the $M_s = \pm 5/2$ doublet at lowest energy, as shown in Figure 2c. The nesting of the saturation isotherms is then caused by changes in the populations of the six $|SM_s\rangle$ sublevels of the ground state with temperature and field. To simulate the VTVH curves, the energy changes of the $|SM_s\rangle$ functions with field and their field-induced mixing has to be taken into account. This is achieved by adding the Zeeman term to the Spin-Hamiltonian in Equation 2 [16]:

$$H = D(\mathcal{S}_z^2 - \frac{1}{3}\mathcal{S}^2) + E(\mathcal{S}_x^2 - \mathcal{S}_y^2) + \beta(g_x H_x \mathcal{S}_x + g_y H_y \mathcal{S}_y + g_z H_z \mathcal{S}_z) \quad (3)$$

By solving this Spin-Hamiltonian at a given field, the energies of the six resulting sublevels and the corresponding spin functions can be calculated; these have the general form:

$$\Theta_i = \sum_{j=1}^6 c_j |SM_s\rangle_j \quad (i = 1-6) \quad (4)$$

With these functions and their energies, the saturation isotherms can be simulated using the general equation [5**]:

$$\frac{\Delta \epsilon_{\alpha\beta}}{E} = \frac{\text{const}}{4\pi S} \int_0^{\pi} \int_0^{2\pi} \sum_i N_i \langle \mathcal{S}_x \rangle_i M_{yz}^{eff} + l_y \langle \mathcal{S}_y \rangle_i M_{xz}^{eff} + l_z \langle \mathcal{S}_z \rangle_i M_{xy}^{eff} \sin\theta d\theta d\phi \quad (5)$$

with the sum over i running over the sublevels of the ground state (for $S = 5/2$ the sum runs over the six functions in Equation 4); the N_i are the Boltzmann populations of the spin states i and the $\langle \mathcal{S}_k \rangle_i = \langle \Theta_i | \mathcal{S}_k | \Theta_i \rangle$ are spin expectation values. (Note that Equation 1 is a special case of Equation 5. In the case of an $S = 1/2$ system, the spin expectation values are related to the g-values of the system: $\langle \mathcal{S} \rangle_{1,2} = \mp 1/2 \gamma^{-1}$ with γ being a function of the g-values (see above). The Boltzmann populations N_i are directly included in the form of the tanh expression in Equation 1.)

Equation 5 explains why the isotherms at lower temperature in Figure 2c saturate at higher intensity. Because the ZFS is axial and the transition is xy-polarized, only the third term in Equation 5 contributes ($l_z \langle \mathcal{S}_z \rangle_i M_{xy}^{eff}$). The spin expectation value of the $M_s = \pm 5/2$ doublet at lowest energy, for example:

$$\langle \mathcal{S}_z \rangle = \left\langle S = \frac{5}{2}; M_s = -\frac{5}{2} \left| \mathcal{S}_z \right| S = \frac{5}{2}; M_s = -\frac{5}{2} \right\rangle = -\frac{5}{2}$$

is larger than the corresponding value of the two other doublets, and because lower temperature leads to higher population of the $M_s = \pm 5/2$ doublet, this will lead to an increase of the MCD intensity. Because the doublets split in a magnetic field, this effect is also field-dependent and, overall, this leads to the nesting of the VTVH data in Figure 2c.

Determination of relative polarizations from VTVH MCD

As shown by Equation 1 for an $S = 1/2$ center, the curvature of the VTVH isotherms is related to the g-values of the electronic groundstate and products of relative polarizations. In the case of $S > 1/2$, the Spin-Hamiltonian parameters D and E are needed to describe the electronic groundstate sublevels in Equation 5, and the ZFS can lead to a nesting of the saturation curves. Using Equation 1 and 5, respectively, the ground state

parameters (*g*-values and Spin-Hamiltonian parameters *D* and *E*) and the products of the relative polarizations can be derived by fitting the VTVH data. However, it is better to determine the *g*-values and Spin-Hamiltonian parameters from temperature-dependent EPR spectroscopy and then use these as input to fit the VTVH curves. This way, the number of parameters can be significantly reduced and the polarizations calculated from the fitting procedure are more reliable. The procedure to get the relative polarizations from VTVH data is as follows:

1. The *g*-values and/or Spin-Hamiltonian parameters *D* and *E* are determined from temperature-dependent EPR spectroscopy.

2. In the case of $S > 1/2$ systems, diagonalization of the Spin-Hamiltonian (Equation 3) to determine the spin functions (Equation 4) and their energies and the spin expectation values $\langle \mathcal{S}_k \rangle$.

3. Fitting the VTVH isotherms with Equation 1 ($S = 1/2$) and Equation 5 ($S > 1/2$) then leads to the relative polarization products M_{ij}^{eff} .

The percentage of *i*-polarization for the transition from $|A\rangle$ to $|J\rangle$ can then be calculated from the M_{ij}^{eff} using Equation 6 (for $i = x$) [5**]. Cyclic permutation of the indices gives the other polarizations.

$$\%x = 100 \times \frac{(M_{xy}^{eff} M_{xz}^{eff})^2}{(M_{xy}^{eff} M_{xz}^{eff})^2 + (M_{xy}^{eff} M_{yz}^{eff})^2 + (M_{xz}^{eff} M_{yz}^{eff})^2} \quad (6)$$

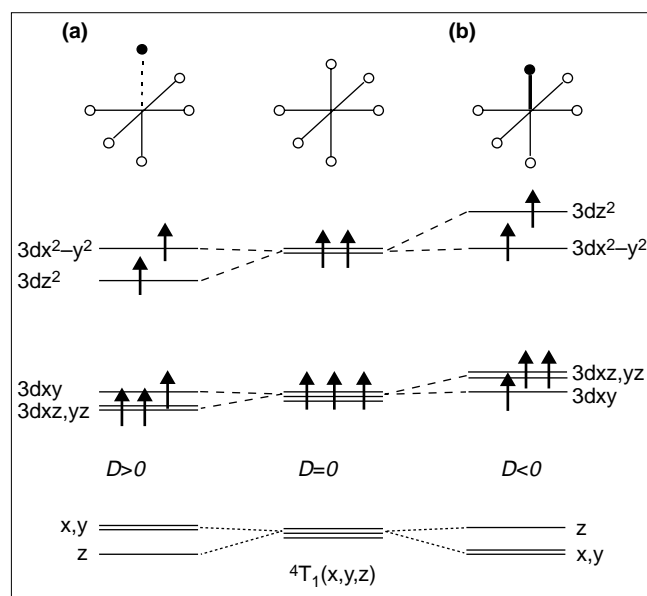
This formula is strictly valid only in the case that the excited state dominantly spin-orbit couples to one intermediate state $|K\rangle$. Otherwise, quantum-mechanical interference between different contributions has to be taken into account. It is important to point out that the polarization products and therefore also the polarizations determined from Equation 6 are relative because they are given in a coordinate system defined by the electronic ground state wavefunction. This means that for $S = 1/2$ systems (Equation 1) they are given in the coordinate system of the **g** matrix and in $S > 1/2$ species they are related to the coordinate system of the **D** tensor (Equation 5) [5**]. In order to get absolute polarizations, the orientation of the **g** matrix or **D** tensor must be determined in the molecular frame.

Determination of absolute polarizations

The absolute orientation of the **g** matrix and the **D** tensor can be measured with single-crystal EPR spectroscopy. But, as already mentioned, this depends on the availability of single crystals. Alternatively, it is possible to calculate the orientation of the **g** matrix and the **D** tensor in the molecule by quantum chemical methods.

In general, the elements of the **D** tensor are defined as [8**]:

Figure 3



Relationship between the electronic structure of a high-spin ferric center (energy splittings of the d orbitals and of the $4T_1$ ligand-field excited states) and the sign of *D* within the pure ligand-field model of Griffith [17]. (a) Weak axial-ligand case. (b) Strong axial-ligand case. Reprinted from [3] with permission. Copyright 2000 American Chemical Society.

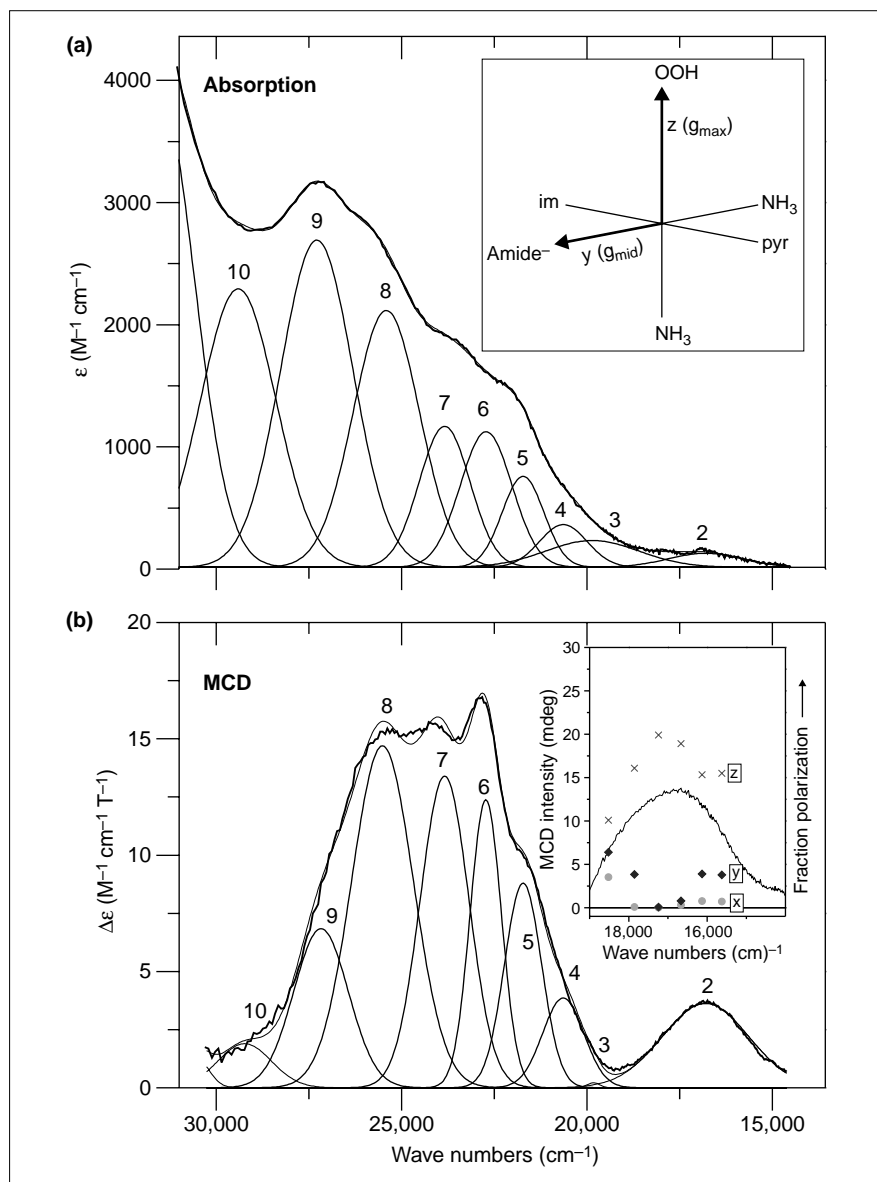
$$D_{pq}^{(0;\pm 1)} \sim - \sum_B \Delta_B^{-1} \langle AS_A M_{S,A} | H_{SOC}^p | BS_B M_{S,B} \rangle \times \langle BS_B M_{S,B} | H_{SOC}^q | AS_A M_{S,A} \rangle \quad (7)$$

with $|AS_A M_{S,A}\rangle$ being the ground state function of total spin S_A and corresponding $M_{S,A}$ value; the $|BS_B M_{S,B}\rangle$ are the excited states that appear in the sum over *B*; the indices (*p,q*) = *x,y,z* refer to the Cartesian components of the **D** tensor; H_{SOC}^p is the spin-orbit coupling operator and $\Delta_B = E_B - E_A$. The elements of the $\Delta \mathbf{g}$ matrix that define the shifts of the *g*-values relative to the free electron value (2.00) are obtained from the equation [8**]:

$$\Delta g_{pq} \sim - \sum_B \Delta_B^{-1} \left[\langle AS_A M_{S,A} | L^p | BS_B M_{S,B} \rangle \times \langle BS_B M_{S,B} | H_{SOC}^q | AS_A M_{S,A} \rangle + \langle AS_A M_{S,A} | H_{SOC}^p | BS_B M_{S,B} \rangle \langle BS_B M_{S,B} | L^q | AS_A M_{S,A} \rangle \right] \quad (8)$$

with L^p being the orbital angular momentum operator. The elements of the **D** tensor in Equation 7 arise from products of spin-orbit coupling matrix elements, whereas the *g* shifts in Equation 8 emerge from products of spin-orbit coupling and Zeeman matrix elements. This is the reason why only excited states of the same total spin as the ground state ($S_B = S_A$) contribute to the $\Delta \mathbf{g}$ matrix, whereas the **D** tensor has additional contributions from states with $S_B = S_A \pm 1$.

Figure 4



Absorption (a) and MCD (b) spectra of activated BLM. The insert in the top panel shows the computed orientation of the \mathbf{g} matrix in the simplified ABLM model used for the electronic structure calculation. (im, imidazole; pyr, pyridine.) The insert in the bottom panel shows the absolute polarizations (within the coordinate system of the \mathbf{g} matrix) for the 16,800 cm^{-1} MCD signal. Reprinted from [22*] with permission. Copyright 2000 American Chemical Society.

In the case of six-coordinate high-spin Fe(III) with an $S = 5/2$ ground state, a pure ligand-field model was developed [17] that interprets the observed ZFS in terms of second-order spin orbit coupling of the 6A_1 ground state with 4T_1 excited states in accordance with Equation 7 (with $B = {}^4T_1$). As can be seen in Figure 3, the splitting of the lowest excited 4T_1 state, which arises from distortions from octahedral symmetry leads, by spin-orbit coupling, to a ZFS of the 6A_1 ground state. In this simple ligand-field model, the sign of the Spin-Hamiltonian parameter D is directly related to the splittings of the d orbitals due to the geometry of the complex (*cf.* Figure 3). Importantly, experimental data have shown that this pure ligand-field model can lead to wrong predictions even of the sign of the ZFS [18–20]. This derives from the fact that the spin-orbit coupling to the excited states can be

anisotropic ($\mathbf{H}_{SOC}^p \neq \mathbf{H}_{SOC}^q$) because of differences in the covalencies of the different d functions of the metal. Orbitals that are ‘diluted’ by large covalent admixtures of ligand orbitals will have significantly lower contributions to spin-orbit coupling. This leads to the expressions for the Spin-Hamiltonian parameters D and E in Equation 9 [20,21]:

$$D = \frac{(\zeta_{\text{Fe}^{3+}})^2}{10} \left[\frac{2\kappa_z^2}{E({}^4T_1(z))} - \frac{\kappa_y^2}{E({}^4T_1(y))} - \frac{\kappa_x^2}{E({}^4T_1(x))} \right]$$

$$E = \frac{(\zeta_{\text{Fe}^{3+}})^2}{10} \left[\frac{\kappa_y^2}{E({}^4T_1(y))} - \frac{\kappa_x^2}{E({}^4T_1(x))} \right] \quad (9)$$

with the orbital reduction factors κ_p being defined as:

$$\begin{aligned}\kappa_z^2 &= (1-\beta^2)(1-\varepsilon^2) \\ \kappa_x^2 &= \left[\frac{\sqrt{(1-\xi^2)(1-\varepsilon^2)}}{4} + \frac{\sqrt[3]{(1-\xi^2)(1-\theta^2)}}{4} \right]^2 \\ \kappa_y^2 &= \left[\frac{\sqrt{(1-\eta^2)(1-\varepsilon^2)}}{4} + \frac{\sqrt[3]{(1-\eta^2)(1-\theta^2)}}{4} \right]^2\end{aligned}$$

Here, β^2 , ξ^2 , η^2 , ε^2 and θ^2 represent the ligand character in the iron d_{xy} , d_{yz} , d_{xz} , $d_{x^2-y^2}$ and d_{z^2} orbitals, respectively. Note that Equation 9 becomes equivalent to Griffith's pure ligand field model [17] when $\kappa_z^2, \kappa_x^2, \kappa_y^2 = 1$. This equation has been derived from Equation 7 in terms of molecular orbitals [8,19]. In a more general picture, the orbital reduction factors contain several effects in a real complex that are not included in the ligand field model [8**]. The differential d orbital covalencies lead to anisotropic spin-orbit coupling (see above) and a reduction of the spin-orbit coupling constant ζ compared with that of the free ion (up to 10%). This latter effect is caused by the charge donation by the ligands, which leads to a reduction of the effective nuclear charge on the metal and, hence, to an expansion of the metal radial wavefunctions. Finally, spin-orbit coupling on ligands with high atomic numbers (e.g. Br⁻) needs to be taken into account.

In addition to the model given in Equation 9, high-spin Fe(III) has a low lying sextet of excited CT states that may also play an important role by spin-orbit coupling with the ground state. Molecular orbital calculations based on Equation 7 and 8 include all these contributions and can be used to calculate the **g** matrix and the **D** tensor of a metal complex [8]. Diagonalization of these gives the orientation of their principal axes in the molecular structure. This information allows the conversion of the relative polarizations derived from MCD spectroscopy to absolute polarizations:

1. In the case of $S = \frac{1}{2}$ systems, the relative polarizations according to Equation 1 are given in terms of the principal axes of the **g** matrix. For $S > \frac{1}{2}$ systems fit with Equation 5, the polarizations are defined relative to the principal axes of the **D** tensor.
2. From the diagonalized **D** tensor, the Spin-Hamiltonian parameters D and E are obtained (see above), which can be directly related to the experimental values from EPR spectroscopy. If the data support the theoretical description, the **g** matrix and **D** tensor orientations in the molecular structure can be used to get absolute polarizations.

An example: activated bleomycin

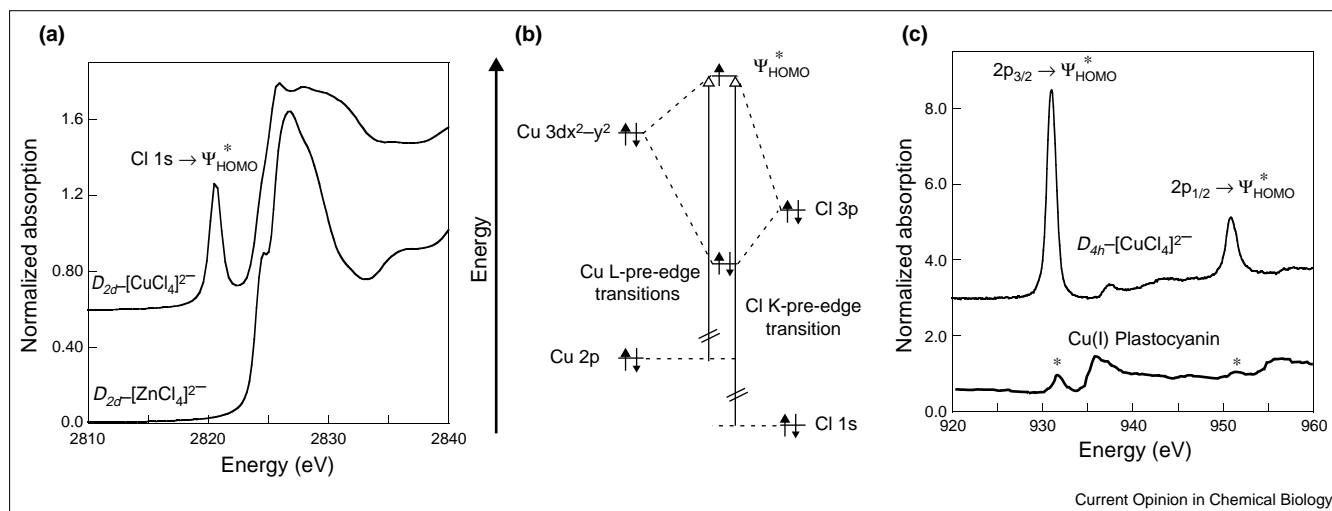
ABLM [22*] is, at present, the only well characterized non-heme iron oxygen intermediate [3]. It has been shown to be kinetically competent to cleave DNA by H-atom abstraction. Its absorption spectrum is shown in Figure 4a. It is very similar to Fe(III)(BLM) (bleomycin; data not shown), but has a new weak absorption feature

around 16,800 cm⁻¹ (band 2). The differences between ABLM and Fe(III)(BLM) are more pronounced in the MCD spectrum, in which band 2 corresponds to a relatively intense **C** term feature as shown in Figure 4b. The Raman spectrum recorded in the region of band 2 does not show resonance enhancement because of the low extinction coefficient of this absorption band ($\epsilon \sim 100 \text{ M}^{-1} \text{ cm}^{-1}$). Using the above VTVH MCD methodology, polarizations at six energies over the range of band 2 have been determined. The insert in Figure 4a shows the orientation of the **g** matrix in the ABLM molecule calculated from INDO/S-CI using Equation 8. The derived absolute polarizations in the range of band 2 are given in the insert of Figure 4b, showing that band 2 has different overlapping contributions but is mainly z polarized. Because the z axis is oriented along the Fe-hydroperoxo bond, this feature is assigned as a hydroperoxo-to-Fe(III) CT transition. Therefore, this absorption band provides a direct probe of the Fe(III)-OOH bond in ABLM. Electronic structure calculations based on these spectroscopic data show that hydroperoxo bonding in the non-heme iron intermediate ABLM is very different compared with in heme systems. This directly relates to the reactivity of these intermediates. Heterolytic cleavage of the O-O bond is known to occur for heme systems; however, this is a high-energy process in the non-heme environment. Alternatively, ABLM appears to be activated for the direct H-atom abstraction from substrate by the hydroperoxo ligand.

Covalency of ligand-metal bonds (metal L-edge/ligand K-edge XAS)

XAS spectroscopy involves the photoexcitation of core electrons to partially occupied or unoccupied valence orbitals and to the continuum. Perhaps the most well known XAS method is metal K-edge XAS, which can provide information about the oxidation state, spin-state, and coordination number of the metal center. However, metal K-edge XAS is a relatively low resolution probe of the electronic structure because of both the high energy of the technique and the fact that the $1s \rightarrow 3d$ pre-edge transition is not electric dipole allowed. A more detailed understanding of electronic structure is provided by ligand K-edge ($1s \rightarrow 3p + \text{continuum}$) and metal L-edge ($2p \rightarrow 3d + \text{continuum}$) XAS spectroscopies, two complementary methods that provide quantitative electronic structural insight because of both the improved resolution of experiments at lower energies and the electric-dipole-allowed nature of the transitions involved. The intensity of the ligand K-edge pre-edge feature is a direct experimental measure of the ligand covalency, [23**,24], whereas the intensity of metal L-edge features reflects the metal d character in the highest-occupied molecular orbital (HOMO) [25]. Hence, together these two methods can provide a quantitative description of the ground state wave function of a complex [26**,27**]. These methods are first discussed using $[\text{CuCl}_4]^{2-}$ as a well-defined reference and then applied to the Cu_A center.

Figure 5



Ligand K-edge and metal L-edge XAS. (a) A comparison of the Cl K-edge spectra of $[\text{ZnCl}_4]^{2-}$ and $D_{2d}\text{-}[\text{Cu}^{\text{II}}\text{Cl}_4]^{2-}$. (b) Molecular orbital diagram showing the ligand K- and metal L- pre-edge transitions.

(c) A comparison of the Cu K-edge spectra of $D_{4h}\text{-}[\text{Cu}^{\text{II}}\text{Cl}_4]^{2-}$ and Cu(I) plastocyanin. Features marked with an asterisk reflect the presence of a small amount of Cu^{II} .

Ligand K-edge XAS

A comparison of the Cl K-edge spectra of $D_{2d}\text{-}[\text{Zn}^{\text{II}}\text{Cl}_4]$ and $D_{2d}\text{-}[\text{Cu}^{\text{II}}\text{Cl}_4]$ is shown in Figure 5a [24]. Both complexes exhibit an edge jump at ~ 2823 eV with a maximum at ~ 2827 eV. However, only the copper(II) complex exhibits a low-energy feature at ~ 2820 eV. Because Zn^{II} has a d^{10} electron configuration, the lowest unoccupied energy levels are the 4s and 4p orbitals. Hence, the intense edge jump observed in both complexes is attributed to the electric-dipole-allowed $\text{Cl } 1s \rightarrow \text{Cl } 4p$ transition. The additional low-energy pre-edge peak present in the copper complex, but not the zinc complex, results from the d^9 electron configuration of Cu^{II} , which allows for a transition into the hole in the d-manifold. Hence, the pre-edge transition can be considered a $\text{Cl } 1s \rightarrow \text{Cu } dx^2-y^2$ transition. However, because the $\text{Cl } 1s$ orbital is highly localized, this transition can only have intensity if the $\text{Cu } dx^2-y^2$ orbital contains a significant contribution of $\text{Cl } 3p$ character because of covalency. As shown in Figure 5b, the bonding interaction between the $\text{Cu } dx^2-y^2$ and the $\text{Cl } 3p$ orbital gives rise to a half-occupied antibonding wave function:

$$\Psi_{\text{HOMO}}^* = (1 - \alpha^2)^{1/2} \left| \text{Cu } 3d_{x^2-y^2} \right\rangle - \alpha \left| \text{Cl } 3p \right\rangle \quad (10)$$

$$\text{Int}(\text{Cl}1s \rightarrow \Psi^*) = \text{const} \left| \left\langle \text{Cl}1s \left| r \right| \Psi^* \right\rangle \right|^2 \quad (11a)$$

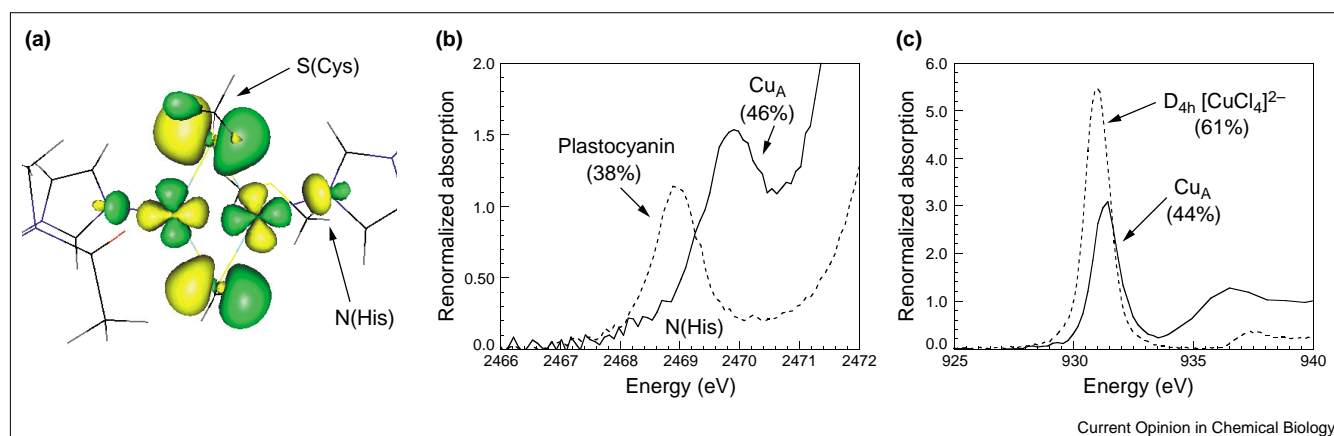
$$= \alpha^2 \text{const} \left| \left\langle \text{Cl}1s \left| r \right| \text{Cl}3p \right\rangle \right|^2 \quad (11b)$$

where α^2 represents the $\text{Cl } 3p$ character in the normalized symmetry-adapted molecular orbital encompassing the four Cl ligands. Hence the pre-edge transition is more appropriately described as a $1s \rightarrow \Psi^*$ transition, which gains

intensity from $\text{Cl } 3p$ mixing into the Ψ^* wavefunction. The electric dipole intensity for this transition is given by Equation 11a. Substituting Ψ^* from Equation 10 and accounting for the localized nature of the transition gives Equation 11b, where $\text{const} \left| \left\langle \text{Cl } 1s \left| r \right| \text{Cl } 3p \right\rangle \right|^2$ is the intensity of the pure Cl-centered $1s \rightarrow 3p$ transition. The intensity of the pre-edge peak is then the intensity of the pure $\text{Cl } 1s$ to $3p$ transition weighted by α^2 , the covalent character contained in the antibonding molecular orbital. Thus, ligand K-edge XAS spectroscopy provides a direct probe of the covalency of a metal-ligand bond, which can be quantified using $D_{2d}\text{-}[\text{Cu}^{\text{II}}\text{Cl}_4]$ as a well-defined reference. The covalency of $D_{2d}\text{-}[\text{Cu}^{\text{II}}\text{Cl}_4]$ has been probed by a number of spectroscopic techniques [28,29] including EPR, absorption and photoelectron spectroscopy. Using these techniques, an experimental value for the $\text{Cl } 3p$ character (30%) has been obtained, and has been used to quantify the Cl covalency of other Cl-containing transition-metal sites by Cl K-edge XAS. Similar references have been developed for thiolate-containing [30] and sulfide-containing [31*] compounds. For the Cu_A center discussed later, plastocyanin is used as a thiolate reference compound with 38% S $3p$ character [30].

It should also be noted that the energy of a ligand K-edge transition provides important electronic structural information [23*,32]. The pre-edge energy is affected by the energy of the HOMO (which has contributions from the ligand field and Z_{eff}) and the energy of the ligand $1s$ core. In addition, the ligand K-edge rising edge energy reflects the chemical shifts in the ligand $1s$ core. Thus, by evaluating changes in edge and pre-edge energies, changes in the HOMO energy can be directly obtained.

Figure 6



Theoretical and experimental electronic structure of the Cu_A center. (a) Half-occupied HOMO of the Cu_A site. (b) A comparison of the renormalized S K-edge spectra of Cu_A and plastocyanin. (c) Renormalized Cu L-edge spectra of $\text{D}_{4h}\text{[CuCl}_4\text{]}^{2-}$ and Cu_A .

Metal L-edge XAS

Figure 5c shows the L-edge spectrum of $\text{D}_{4h}\text{[Cu}^{\text{II}}\text{Cl}_4\text{]}$. The intense pre-edge features at ~ 930 and ~ 950 eV arise from the electric-dipole-allowed $\text{Cu } 2p \rightarrow \text{Cu } 3d_{x^2-y^2}$ transition. These features, corresponding to the L_3 and L_2 edges, are split by ~ 20 eV because of the spin orbit coupling of the $2p$ hole (i.e. the L_3 and L_2 edges arise from transitions producing $2p_{3/2}$ and $2p_{1/2}$ hole final states, respectively). For comparison, Figure 5c also shows the L-edge spectrum of a Cu^{I} complex (reduced plastocyanin) [25]. Because Cu^{I} has a d^{10} electron configuration, the d subshell is filled and no intense $2p \rightarrow 3d$ transitions are observed (though weak $2p \rightarrow 4s$ transitions are observed) verifying that, in the Cu^{II} case, the intense transitions are to the half-occupied HOMO in Figure 5b. The intensity of the Cu^{II} L_3 and L_2 pre-edge peaks can be interpreted in a manner analogous to the ligand K-edge data. The electric dipole allowed intensity for this transition is given by Equation 12a:

$$\text{Int}(\text{Cu } 2p \rightarrow \Psi^*) = \text{const} \left\langle \left\langle \text{Cu } 2p | \mathbf{r} | \Psi^* \right\rangle \right\rangle^2 \quad (12a)$$

$$= (1 - \alpha^2) \text{const} \left\langle \left\langle \text{Cu } 2p | \mathbf{r} | \text{Cu } 3d_{x^2-y^2} \right\rangle \right\rangle^2 \quad (12b)$$

Substituting Ψ^* from Equation 10 and accounting for the localized nature of the transition gives equation 12b, where

$$\text{const} \left\langle \left\langle \text{Cu } 2p | \mathbf{r} | \text{Cu } 3d_{x^2-y^2} \right\rangle \right\rangle^2$$

is the intensity of the pure Cu-centered $2p \rightarrow 3d_{x^2-y^2}$ transition. The intensity of the L_3 and L_2 pre-edge peaks is then the intensity of the pure Cu $2p$ to $3d_{x^2-y^2}$ transition weighted by $1 - \alpha^2$, the metal d character contained in the antibonding molecular orbital. Using $\text{D}_{4h}\text{[Cu}^{\text{II}}\text{Cl}_4\text{]}$ as a well-defined reference with $\sim 61\%$ Cu $d_{x^2-y^2}$ character, this method has been used to determine the metal d character

in $\text{D}_{2d}\text{[Cu}^{\text{II}}\text{Cl}_4\text{]}$ [25], plastocyanin [25], and most recently Cu_A [33*]. The application of this methodology to Cu_A is discussed in the next section.

The energies of the L_3 and L_2 pre-edge peaks also vary with the environment of the metal site. A change in Z_{eff} , because of a change in oxidation state or in coordination number, will affect the energy of both the $2p$ and the HOMO, whereas a change in the splitting of the d -manifold will only effect the HOMO energy. Combining an analysis of metal L-edge and ligand K-edge energies allows the specific contributions to the HOMO energy to be elucidated.

Application to the Cu_A center

Cu_A centers [34–36] serve as the electron uptake site in cytochrome *c* oxidase and also as a redox center in nitrous oxide reductase. The Cu_A site is a completely delocalized binuclear center [37] (Figure 6a) in its oxidized state with two $\text{Cu}^{1.5+}$ separated by ~ 2.4 Å and bridged by two S(Cys). Our studies have focused on understanding the electronic structure of Cu_A and its contribution to function [33*,38,39]. Combined S K-edge and Cu L-edge studies [33*] provide the opportunity to obtain an experimental description of the ground-state wavefunction of Cu_A . Figure 6b and c show the renormalized S K-edge and Cu L-edge spectra of Cu_A and the relevant standards. (The S K-edge data are renormalized to account for the fact that a different number of sulfur atoms contribute to the pre-edge and edge features. In addition, both the S K- and Cu L-edge data are renormalized to one d-hole.) Analysis of the S K-edge data shows a total of 46% S character in the half-occupied HOMO, which is distributed over the two sulfur atoms. Using the L-edge methodology, it is found that there is 44% Cu d character in the HOMO, which is delocalized over the two coppers. This delocalization lowers both the inner- and outer-sphere reorganization energy and contributes to the ET function of

Cu_A. Further evidence for the delocalization in Cu_A comes from analysis of the Cu L- and S K- pre-edge energies (combined with MCD data), which indicate an ~0.4 eV contribution to the HOMO because of metal-metal bonding (σ^* interaction in Figure 6a).

In addition, the nature of the ground-state wavefunction of Cu_A has important implications for both intra- and intermolecular electron transfer in cytochrome *c* oxidase. Comparison of the S K-edge results with N ENDOR results [40] (which show ~4% total N covalency), indicate a redox active orbital with highly anisotropic covalency. This anisotropy must be included in the analysis of electron transfer pathways by weighting the electron transfer rates by the appropriate ligand character. By allowing for this effect, a path through the Cys200 (using the residue numbering from bovine cytochrome *c* oxidase [41]) can become competitive with the shorter His161 path in the intramolecular electron transfer path in cytochrome *c* oxidase (Cu_A→heme *a*). Further, the highly covalent Cu-S bond is particularly important for activating the intermolecular electron transfer path from heme *c*→Cu_A.

Conclusions

Different energy regions in Figure 1 provide complementary information on a transition metal complex. Thus, an appropriate combination of spectroscopic methods are required for maximum insight into active-site geometric and electronic structure. Electronic structure calculations provide an important complement to spectroscopy and, when supported by data, provide total energy comparisons and insight into reaction coordinates. Often metalloenzymes exhibit unique spectroscopic features that reflect highly covalent sites, which activate the metal center for catalysis. New spectroscopic methodologies have been presented that enable one to assign these unique features (VTMH MCD/EPR/MOT) and to experimentally define the covalency of ligand-metal bonds (metal L-edge/ligand K-edge XAS).

Acknowledgements

We gratefully acknowledge the contributions of our co-workers and collaborators, who are cited in the referenced publications. In particular, we would like to thank Keith O Hodgson, Britt Hedman, and Frank Neese. This work was supported by NIH GM-40392 and NSF CHE-9980549 (EIS). NL thanks the Deutscher Akademischer Austauschdienst (DAAD) for a postdoctoral fellowship.

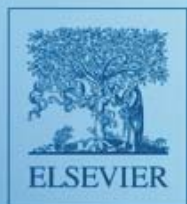
References and recommended reading

Papers of particular interest, published within the annual period of review, have been highlighted as:

- of special interest
- of outstanding interest

1. Solomon EI: **Inorganic spectroscopy – an overview.** *Comment Inorg Chem* 1984, 3:227-320.
2. Solomon EI, Hanson MA: **Bioinorganic spectroscopy.** In *Inorganic Electronic Structure and Spectroscopy Vol 2*. Edited by Solomon EI, Lever ABP. New York: John Wiley; 1999:1-129.
3. Solomon EI, Brunold TC, Davis MI, Kemsley JN, Lee S-K, Lehnert N, Neese F, Skulan AJ, Yang Y-S, Zhou J: **Geometric and electronic structure/function correlations in non-heme iron enzymes.** *Chem Rev* 2000, 1:235-349.
4. Hitchman MA, Riley MJ: **Polarized absorption spectroscopy.** In *Inorganic Electronic Structure and Spectroscopy Vol 1*. Edited by Solomon EI, Lever ABP. New York: John Wiley; 1999:213-258.
5. Neese F, Solomon EI: **MCD C-term signs, saturation behavior, and determination of band polarizations in randomly oriented systems with spin $S \geq 1/2$. Applications to $S = 1/2$ and $S = 5/2$.** *Inorg Chem* 1999, 38:1847-1865.
- General formulas are developed to fit the VTMH MCD C term isotherms in orthorhombic symmetry for spin-allowed transitions between orbitally non-degenerate states and $S \geq 1/2$. Analytic formulas for the $S = 1/2$ case are given. In all cases, the MCD intensity is proportional to the spin expectation values of the sublevels of the ground state. Applications to $S = 1/2$ and $S = 5/2$ systems are presented.
6. Oganessian VS, George SJ, Cheesman MR, Thomson AJ: **A novel, general method of analyzing magnetic circular dichroism spectra and magnetization curves of high-spin metal ions: application to the protein oxidized rubredoxin, *Desulfovibrio gigas*.** *J Chem Phys* 1999, 110:762-777.
- Formulas are developed to analyse the total MCD intensity (A, B and C terms) and VTMH saturation behaviour of spin-allowed transitions for $S \geq 1/2$ systems using irreducible tensor methods for symmetries higher than orthorhombic. Application to the tetrahedral high-spin Fe(III) site of oxidized rubredoxin from *Desulfovibrio gigas* is presented.
7. Oganessian VS, Thomson AJ: **Magnetic circular dichroism of symmetry and spin forbidden transitions of high-spin metal ions.** *J Chem Phys* 2000, 113:5003-5017.
- In this paper, the approach given in [6••] is extended to analyse the MCD intensities of spin-forbidden (and symmetry-forbidden) transitions. Under certain conditions, spin-forbidden transitions can have MCD intensities of comparable magnitude as spin-allowed transitions. Application to the tetrahedral high-spin Fe(III) site of rubredoxin from *Methanobacterium thermoautotrophium* (strain Marburg) is given.
8. Neese F, Solomon EI: **Calculation of zero-field splittings, g-values, and the relativistic nephelauxetic effect in transition metal complexes. Application to high-spin ferric complexes.** *Inorg Chem* 1998, 37:6568-6582.
- Based on the observation that anisotropic covalency plays an important role for the sign and magnitude of the ZFS parameters [18–21], general formulae are developed to calculate zero field splittings and g-values from MO and CI wavefunctions rather than pure ligand-field theory. This allows the determination of the orientation of the g matrix and the D tensor in the molecular framework. Applications to high-spin Fe(III) systems are presented and the different contributions to the ZFS and their magnitude and sign are discussed.
9. Stephens PJ: **Theory of magnetic circular dichroism.** *J Chem Phys* 1970, 52:3489-3516.
10. Stephens PJ: **Magnetic circular dichroism.** *Annu Rev Phys Chem* 1974, 25:201-232.
11. Stephens PJ: **Magnetic circular dichroism.** *Adv Chem Phys* 1976, 35:197-264.
12. Piepho SB, Schatz PN: *Group Theory in Spectroscopy: With Applications to Magnetic Circular Dichroism.* New York: John Wiley; 1983.
13. Solomon EI, Pavel EG, Loeb KE, Campochiaro C: **Magnetic circular dichroism spectroscopy as a probe of the geometric and electronic structure of non-heme ferrous enzymes.** *Coord Chem Rev* 1995, 144:369-460.
14. Bingham SJ, Gutschank J, Börger B, Suter D, Thomson AJ: **Magnetic circular dichroism anisotropy from coherent Raman detected electron paramagnetic resonance spectroscopy: application to spin-1/2 transition metal ion centers in proteins.** *J Chem Phys* 2000, 113:4331-4339.
- Application of coherent Raman-detected EPR spectroscopy to determine relative polarizations for $S = 1/2$ systems. General formulas for MCD C term intensity (for $S = 1/2$) are presented and extended to the case where the circular polarized light is within the direction of the microwave field and *orthogonal* to the external magnetic field. Experimental data on the low-spin ferric heme site of cytochrome *c*551 from *Pseudomonas aeruginosa* is presented as an example.
15. Bingham SJ, Börger B, Gutschank J, Suter D, Thomson AJ: **Probing the electronic structure of transition metal ion centres in proteins by coherent Raman-detected electron paramagnetic resonance spectroscopy.** *J Biol Inorg Chem* 2000, 5:30-35.
16. Abragam A, Bleaney B: *Electron Paramagnetic Resonance of Transition Ions.* New York: Dover Publications; 1986.

17. Griffith JS: *The Theory of Transition-Metal Ions*. Cambridge: Cambridge University Press; 1964.
18. Deaton JC, Gebhard MS, Koch SA, Millar M, Solomon EI: Ligand field transitions and the origin of zero field splitting in $[\text{PPh}_4][\text{FeCl}_4]$ and $[\text{NEt}_4][\text{Fe}(\text{SR})_4]$ ($\text{R} = 2,3,5,6\text{-Me}_4\text{C}_6\text{H}$): a model for the high-spin Fe(III) site in rubredoxin. *J Am Chem Soc* 1988, 110:6241-6243.
19. Deaton JC, Gebhard MS, Solomon EI: Transverse and longitudinal Zeeman effect on $[\text{PPh}_4][\text{FeCl}_4]$: assignment of the ligand field transitions and the origin of the $^6\text{A}_1$ ground-state zero-field splitting. *Inorg Chem* 1989, 28:877-889.
20. Gebhard MS, Deaton JC, Koch SA, Millar M, Solomon EI: Single crystal spectral studies of $[\text{Fe}(\text{SR})_4]^-$ ($\text{R} = 2,3,5,6\text{-Me}_4\text{C}_6\text{H}$): the electronic structure of the ferric tetrathiolate active site. *J Am Chem Soc* 1990, 112:2217-2231.
21. Zhang Y, Gebhard MS, Solomon EI: Spectroscopic studies of the non-heme ferric active site in soybean lipoxygenase: magnetic circular dichroism as a probe of electronic and geometric structure: ligand-field origin of zero-field splitting. *J Am Chem Soc* 1991, 113:5162-5175.
22. Neese F, Zaleski JM, Loeb-Zaleski K, Solomon EI: Electronic structure of activated bleomycin: oxygen intermediates in heme versus nonheme iron. *J Am Chem Soc* 2000, 122:11703-11724.
- Analysis of the spectral features of Fe(III)(BLM) and activated BLM (ABLM) and relation to the electronic structure of these two species. Based on this, the reactivity of ABLM is explored using quantum chemical methods and compared with the known reactivity of hemes. Importantly, the non-heme intermediate ABLM (a low-spin Fe(III)-hydroperoxo complex) does not undergo heterolytic cleavage of the O-O bond, but could directly react with the C-H bond of the DNA ribose sugar.
23. Glaser T, Hedman B, Hodgson KO, Solomon EI: Ligand K-edge X-ray absorption spectroscopy: a direct probe of ligand-metal covalency. *Acc Chem Res* 2000, 33:859-868.
- An overview of ligand K-edge methodology as developed in [24,29,30,31*] is presented. The methodology for determining covalency in one-electron (hole) and many electron systems is described and demonstrated for a series of model complexes and proteins.
24. Hedman B, Hodgson KO, Solomon EI: X-ray absorption edge spectroscopy of ligands bound to open-shell metal ions: chlorine K-edge studies of covalency in $\text{CuCl}_4(2-)$. *J Am Chem Soc* 1990, 112:1643-1645.
25. George SJ, Lowery MD, Solomon EI, Cramer SP: Copper L-edge spectral studies: a direct experimental probe of the ground state covalency in the blue copper site in plastocyanin. *J Am Chem Soc* 1993 115:2968-2969.
26. Randall DW, George SD, Hedman B, Hodgson KO, Fujisawa K, Solomon EI: Spectroscopic and electronic structural studies of blue copper model complexes. 1: perturbation of the thiolate-Cu bond. *J Am Chem Soc* 2000, 122:11620-11631.
- In these papers (see also [27**]) the metal L-edge methodology developed in [25] is combined with complementary S K-edge data in order to quantify metal and ligand covalencies for a set of blue copper model complexes.
27. Randall DW, George SD, Holland PL, Hodgson KO, Tolman WB, Solomon EI: Spectroscopic and electronic structural studies of blue copper model complexes. 2: Comparison of 3- and 4-coordinate Cu(II) thiolate complexes and fungal laccase. *J Am Chem Soc* 2000, 122:11632-11648.
- See annotation to [26**].
28. Didziulis SV, Cohen SL, Gewirth AA, Solomon EI: Variable photon energy photoelectron spectroscopic studies of copper chlorides: an experimental probe of metal-ligand bonding and changes in electronic structure on ionization. *J Am Chem Soc* 1988, 110:250-268.
29. Gewirth AA, Cohen SL, Schugar HJ, Solomon EI: Spectroscopic and theoretical studies of the unusual electron-paramagnetic-resonance parameters of distorted tetrahedral cupric sites: correlations to X-ray spectral features of core levels. *Inorg Chem* 1987, 26:1133-1146.
30. Shadle SE, Penner-Hahn JE, Schugar HJ, Hedman B, Hodgson KO, Solomon EI: X-ray absorption spectroscopic studies of the blue copper site: metal and ligand K-edge studies to probe the origin of the EPR hyperfine splitting in plastocyanin. *J Am Chem Soc* 1993, 115:767-776.
31. Rose K, Shadle ES, Glaser T, Vries SD, Cherepanov A, Canters GW, Hedman B, Hodgson KO, Solomon EI: Investigation of the electronic structure of 2Fe-2S model complexes and the Rieske protein using ligand K-edge X-ray absorption spectroscopy. *J Am Chem Soc* 1999, 121:2353-2363.
- S K-edge XAS is applied to a series of 2Fe-2S model complexes, and the sulfide and thiolate contributions to covalency are evaluated separately, by development of a reference for sulfide. This methodology is then applied to the Rieske protein.
32. Shadle SE, Hedman B, Hodgson KO, Solomon EI: Ligand K-edge X-ray-absorption spectroscopy as a probe of ligand-metal bonding: charge donation and covalency in copper-chloride systems. *Inorg Chem* 1994, 33:4235-4244.
33. George SD, Metz M, Szilagyi RK, Wang H, Cramer SP, Lu Y, Tolman WB, Hedman B, Hodgson KO, Solomon EI: A quantitative description of the ground state wave function of Cu_A by X-ray absorption spectroscopy: comparison to plastocyanin and relevance to electron transfer function. *J Am Chem Soc* 2001, in press.
- Using a combination of Cu L- and S K-edge XAS, a quantitative description of the ground-state wavefunction of Cu_A is obtained. These results, combined with DFT calculations, are correlated with the electron transfer function of Cu_A .
34. Ferguson-Miller S, Babcock GT: Heme/copper terminal oxidases. *Heme/Copper Terminal Oxidases* 1996, 96:2889-2907.
35. Beinert H: Copper A of cytochrome c oxidase, a novel, long-embattled, biological electron-transfer site. *Eur J Biochem* 1997, 245:521-532.
36. Ramirez BE, Malmström BG, Winkler JR, Gray HB: The currents of life: the terminal electron-transfer complex of respiration. *Proc Natl Acad Sci USA* 1995, 92:11949-11951.
37. Kroneck PMH, Antholine WE, Riestler J, Zumft WG: The cupric site in nitrous-oxide reductase contains a mixed-valence $[\text{Cu}(\text{II})\text{Cu}(\text{I})]$ binuclear center: a multifrequency electron-paramagnetic resonance investigation. *FEBS Lett* 1988, 242:70-74.
38. Gamelin DR, Randall DW, Hay MT, Houser RP, Mulder TC, Canters GW, DeVries S, Tolman WB, Lu Y, Solomon EI: Spectroscopy of mixed-valence Cu_A type centers: ligand-field control of ground-state properties related to electron-transfer. *J Am Chem Soc* 1998, 120:5246-5263.
39. Williams KR, Gamelin DR, LaCroix LB, Houser RP, Tolman WB, Mulder TC, DeVries S, Hedman B, Hodgson KO, Solomon EI: Influence of copper-sulfur covalency and copper-copper bonding on valence delocalization and electron-transfer in the Cu_A site of cytochrome c oxidase. *J Am Chem Soc* 1997, 119:613-614.
40. Gurbiel RJ, Fann YC, Surerus KK, Werst MM, Musser SM, Doan PE, Chan SI, Fee JA, Hoffman BM: Detection of two histidyl ligands to Cu_A of cytochrome oxidase by 35-GHz ENDOR: N-14, 15 and Cu-63,65 ENDOR studies of the Cu_A site in bovine heart cytochrome aa(3) and cytochrome caa(3) and cytochrome ba(3) from *Thermus thermophilus*. *J Am Chem Soc* 1993, 115:10888-10894.
41. Yoshikawa S, Shinzawa-Itoh K, Nakashima R, Yaono R, Yamashita E, Inoue N, Yao M, Fei MJ, Libeu CP, Mizushima T et al.: Redox-coupled crystal structural changes in bovine heart cytochrome c oxidase. *Science* 1998, 280:1723-1729.



Volume 110

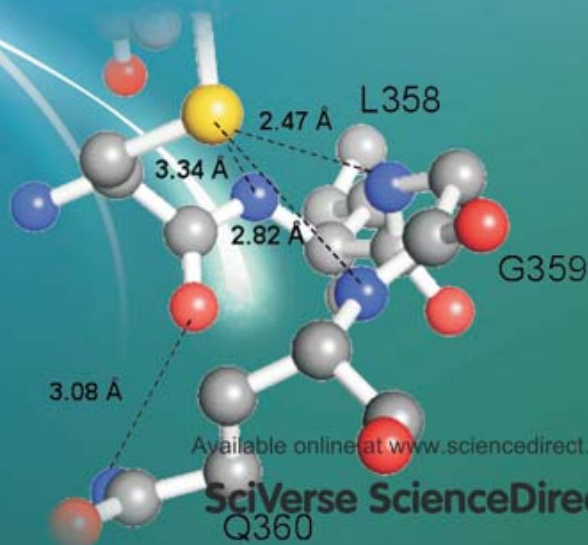
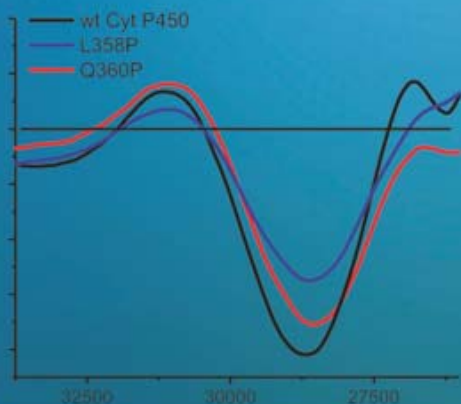
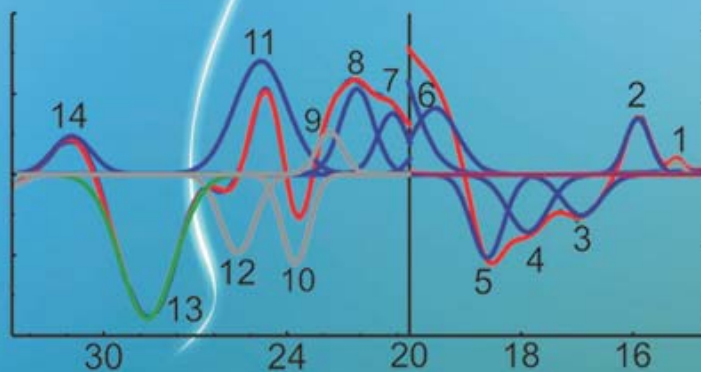
May 2012

ISSN 0162-0134

JOURNAL OF Inorganic Biochemistry

Early Career
Focused Review
by
Nicolai Lehnert

Editor: J.H. DAWSON





Focused review

Elucidating second coordination sphere effects in heme proteins using low-temperature magnetic circular dichroism spectroscopy

Nicolai Lehnert

Department of Chemistry, The University of Michigan, 930 North University Avenue, Ann Arbor, MI 48109-1055, USA

ARTICLE INFO

Article history:

Received 7 October 2011

Received in revised form 27 February 2012

Accepted 28 February 2012

Available online 10 March 2012

Keywords:

Heme proteins

Second coordination sphere effects

Hydrogen bonding

Magnetic circular dichroism spectroscopy

Cytochrome P450

Electronic structure

ABSTRACT

This paper reviews recent findings on how the second coordination sphere of heme proteins fine-tunes the properties of the heme active site via hydrogen bonding. This insight is obtained from low-temperature magnetic circular dichroism (MCD) spectroscopy. In the case of high-spin ferric hemes, MCD spectroscopy allows for the identification of a multitude of charge-transfer (CT) transitions. Using optically-detected magnetic saturation curves, out-of-plane polarized CT transitions between the heme and its axial ligand(s) can be identified. In the case of ferric Cytochrome P450cam, the corresponding $S(\sigma) \rightarrow Fe(III)$ CT transition can be used as a probe for the {Fe(III)-axial ligand} interaction, indicating that the hydrogen bonding network of the proximal Cys only plays a limited role for fine-tuning the Fe(III)-S(Cys) interaction. In the case of high-spin ferrous hemes with axial His/imidazole coordination, our MCD-spectroscopic investigations have uncovered a direct correlation between the strength of the hydrogen bond to the proximal imidazole ligand and the ground state of the complexes. With neutral imidazole coordination, the doubly occupied d-orbital of high-spin iron(II) is of d_{π} character, located orthogonal to the heme plane. As the strength of the hydrogen bond increases, this orbital rotates into the heme plane, changing the ground state of the complex.

© 2012 Elsevier Inc. All rights reserved.

1. Introduction

Second coordination sphere (SCS) effects in proteins and transition metal complexes correspond to interactions of the metal center and its primary ligands with groups that are not part of the intimate coordination environment of the metal. In proteins, SCS effects are usually mediated by amino acid side chains in the substrate (active site) pocket of the protein. The most important types of interactions are hydrogen bonding, electrostatic (between charged groups) and dipole interactions, steric interactions, and π -stacking of aromatic side chains. These interactions are used by proteins for substrate recognition (binding and precise orientation in the active site), for fine-tuning of ligand donor strengths and redox potentials of transition metal centers, to enforce unnatural coordination geometries on transition metal complexes (the 'entatic' state), for proton and electron transfer, etc. [1]. The most important SCS interaction is hydrogen bonding. A famous example in this respect is the distal His in hemoglobin (Hb) and myoglobin (Mb), which forms a hydrogen bond to dioxygen bound to the heme center, and in this way, stabilizes the oxy-Hb/Mb complex [2].

SCS effects, in particular hydrogen bonding, are generally thought to be used in nature to fine-tune the properties of all heme protein active sites. This pertains particularly to hydrogen bonds to either the axial ligand(s) of heme, heme side chains, or substrates bound to the heme

center. In this way, SCS effects allow principally similar active sites, like the {heme-thiolate(Cys)} active site in all members of the Cyt. P450 family or the {heme-imidazole(His)} active site in globins, (per)oxidases and heme sensor proteins, to perform a surprisingly diverse range of functions. This requires adjustments in the electronic structures, redox potentials, and reactivities of the {heme-axial ligand} (catalytic) units in these different proteins. Despite this central importance of hydrogen bonding for heme protein function, however, it has been found very difficult to obtain direct insight into how exactly hydrogen bonding affects the electronic structures and properties of heme protein active sites. For example, it has been observed frequently that changes in the hydrogen bonding network of axial ligands to heme can have a distinctive effect on redox potential [3–5], but it is not clear whether this relates to changes in heme-axial ligand bond strength, changes in ground state of the heme, changes in heme conformation, etc., and whether the ferrous or ferric oxidation state is primarily affected by the change (or both).

Magnetic Circular Dichroism (MCD) spectroscopy has long been used to elucidate the geometric and electronic structures of heme proteins [6–10]. In particular, MCD spectroscopy has been frequently applied as a 'finger-printing' technique to identify (a) the number and types of axial ligands bound to heme, (b) the oxidation and spin states of the heme, and (c) the heme conformation, in particular out-of-plane distortions of the heme. For example, in the low-spin ferric oxidation state of heme, low-energy (NIR) transitions are observed around $5000\text{--}10000\text{ cm}^{-1}$ that are characteristic for the axial ligands of heme [6,11–13]. In addition, axial thiolate coordination is easily identified from the MCD spectra [14].

E-mail address: lehnertn@umich.edu.

In order to utilize the full power of MCD spectroscopy, low-temperature (liquid helium) measurements of the temperature and field dependence of the paramagnetic MCD intensity, called **C-term** intensity, are necessary. In this way, magnetic saturation curves can be detected optically [15,16], and, as detailed below, the fitting of these magnetization data allows for the determination of the polarizations of the observed transitions, in samples of randomly oriented molecules (i.e. not requiring single-crystal measurements) [17–21]. As demonstrated in this review, this information, combined with TD-DFT calculations, can be used to assign the optical spectra of metalloporphyrins, and in particular, identify charge-transfer transitions between the iron center of heme and the axial ligand(s) [21]. In addition, the total MCD intensity is very sensitive to the exact nature of the ground state, and can be correlated with changes in electron distribution of the iron center [22,23]. In comparison to UV–visible (UV–vis) spectroscopy, MCD has the additional advantage that MCD intensity is a signed quantity, and hence, a much better resolution of the optical transitions of metalloporphyrins is usually achieved with this technique. Compared to EPR spectroscopy, MCD is not restricted to non-integer spin systems.

In the following, these strengths of low-temperature MCD spectroscopy are used to investigate how the electronic properties of hemes can be fine-tuned via SCS effects in proteins. Useful complementary techniques to further support the conclusions drawn from MCD in terms of spectral assignments and ground state properties are EPR [24,25] and resonance Raman (rR) spectroscopy [26,27], and DFT calculations. Here we focus on high-spin ferrous and ferric hemes, since these are the (catalytically) active states of many heme proteins involved in O₂ and small molecule binding and activation.

2. Low-temperature MCD spectroscopy

The theoretical background of MCD spectroscopy was developed by P. J. Stephens in the 1970s and has been summarized in a number of reviews and articles [8,13,16,17,20,28,29]. MCD spectroscopy measures the difference in absorption of left (lcp) and right (rcp) circular polarized light in an applied, longitudinal magnetic field, usually generated by a superconducting magnet. MCD intensity arises from three different mechanisms, designated as MCD **A**-, **B**- and **C**-terms, as shown in Eq. (1).

$$I \sim \left[A_1 \left(\frac{-\partial f(E)}{\partial E} \right) + \left(B_0 + \frac{C_0}{kT} \right) f(E) \right] \cdot B \quad (1)$$

Here, I is the MCD intensity, T the temperature, B the magnetic field and the function $f(E)$ represents the band shape of an absorption band. Importantly, the **A**- and **B**-terms are temperature independent, whereas MCD **C**-term intensity is temperature dependent. Due to the $1/T$ dependence, the dominant mechanism at low temperature is in fact the **C**-term. From Eq. (1), MCD intensity increases linearly with the strength of the magnetic field (B). This strictly applies to the **A**-

and **B**-terms. On the other hand, **C**-term intensity arises from a degenerate ground state, which is split in the applied magnetic field due to the Zeeman effect as shown in Scheme 1. Since the Jahn–Teller effect generally lifts orbital degeneracy of ground states, degenerate ground states usually originate from spin degeneracy, and hence, *only paramagnetic compounds exhibit C-term signals*.

At low temperatures, when kT is in the order of the Zeeman splitting in the presence of a strong magnetic field, a larger population of the lower energy compared to the higher energy Zeeman sublevels of the ground state results, according to the Boltzmann distribution. Hence, the intensities of the rcp and lcp transitions do not cancel anymore leading to an absorption band shape for the **C**-term. A further decrease of the temperature or an increase of the magnetic field results in an increase in the population of the lowest-energy sublevel and therefore, the **C**-term MCD intensity also increases. If the higher energy sublevels are completely depopulated, the **C**-term intensity reaches its maximum value, it saturates. Importantly, the temperature- and magnetic field-dependent **C**-term intensity (variable-temperature variable-field (VTVH) data) contains the complete information about the ground state properties including g values and zero-field splitting (ZFS) parameters, as well as the polarization of the respective electronic transition. All this information can be extracted by fitting these **C**-term saturation magnetization curves.

2.1. Fitting of variable-temperature variable-field (VTVH) MCD data

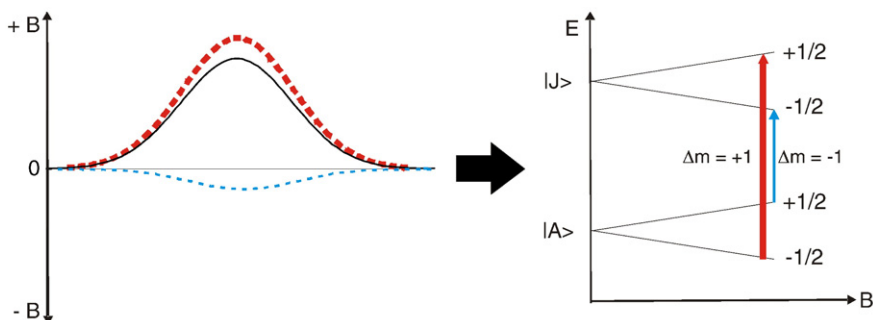
VTVH data obtained from the temperature- and field-dependent MCD **C**-term intensity can be fitted using the general method developed by Neese and Solomon [18]. The analysis is based on the following Eq. (2):

$$\frac{\Delta \epsilon}{E} = \frac{\gamma}{4 \cdot \pi \cdot S} \int_0^{\pi} \int_0^{2\pi} \sum_i N_i \left(l_x \langle S_x \rangle_i M_{yz}^{eff} + l_y \langle S_y \rangle_i M_{xz}^{eff} + l_z \langle S_z \rangle_i M_{xy}^{eff} \right) \sin(\theta) d\theta d\phi \quad (2)$$

where the sum over i runs over the sublevels of the ground state, $\Delta \epsilon/E$ is the MCD intensity, M^{eff} are the effective transition dipole moment products, l are the angles between the magnetic field axes and the molecular coordinate system, N_i are the Boltzmann populations, $\langle S \rangle_i$ are the spin-expectation values, γ is a constant, and S is the total spin. The individual polarizations of MCD bands can then be calculated using the M^{eff} values obtained from the fit of the VTVH saturation curves, using Eq. (3):

$$\%x = 100 \cdot \frac{\left(M_{xy}^{eff} \cdot M_{xz}^{eff} \right)^2}{\left(M_{xy}^{eff} \cdot M_{xz}^{eff} \right)^2 + \left(M_{xy}^{eff} \cdot M_{yz}^{eff} \right)^2 + \left(M_{xz}^{eff} \cdot M_{yz}^{eff} \right)^2} \quad (3)$$

The calculation of the %y- and %z-polarization is performed correspondingly. This methodology is applied in the following to analyze the low-temperature MCD data of metalloporphyrins. In order to



Scheme 1. MCD **C**-term transition between the magnetically split sublevels of ground state $|A\rangle$ and excited state $|J\rangle$ for an $S=1/2$ system.

determine the polarizations accurately, it is advantageous to obtain the g values and zero-field splitting parameters of the system independently, for example via SQUID and EPR measurements.

3. MCD spectroscopy of five-coordinate high-spin ferric hemes: identification of charge-transfer transitions between the axial ligand and iron(III)

3.1. Model complex studies on [Fe(TPP)(Cl)] (Ref. [21])

In order to test whether VTVH saturation curves for in-plane versus out-of-plane (with respect to the heme) polarized transitions are distinct enough to allow for clear and unambiguous assignments of the corresponding charge-transfer (CT) transitions, we first investigated the five-coordinate high-spin ferric model complex [Fe(TPP)(Cl)] (TPP²⁻ = tetraphenylporphyrinato dianion). Fig. 1, top shows the UV-vis absorption spectrum of this complex. As evident from this figure, and explicitly noted in the preceding literature [6,15,30], the optical spectra of high-spin ferric hemes are particularly complicated due to the half-filled d^5 shell of high-spin Fe(III), which allows for a multitude of ligand to metal CT transitions. Correspondingly, prior to our work, detailed assignments of the optical spectra of high-spin ferric hemes were lacking. In the case of [Fe(TPP)(Cl)], the most striking features are the intense, broad transition(s) around 379 nm to higher energy of the Soret band (which is at 417 nm), and the low-energy features around 650 nm, the nature of which was unknown prior to our work. In addition, the exact location

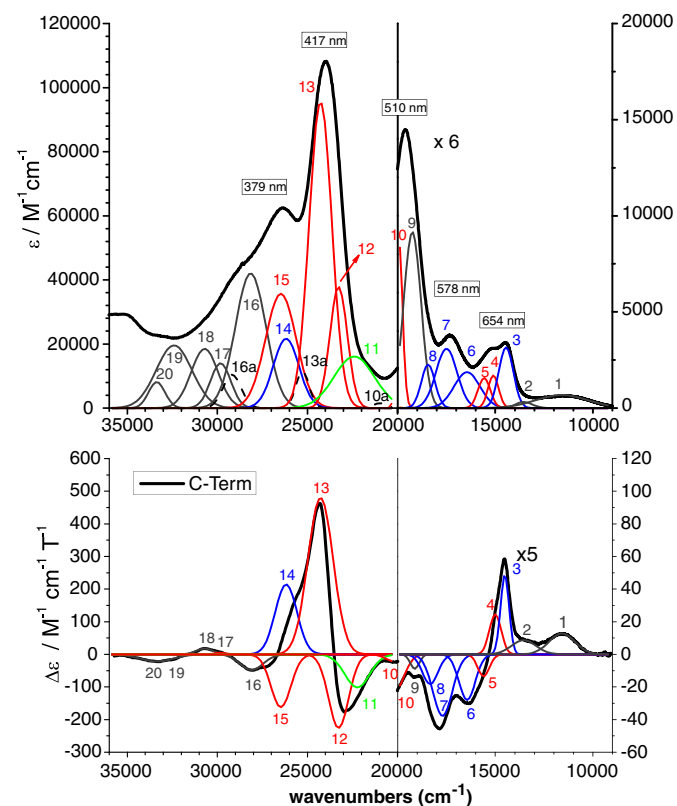


Fig. 1. Electronic spectra of [Fe(TPP)(Cl)]. Top: UV-vis absorption spectrum measured in CHCl_3 at room temperature. Bottom: MCD C-term spectrum measured in polystyrene at 5.8 K (lower concentration for 36 000–21 000 cm^{-1} region) and 5.6 K (higher concentration for 21 000–9 000 cm^{-1}), respectively. The colored lines represent a correlated Gaussian fit of these data, where the polarizations are color-coded (in-plane in red, out-of-plane in blue, mixed in green and not determined in gray). Reprinted with permission from Ref. [21]. Copyright 2008 American Chemical Society.

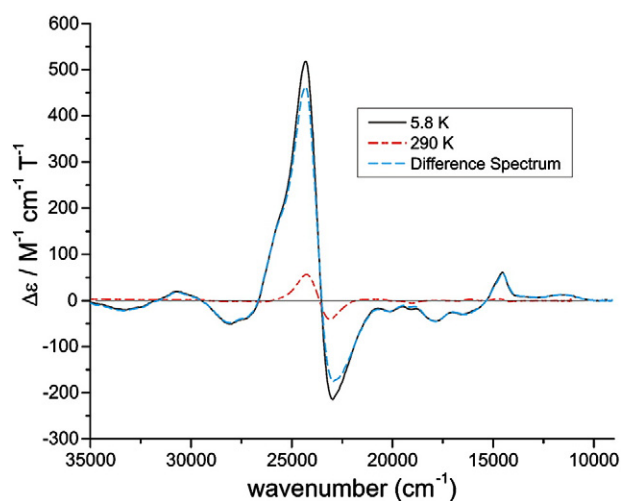


Fig. 2. MCD spectrum of [Fe(TPP)(Cl)]: The black line represents the MCD spectrum measured at 5.8 K, and the red (dashed) line shows the spectrum measured at 290 K (weak signal). The C-term spectrum in blue (dashed line) results from subtraction of the 290 K from the low-temperature data. Reprinted with permission from Ref. [21]. Copyright 2008 American Chemical Society.

of the Q and Q_v bands of the heme¹ [31] in the optical spectra of [Fe(TPP)(Cl)] was only ill defined [27]. To analyze and assign the electronic spectra of [Fe(TPP)(Cl)], the low-temperature MCD C-term spectra of this complex were recorded as shown in Fig. 1, bottom. A correlated fit of the UV-vis absorption and C-term data of this complex allowed for the identification of at least 20 electronic transitions as shown in Fig. 1. Here, the MCD C-term spectrum is calculated as the difference between the low-temperature and room temperature data, the latter being dominated by the temperature-independent A- and B-term signals as shown in Fig. 2.

In order to gain insight into the nature of the different transitions, VTVH MCD measurements were then performed on all features shown in Fig. 1. As described above, a detailed simulation of these data then provides insight into the polarizations of the different transitions, which greatly assists in the assignments. Fig. 3 shows that the polarizations of the bands, either in-plane (x,y) or out-of-plane (z) with respect to the heme plane, lead to distinct changes in the behavior of the magnetic saturation curves. In this way, out-of-plane polarized transitions between the iron(III) center and axial ligands can easily be identified. Based on this analysis, bands 3, 6–8, and 14 are shown to have major out-of-plane polarized contributions. With this information in hand, TD-DFT calculations can then be used to assign all experimentally observed features. These calculations by themselves are not accurate enough to assign the spectra, but they are insightful as they provide a list of important transitions and their relative energies and intensities, and in this way, define the “active space” of electronic transitions that are relevant. Taking these results into consideration, the lower-energy band 6 is assigned to the chloride(π)-to-iron(III) CT transition, whereas the higher energy transition (band 14) is assigned to a mixed chloride(σ/π)-to-iron(III) (Cl(σ/π) \rightarrow Fe) CT band. Further important features in the optical

¹ The optical spectra of all metalloporphyrins contain three strong signals that are of porphyrin character and that originate from the aromatic system of this macrocyclic ligand.[30] These are due to transitions between the occupied a_{1u} and a_{2u} π - and the unoccupied e_g π^* -orbitals of the heme. Here, the individual transitions couple via Cl mixing to create the intense Soret band at higher, and the weak Q band at lower energy. In addition, vibronic coupling between the Soret and Q state create the Q_v band, which occurs about 1300 cm^{-1} to higher energy from Q.

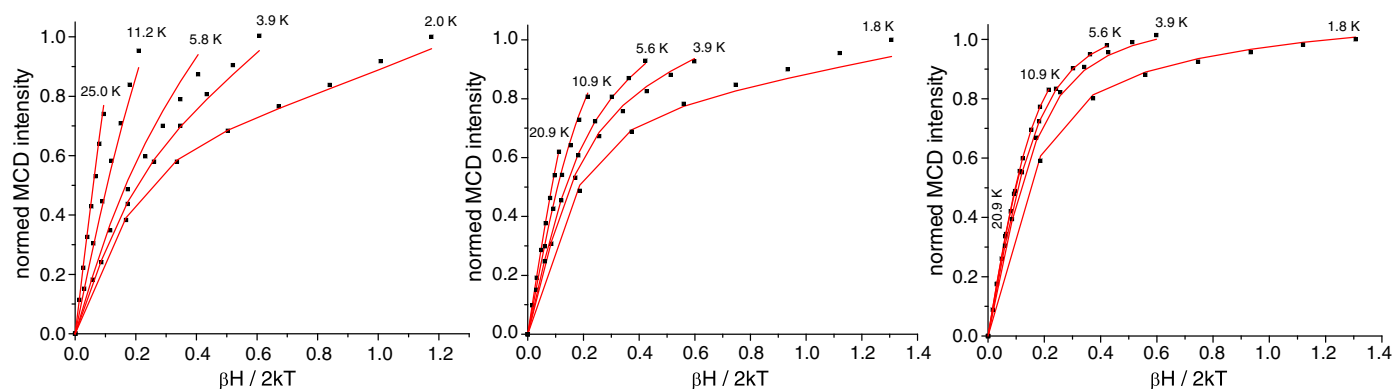
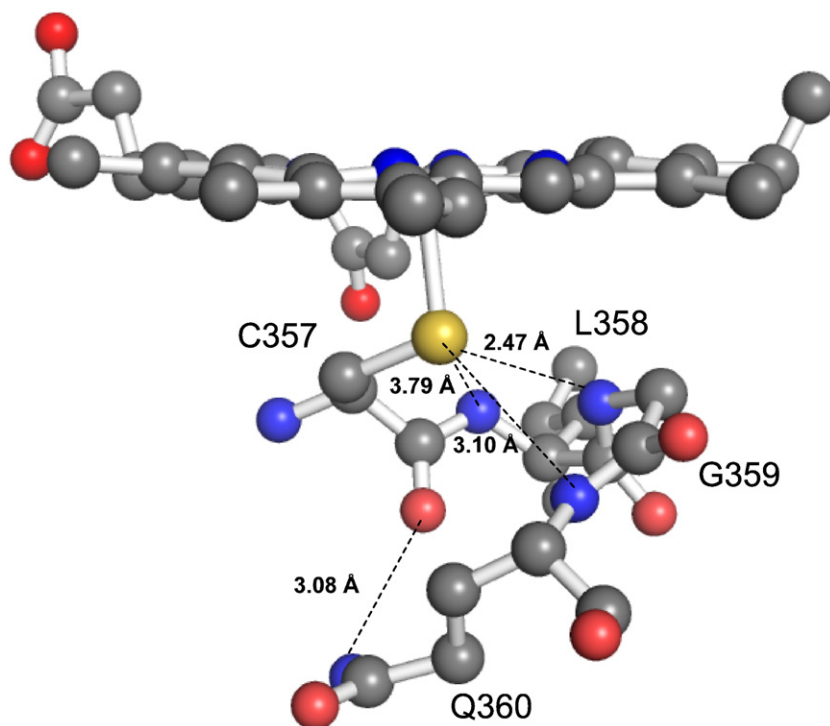


Fig. 3. MCD saturation magnetization curves (VT VH) of [Fe(TPP)(Cl)] for (a) band 12 (Soret) at 23266 cm^{-1} (left), (b) band 4 ($\text{CT}^{(1)}$) at 15000 cm^{-1} (middle), and (c) band 6 ($\text{CT}^{(1,m)}$) at 16444 cm^{-1} (right). Red lines: fit; black dots: experimental data points. Cases (a) and (b) correspond to x,y-polarized transitions whereas (c) shows a feature that is $\sim 75\%$ z polarized. Reprinted with permission from Ref. [21]. Copyright 2008 American Chemical Society.

spectra of [Fe(TPP)(Cl)] that are clarified based on our spectral analysis are as follows:

- Based on Gouterman's Four-Orbital model, it would be expected that the Soret band corresponds to a derivative-shaped pseudo **A**-term signal (see Chapter 4 below) [31]. However, Fig. 1 shows that this is not the case: for [Fe(TPP)(Cl)] several x,y-polarized MCD bands are observed in the Soret region. Our results show that the negative feature of the pseudo **A**-term signal of the Soret transition is in fact split into two components (bands 12 and 15) in [Fe(TPP)(Cl)] by selective mixing with an additional porphyrin $a_{2u} \rightarrow e_g(\text{LUMO})$ ($\pi \rightarrow \pi^*$) transition. The Soret band therefore corresponds to MCD bands 12, 13 and 15 in Fig. 1.
- Our results clarify the nature of the mysterious, broad absorption band at 379 nm in the UV-vis spectrum of [Fe(TPP)(Cl)]: this band originates from an additional porphyrin $\pi \rightarrow \pi^*$ transition, mixed with the Soret transition, and, importantly, the chloride(σ/π)-to-iron(III) CT transition.
- The Q band is very weak in [Fe(TPP)(Cl)], and cannot be observed as a distinct absorption or MCD feature. In comparison to rR spectroscopy [27], this feature likely occurs in the $18000\text{--}19000\text{ cm}^{-1}$ region. The vibronic band Q_v is identified at $\sim 20200\text{ cm}^{-1}$.
- Laser excitation into the low-energy absorption band at 654 nm leads to unusual Raman enhancement of low-energy anomalously polarized bands (where the depolarization ratio is $> 3/4$) [32], which correspond to in-plane and out-of-plane porphyrin deformation modes [27]. This absorption feature corresponds to MCD bands 3–5. Based on our analysis, bands 4 and 5 can be assigned to the two components of a porphyrin(π) $\rightarrow d_{\pi}$ CT transition ($d_{\pi} = d_{xz}, d_{yz}$) where electron



Scheme 2. Proximal hydrogen bonding network of Cytochrome P450_{cam}. The orange, yellow and blue balls represent the heme iron, the sulfur atom and the main chain amide nitrogen atoms of Leu358, Gly359, and Gln360, respectively. The dashed lines represent the $\text{NH}\cdots\text{S}$ hydrogen bonds in the Cys pocket. The image was generated using PyMOL from PDB code 2CPP [52]. Reprinted with permission from Ref. [33]. Copyright 2011 American Chemical Society.

density is shifted out of the heme plane, presumably inducing out-of-plane distortions of the heme in the excited states. This explains the resonance enhancement of out-of-plane heme vibrations in the Raman spectra of [Fe(TPP)(Cl)] upon excitation in this energy region.

In summary, we were able to develop an accurate theoretical description of the ground and excited states of [Fe(TPP)(Cl)] for the first time, and in particular, we demonstrated that VTVH magnetization curves can be used to identify iron \rightarrow axial ligand CT transitions in heme active sites. We then applied this methodology to high-spin ferric Cytochrome P450cam to investigate SCS effects in this protein.

3.2. Second coordination sphere effects in Cytochrome P450cam (Ref.[33])

Scheme 2 shows the active site of Cytochrome P450cam. In this case, a thiolate (Cys) group serves as the axial ligand to heme that is stabilized by four hydrogen bonds from protein backbone amide hydrogen atoms (the so-called ‘Cys’ pocket), provided by amino acids L358, G359, and Q360. Previous studies have shown that mutations of amino acids in this Cys pocket lead to distinct shifts in Fe(II)/Fe(III) redox potential [3], but the underlying causes for these shifts are not clear. We applied our MCD methodology described above to determine whether the heme–thiolate bond in the high-spin ferric case is in fact affected by these changes in the hydrogen bonding network. In order to do this, we first needed to identify the

thiolate \rightarrow iron(III) CT transitions, and then compare their energies in wild-type (wt) protein and the Cys pocket mutants. Note that Cyt. P450cam is in the ferric low-spin state in the resting form, but becomes high-spin upon substrate binding. This is the catalytically active state of the protein that is ready to accept an electron from an external source to start the catalytic cycle of the enzyme [34].

There are two potential problems in applying our MCD methodology to high-spin ferric Cyt. P450cam. First, the model complex [Fe(TPP)(Cl)] studied previously shows approximate 4-fold symmetry, and correspondingly, axial zero-field splitting (ZFS) where $E/D \sim 0$. Hence, in this case there is a clear distinction in magnetic response between in-plane and out-of-plane polarized transitions. In contrast, the Fe–S(Cys) bond in Cyt. P450cam is anisotropic in x and y direction (with z being the heme normal), leading to approximate 2-fold symmetry, and hence, rhombic ZFS with $E/D = 0.087$ [35]. It is therefore not clear a priori whether distinct changes in magnetic saturation curves between different types of electronic transitions can also be expected here. Fig. 4 shows theoretical magnetization curves calculated for different polarizations of electronic transitions. Based on these predictions, one would expect that z-polarization of electronic transitions should lead to VTVH curves that only show a small amount of nesting, and hence, that corresponding transitions can in fact be identified via VTVH measurements.

In addition, wt Cyt. P450cam with bound camphor is 100% high-spin at room temperature, but shows a fraction of the low-spin form at cryogenic temperatures due to the coordination of a water molecule to the heme, as evident from EPR spectroscopy [3]. In

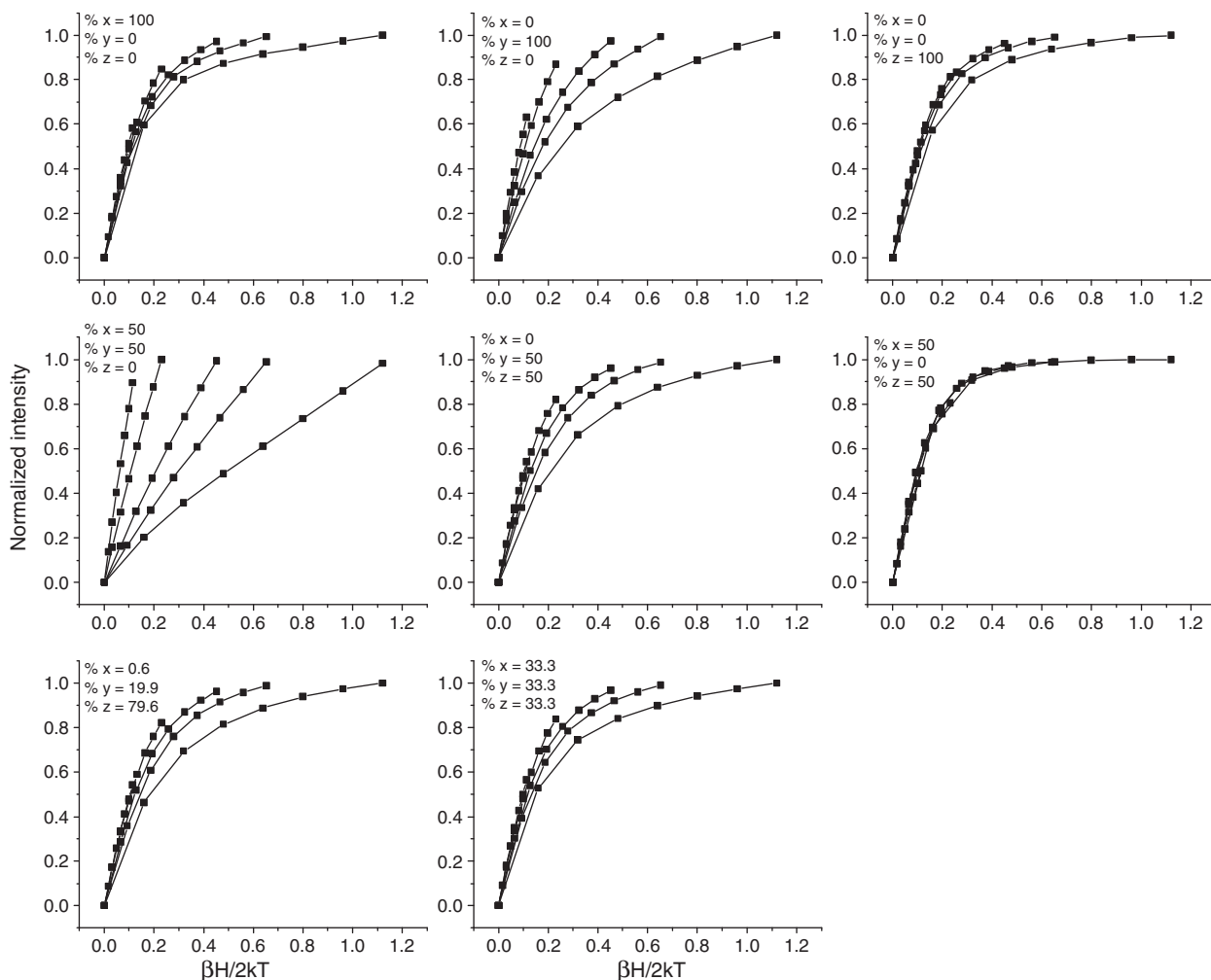


Fig. 4. Simulation of VTVH curves using $S = 5/2$, $E/D = 0.087$; $D = 3.8 \text{ cm}^{-1}$; and $g_x, g_y, g_z = 2.0023$. Reprinted with permission from Ref. [33]. Copyright 2011 American Chemical Society.

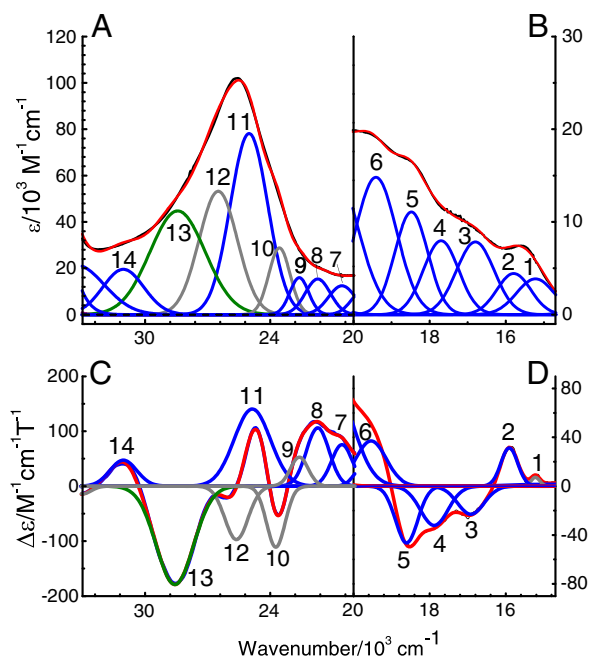


Fig. 5. Electronic spectra of ferric high-spin Q360P Cyt. P450cam in 50 mM potassium phosphate buffer (pH 7.4) with 500 μM *d*-camphor. Top: UV-vis absorption spectrum measured at room temperature. Bottom: MCD C-term spectrum measured at 5 K in phosphate buffer with 50% (v/v) glycerol added. The colored lines represent a correlated Gaussian fit of these data, where the predominant polarizations are color-coded (*xy*-polarizations in blue, *z*-polarizations in green, and undetermined polarizations in gray). The experimental spectra are shown in red. Reprinted with permission from Ref. [33]. Copyright 2011 American Chemical Society.

order to deconvolute the MCD spectra of wt Cyt. P450cam, we therefore investigated the variants Q360P and Y96W first, which had previously been shown to correspond to pure high-spin and low-spin complexes even at lq. helium temperatures. In this way, the signals of the high-spin and low-spin ferric heme center of Cyt. P450cam could be identified, and the MCD data of wt protein and other mutants that generate high-spin/low-spin mixtures at cryogenic temperatures could be deconvoluted.

Fig. 5 shows the UV-vis absorption and MCD spectra of high-spin ferric Q360P Cyt. P450cam, along with Gaussian fits of the obtained data. In total, 14 different electronic transitions are identified from these data. In order to gain further insight into the nature of these features, we then recorded VTVH saturation curves for the different MCD bands observed in Fig. 5. Fig. 6 shows that the predictions for the

saturation behavior shown in Fig. 4 are very well reproduced by the experimental data. Compared to [Fe(TPP)(Cl)], the electronic transitions appear generally more mixed with respect to their polarizations. Importantly, the VTVH data show that the intense MCD band 13 to higher energy of the Soret band is about 40% *z* polarized, as reflected by the very small nesting of the VTVH curves (see Fig. 6). TD-DFT calculations indicate that in the high-spin ferric Cyt. P450cam active site, the thiolate(π)-to-iron(III) CT transitions occur in the area of band 4, which shows some *z*-polarization, but that these transitions are distributed over a number of bands, and hence, are not as well defined as the chloride(π)-to-iron(III) CT transitions in [Fe(TPP)(Cl)]. Band 13 in the MCD spectra of high-spin ferric Cyt. P450cam is surprisingly intense, which strongly indicates that this feature is of CT character with a large amount of metal contribution. The distinct amount of *z*-polarization further points towards a strong contribution of thiolate to iron(III) CT character. The TD-DFT calculations predict a number of different CT transitions under the broad envelop of band 13, and, importantly, the presence of the thiolate(σ)-to-iron(III) CT transition. Based on the experimentally observed, strong *z*-polarization of this feature, we therefore assign band 13 at 28570 cm^{-1} to the $S(\sigma) \rightarrow \text{Fe}$ CT transition, similar to [Fe(TPP)(Cl)] where the corresponding $\text{Cl}(\sigma/\pi) \rightarrow \text{Fe}$ CT transition is observed at $\sim 26200\text{ cm}^{-1}$ as described above.

Fig. 7 shows the UV-vis absorption and low-temperature MCD data of the ferric low-spin Y96W Cyt. P450cam variant. The most striking differences between the MCD spectra of high-spin and low-spin Cyt. P450cam are (a) the absence of the intense $S(\sigma) \rightarrow \text{Fe}$ CT transition to higher energy of the Soret band in the low-spin form, and (b) the fact that the MCD C-term intensity of the Soret band is about 10 times larger for the low-spin ($-1696\text{ M}^{-1}\text{ cm}^{-1}\text{ T}^{-1}$) compared to the high-spin form ($+141\text{ M}^{-1}\text{ cm}^{-1}\text{ T}^{-1}$). The latter effect is due to differences in spin-orbit coupling (SOC), and, as we have shown in Ref. [21], constitutes a general distinction between the high-spin and low-spin forms of ferric hemes. This is further exemplified in Table 1, using other heme proteins as examples. Scheme 3 shows the two different mechanisms for C-term intensity [18], either based on SOC between two excited states (mechanism 1), or the ground state and a low-lying excited state (mechanism 2). Whereas mechanism 1 is valid for all iron(III) porphyrins, the low-spin state also has contributions from mechanism 2, because of the low-lying excited states generated from the $[t_{2(g)}]^5$ electron configuration that do not exist in the high-spin state. For low-spin ferric hemes with the “normal” ground state, $[d_{xy}]^2 [d_{xz}, d_{yz}]^3$ as indicated in Scheme 3, very strong SOC exists between the ground state and the first ligand-field excited state ($d_{xz} \rightarrow d_{yz}$ transition) corresponding to the reduced SOC matrix element $\langle d_{xz} | l_z | d_{yz} \rangle$. This leads to a

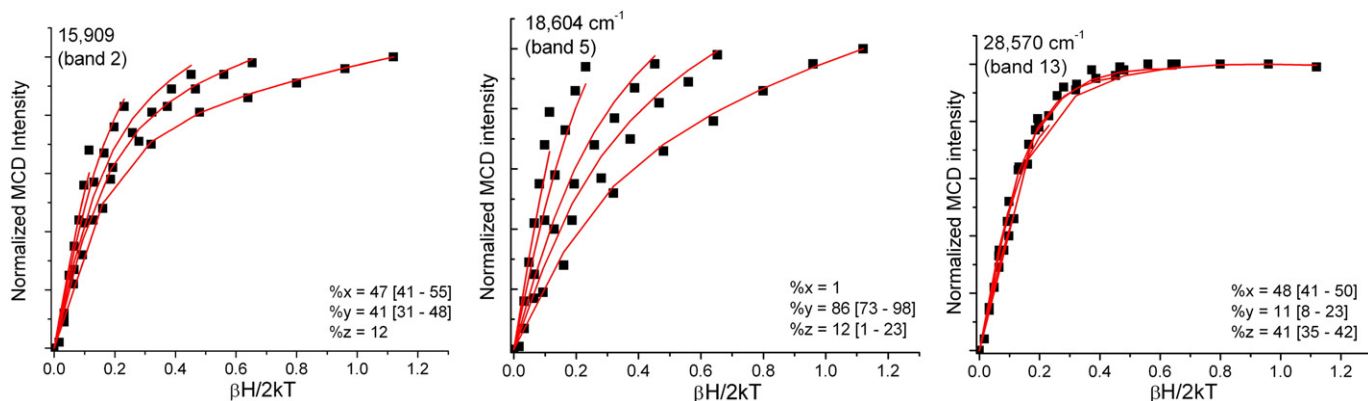


Fig. 6. Ferric high-spin Q360P Cyt. P450cam MCD C-term VTVH saturation magnetization curves for (a) band 2 at 15909 cm^{-1} (left, 88% *xy*-polarization), (b) band 5 at 18604 cm^{-1} (middle, 87% *xy*-polarization), and (c) band 13 at 28570 cm^{-1} (right, 41% *z*-polarization). Red lines: fit; black dots: experimental data points. Buffer conditions were the same as in Fig. 5. Reprinted with permission from Ref. [33]. Copyright 2011 American Chemical Society.

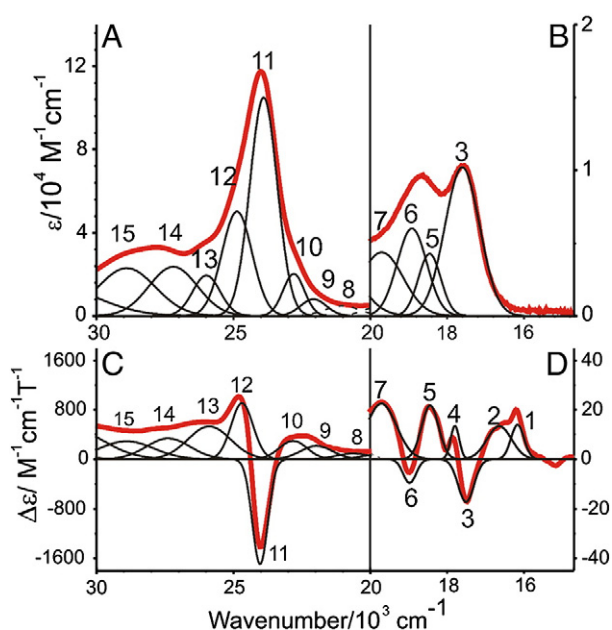


Fig. 7. Electronic spectra of ferric low-spin Y96W Cyt. P450cam taken under the same conditions as those in Fig. 5. Top: UV-vis absorption spectrum measured at room temperature. Bottom: MCD C-term spectrum measured at 5 K in phosphate buffer with 50% (v/v) glycerol added. Reprinted with permission from Ref. [33]. Copyright 2011 American Chemical Society.

dramatic increase in MCD intensity compared to the high-spin state. The fact that mechanism 2 is in fact responsible for this increase in MCD intensity of x,y polarized transitions is evident from MCD data of low-spin ferric hemes with the alternative “ d_{xy} ” ground state ($[d_{xz}, d_{yz}]^4 [d_{xy}]^1$) [25]. In this case, no SOC effective in z direction is present, and hence, mechanism 2 cannot contribute. Correspondingly, the MCD spectra obtained by Cheesman et al. for a complex with “ d_{xy} ” ground state show a dramatic decrease in MCD intensity compared to “normal” low-spin ferric hemes [22]. This difference in SOC is also indirectly reflected by the fact that low-spin Fe(III) shows large g shifts, whereas high-spin Fe(III) has practically no g shifts at all [24].

As mentioned above, the MCD spectrum of wt Cyt. P450cam at low-temperature shows signals from both the majority high-spin form and a minority low-spin component, which can now be deconvoluted based on the known spectra of the corresponding, pure spin states, shown in Figs. 5 and 7. In a typical MCD experiment, the estimated low-spin contribution for wt protein is about 15%. Importantly, the prominent $S(\sigma) \rightarrow Fe$ CT transition can easily be identified in the spectra of wt Cyt. P450cam and the additional Cys pocket mutant L358P as shown in Fig. 8. The energies of the $S(\sigma) \rightarrow Fe$ CT bands observed at 28724, 28620, and 28570 cm^{-1} for wt, L358P, and Q360P Cyt P450cam, respectively (Fig. 8), have implications for the effect of H-bonding on the Fe–S bond. In going from wt to L358P and

Table 1

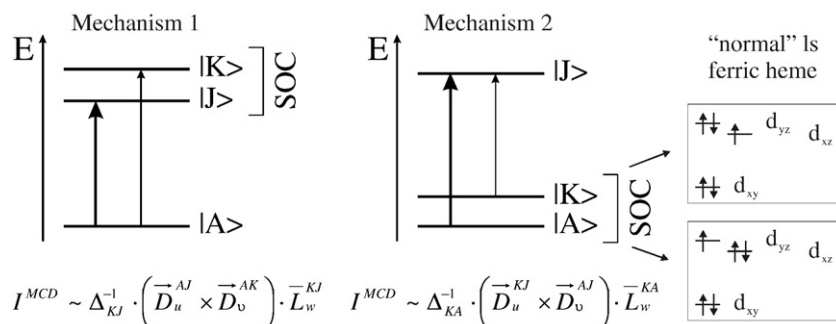
Peak-to-trough (maximum-to-minimum) saturation limits for the Soret bands of [Fe(TPP)(Cl)] and different (ferric) enzymes.

Compound	Spin-state	Peak-to-trough saturation limit ^a	Ref.
[Fe(TPP)(Cl)]	5/2	$3.4 \cdot 10^3$	[21]
Horse heart cytochrome c	1/2	$40.5 \cdot 10^3$	[53]
Metmyoglobin CN ⁻	1/2	$60.5 \cdot 10^3$	[53]
Cytochrome c oxidase	1/2	$25 \cdot 10^3$	[54]
Cytochrome c oxidase CN ⁻	1/2	$54 \cdot 10^3$	[54]
Ferryl horseradish peroxidase (HRP) compound I	3/2	$1.9 \cdot 10^3$	[55]

^a Peak-to-trough saturation limits are given in $M^{-1} cm^{-1}$.

Q360P, one hydrogen bond to sulfur is removed. In addition, Q360P is also lacking an additional hydrogen bond to the cysteine backbone. The removal of hydrogen bond(s) from the thiolate group of cysteine increases the electron density on sulfur, and thus, the sulfur donor strength. This, in turn, affects the strength of the Fe–S bond. DFT calculations on six-coordinate ferric nitrosyl model complexes [Fe(P)(SR)(NO)] (P^{2-} = porphine²⁻; the simplest porphyrin ligand) support this idea, and show a correlated increase in the Fe–S force constant and a decrease in Fe–S bond distance upon stepwise removal of strong NH-S(thiolate) hydrogen bonds in model complexes [36]. DFT calculations indicate that the reason for this is an increase of $S(p_z)$ in energy as H-bonds are removed, leading to an increase of the Fe–S covalency, and hence, bond strength. There is little doubt that L358, G359, and Q360 form amide hydrogen bonds to the sulfur donor atom of C357 in Cyt P450cam; the real question is how strong these interactions are, and how strongly they influence the Fe–S bond strength. One way to detect this change is by probing the energy of the $S \rightarrow Fe$ CT transition: as the $S(p_z)$ orbital increases in energy, the energetic separation between the corresponding bonding and antibonding combinations of $S(p_z)$ and d_{z^2} of iron(III) decreases and this shifts the corresponding $S(\sigma) \rightarrow Fe$ CT transition to lower energy. This notion is consistent with the trend observed in going from wt to L358P and to Q360P. However, this effect is quite small. This is in agreement with the small changes in Fe–S vibrational frequencies observed between wt, L358P and Q360P from Raman spectroscopy [3]. One could argue that the small changes are due to (a) rearrangement of the Cys pocket to strengthen the remaining H-bonds, or (b) incorporation of water in the Cys pocket in the mutants. However, the crystal structure of ferrous L358P indicates that this is likely not the case [37].

Based on the *small* changes in the $S(\sigma) \rightarrow Fe$ CT transition energy between wt, L358P, and Q360P, and corresponding *small* changes in $\nu(Fe-S)$ along this series, our work therefore implies that the hydrogen bonds between the axial thiolate (C357) ligand and L358 and Q360 are weak. The remaining H-bond from G359 could be stronger, and could be most significant for fine-tuning the Fe–S bond strength. This is in accordance with X-ray crystallography, which shows that



Scheme 3. Different mechanisms for MCD C-term intensity. Right: example for mechanism 2.

the C357–G359 contact is in fact the shortest. This point requires further study. Based on these findings, we propose that the roles of the hydrogen bonds from L358 and Q360 are *not* primarily for fine-tuning the sulfur donor strength of the proximal Cys, but for the protection of the thiolate ligand against protonation or reaction with diatomics, all of which would lead to Cyt. P420 formation. In addition, these hydrogen bonds position the cysteinate for proper coordination to the iron center. Importantly, the idea that the L358 and Q360 hydrogen bonds to the axial cysteinate ligand are weak correlates with function in Cyt. P450 enzymes: weak H-bonds, leading to a strong Fe–S bond, are in fact of key importance for efficient O–O bond cleavage and compound I formation, according to the push effect [38]. This finding disagrees with several hypotheses that the NH–S hydrogen bonds *generally* control the Fe–S bond strength/interaction, and in this way, the redox potential of the heme [39,40]. Based on these results, the observed changes in redox potential between wt and the Cys pocket mutants then likely relate to a stabilization of the ferrous form of the protein or a change in its ground state (see below) as a major source for the observed changes, and/or to structural changes in the heme conformation in the mutants. These aspects are currently under investigation.

4. MCD spectroscopy of high-spin ferrous hemes: second coordination sphere effects control the ground state of heme (Ref. [23])

A common feature in many heme proteins is the presence of hydrogen bonds from the proximal histidine ligand to nearby protein side chains. The strength of these hydrogen bonds is thought to vary from very weak $\{(\text{His})\text{N}-\text{H}\cdots\text{Acceptor}\}$ proton donation to complete donation to form the corresponding imidazolate ligand [41–47]. The idea that a strong hydrogen bond has a strong influence on heme protein behavior is longstanding but has been difficult to investigate in a systematic manner. Clearly, there are significant differences in the strengths of the hydrogen bonds formed to the proximal histidine ligand in different heme proteins. Three distinctly different scenarios can be identified from the literature: (a) the globins and a number of other proteins form weak hydrogen bonds between histidine and a nearby carbonyl or alcohol group (weak), (b) the peroxidases where the proximal histidine is hydrogen-bonded to conserved aspartate residues (medium/strong), and (c) the oxidases where hydrogen bonding involves conserved glutamates (medium/strong). In particular, the idea continues to appeal that the proximal histidine in the peroxidases has imidazolate-like character. This strong hydrogen bond is thought to stabilize higher oxidation states

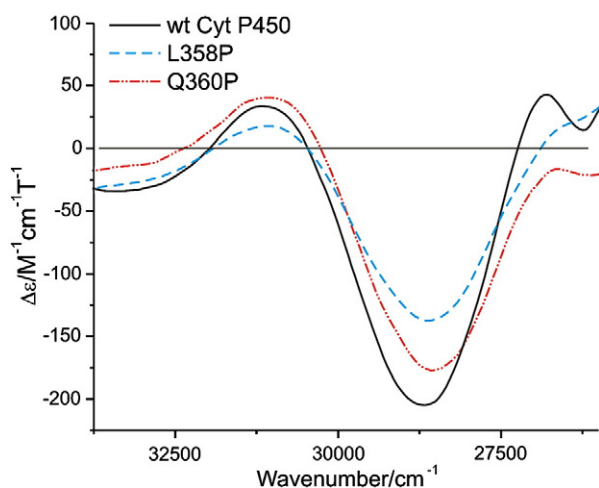


Fig. 8. MCD C-term spectra of wt Cyt P450cam, L358P, and Q360P taken under the same conditions as those in Fig. 5. These spectra focus on the S → Fe CT transition for each enzyme.

of iron and to distinctly alter the chemical behavior of the peroxidases relative to the globins. Nevertheless, the role of this hydrogen bond is still one of the unresolved issues concerning these enzymes. In order to shed light on this question, we used MCD spectroscopy coupled to DFT calculations to elucidate the electronic structures of five-coordinate high-spin ferrous hemes with either axial imidazole or imidazolate coordination, corresponding to the extremes with either no hydrogen bonding, or complete abstraction of the imidazole proton (strongest possible hydrogen bond leading to deprotonation). In order to achieve an exact comparison of these two borderline cases, we chose to study the corresponding model complexes $[\text{Fe}(\text{TPP})(2\text{-MeHIm})]$ and $[\text{K}(222)][\text{Fe}(\text{TPP})(2\text{-MeIm}^-)]$, where (222) = Kryptofix 222 (4,7,13,16,21,24-hexaoxa-1,10-diazabicyclo [8.8.8]-hexacosane), and 2-MeHIm = 2-methylimidazole. Finally, we also included the model complex $[\text{Na}(222)][\text{Fe}(\text{TPP})(\text{Cl})]$ in the study where the bound Cl^- ligand is a crude model for the proximal thiolate in Cyt. P450s [23].

The low-temperature MCD spectra obtained for $[\text{Fe}(\text{TPP})(2\text{-MeHIm})]$, $[\text{K}(222)][\text{Fe}(\text{TPP})(2\text{-MeIm}^-)]$, and $[\text{Na}(222)][\text{Fe}(\text{TPP})(\text{Cl})]$ are overall very similar and are dominated by the $\pi \rightarrow \pi^*$ transitions of the porphyrin ligand. Fig. 9 shows the data for $[\text{Fe}(\text{TPP})(2\text{-MeIm}^-)]^-$ as a representative example. The spectra show four relatively intense MCD features in the region of the Q and Q_V bands, with alternating negative and positive intensities, and a corresponding pair of bands for the Soret transition. As shown by us previously (see also above), the Soret, Q, and Q_V bands of simple metalloporphyrins should give rise to a derivative-shaped C-term signal at

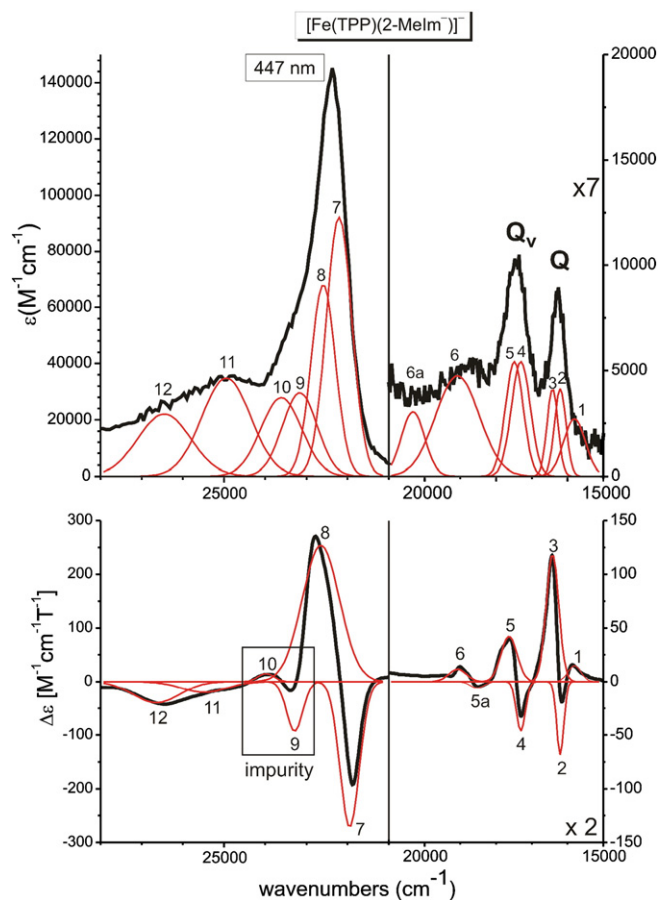


Fig. 9. Electronic spectra of $[\text{Fe}(\text{TPP})(2\text{-MeIm})^-]$. Top: UV-vis absorption spectrum (bold line) measured in CH_2Cl_2 at room temperature. Bottom: MCD C-Term spectrum (bold line) measured in toluene/ CH_2Cl_2 (1:1) at 2 K. The red (thin) lines represent a correlated fit of these data.

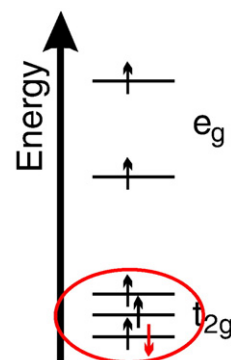
low-temperature in MCD, due to a low-symmetry splitting of the porphyrin $e_g(\pi^*)$ LUMO in the complexes [31,48]. This causes the Soret, Q, and Q_v excited states, which have E_u symmetry in D_{4h} , to split into two components, and correspondingly, two bands are observed for the Soret, Q, and Q_v transitions in MCD. Importantly, due to excited state spin-orbit coupling, the two components of these features show opposite signs, and hence, the Soret, Q, and Q_v transitions each give rise to a derivative-shaped ‘pseudo-A’ C-term signal in MCD at low (lq. helium) temperature. Additionally, since Q_v is the vibronic band of Q, it should appear about 1250 cm^{-1} to higher energy of Q as determined by Gouterman [30]. With this in mind, the electronic spectra of the ferrous heme-imidazole/ate complexes can be readily understood. For $[\text{Fe}(\text{TPP})(2\text{-MeIm}^-)]^-$, bands 2 and 3 (see Fig. 9) at 16206 and 16432 cm^{-1} , respectively, belong to the Q transition, followed by Q_v , at 17308 and 17640 cm^{-1} , respectively (bands 4 and 5). The energy differences between the corresponding negative features 2 and 4 and positive features 3 and 5 are 1102 and 1208 cm^{-1} , which is in good agreement with the predicted value of $\sim 1250\text{ cm}^{-1}$ mentioned above. To higher energy, bands 7 and 8 at 21950 and 22650 cm^{-1} , respectively, constitute the two components of the Soret transition. Note that bands 9 and 10 likely belong to a ferric impurity due to the great sensitivity of $[\text{Fe}(\text{TPP})(2\text{-MeIm}^-)]^-$ towards trace amounts of O_2 , as evidenced by the comparison of the MCD spectra of different preparations of this complex.

In summary, our data show that the MCD C-term spectra of $[\text{Fe}(\text{TPP})(2\text{-MeHIm})]$, $[\text{K}(222)][\text{Fe}(\text{TPP})(2\text{-MeIm}^-)]$, and $[\text{Na}(222)][\text{Fe}(\text{TPP})(\text{Cl})]^-$ are all very similar with respect to the observed electronic transitions. However, there is one striking difference between these data: the absolute MCD intensities. As shown in Table 2, the absolute MCD intensity of the complex with the *neutral* imidazole ligand (Class N) is about 1 order of magnitude larger compared to the complexes with the *anionic* imidazolate and chloride ligands (Class A). In addition, these two different classes also show distinctive differences with respect to their Moessbauer- and EPR-spectroscopic and structural properties as described in Ref. [23]. All these data indicate that these complexes differ in their electronic ground states.

We further investigated this aspect using DFT calculations. In the ground state of five-coordinate high-spin ferrous hemes, all five d-orbitals of iron are singly occupied (five α (spin-up) electrons), and therefore, differences in the ground states of these complexes relate to the location of the additional, sixth β (spin-down) electron as shown in red in Scheme 4. Importantly, our DFT calculations show that in the imidazole complex, this orbital has 65% d_{xz} character, where z is the heme normal, and the xz plane contains the imidazole ligand. An iso-density surface plot of this MO is shown in Fig. 10, left. In contrast, in the imidazolate complex, the sixth (spin-down) electron occupies an orbital that has 50% d_{xy} and only 15% d_{xz} character, as shown in Fig. 10, right. This orbital is therefore effectively located in the heme plane. The chloride complex shows a similar ground state. In summary, these results show that in the imidazolate and chloride (Class A) complexes the doubly occupied d-orbital is located in the porphyrin plane, whereas it is orthogonal to the heme plane in the imidazole (Class N) complex. This difference in ground states is illustrated in Scheme 5. Moreover, the MCD intensity directly reflects this change in ground state, and, as we will show in the following, directly correlates with the amount of d_π character ($d_\pi = d_{xz}$ or d_{yz}) in the occupied β -spin d-orbital of iron (see Table 2).

Table 2
Absolute MCD intensities of the Soret bands in high-spin ferrous heme model complexes (numbers are rounded). Data were obtained at $\sim 2\text{ K}$ in all cases.

	Intensity [$\text{M}^{-1}\text{ cm}^{-1}\text{ T}^{-1}$]
$[\text{Fe}(\text{TPP})(2\text{-MeHIm})]$	5000
$[\text{Fe}(\text{TPP})(2\text{-MeIm})]^-$	300
$[\text{Fe}(\text{TPP})(\text{Cl})]^-$	800



Scheme 4. Differences in the electronic ground state of high-spin ferrous hemes relate to the exact location of the ‘extra’ (spin-down) electron, shown in red (in oval).

In general, MCD C-term intensity has contributions from two different mechanisms as described above and illustrated in Scheme 3 for the low-spin ferric case, and relates to SOC between two energetically close excited states (mechanism 1), or the ground state and a low-lying excited state (mechanism 2) [18,21]. Whereas mechanism 1 applies to all metalloporphyrins due to the lifted degeneracy of the $e_g(\pi^*)$ LUMO of the heme macrocycle in actual complexes, mechanism 2 often originates from low-lying ligand-field excited states. In the case of the five-coordinate high-spin ferrous heme complexes considered here, these low-lying excited states would originate from transitions of the single β -spin d-electron between different t_{2g} -type d-orbitals of iron (see Scheme 4). Since the Q, Q_v and Soret transitions are in-plane (xy) polarized, SOC has to be effective in z direction in order to generate significant C-term intensity according to mechanism 2. Using the mathematical expression for C-term intensity from Ref. [18] (see Scheme 3, middle), we were able to show that the reduced SOC matrix element between the ground state $|A\rangle$ and the ligand-field excited state $|K\rangle$ becomes [23]:

$$\bar{L}_z^{KA} = \text{Im}\langle K|H_{\text{SOC}}^z|A\rangle = \frac{\text{Im}\left[\zeta^{\text{Fe}} \sum_{r,s} \langle c_s^d \phi_s^d | L_z | c_r^d \phi_r^d \rangle\right]}{\Delta_{KA}} = \frac{\text{Im}\left[\zeta^{\text{Fe}} \langle \sum_s c_s^d \phi_s^d | L_z | c_{xz}^\beta d_{xz}^\beta \rangle\right]}{\Delta_{KA}} \quad (4)$$

Here we use the coordinate system from our DFT results shown in Fig. 10, where the d_π contribution to the occupied β -spin t_{2g} -type d-orbital in the ground state $|A\rangle$ is of d_{xz} character (with the corresponding MO coefficient c_{xz}^β). The sum $\sum_s c_s^d \phi_s^d$ corresponds to the LCAO expansion of the β -spin t_{2g} -type d-orbital in the relevant excited

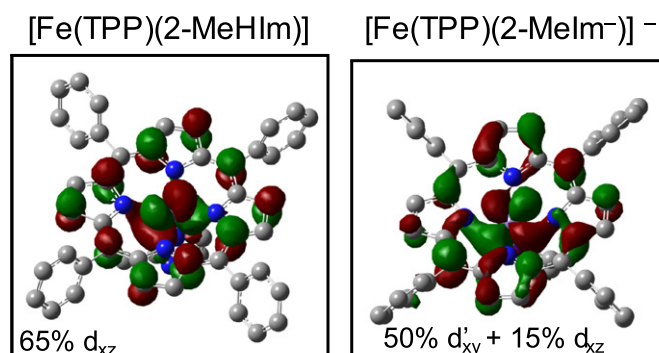
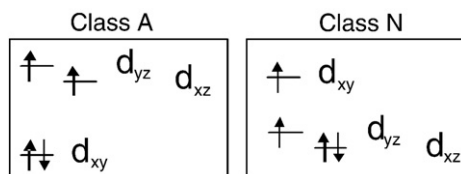


Fig. 10. Occupied β -spin d-orbitals in the ground states of high-spin ferrous heme-imidazole (Class N, left) and -imidazolate (Class A, right) complexes; see Scheme 5.



Scheme 5. Differences in the electronic ground states of high-spin ferrous hemes of Class A (anionic axial ligand) and Class N (neutral axial ligand) type; see text.

state $|K\rangle$. Importantly, the I_z operator (representing SOC in z direction) only connects the orbitals d_{xz} and d_{yz} , such that:

$$\text{Im}\langle d_{yz} | I_z | d_{xz} \rangle = 1, \text{ whereas}$$

$$\text{Im}\langle d_{xz} | I_z | d_{xy} \rangle = 0 \text{ and } \text{Im}\langle d_{yz} | I_z | d_{xy} \rangle = 0.$$

This means that d_{xy} cannot contribute directly to MCD intensity for x,y polarized transitions. Hence, in the imidazolate (Class A) complex, only the d_{xz} character mixed into the occupied β -spin d_{xy} orbital in the ground state is able to generate C-term intensity, as indicated in Eq. (4). Because of this, mechanism 2 can only contribute significantly to the MCD intensity of the Q, Q_v , and Soret transitions for Class N systems, whereas this contribution will be much smaller for Class A. Based on the coefficients of the occupied β -spin t_{2g} -type d-orbitals of the imidazole and imidazolate complexes (see Fig. 10), and the excitation energies calculated from TD-DFT, we estimate that the MCD C-term intensity for [Fe(TPP)(2-MeHIm)] is approximately 7 times larger than that of [K(222)][Fe(TPP)(2-MeIm⁻)], which is in good agreement with experiment (see Table 2) [23]. In this sense, the absolute MCD C-term intensity of five-coordinate high-spin ferrous hemes directly reflects the amount of d_{π} character in the singly occupied β -spin (minority spin) d-orbital in the ground state.

In summary, variation of the hydrogen bonding network of the proximal His ligand can change the ground state of five-coordinate high-spin ferrous heme active sites. We believe that this change in ground state in fact contributes to function in heme proteins. This is seen in the proteins that can definitely be assigned to one of the two classes. Deoxyhemoglobin and -myoglobin, members of Class N, are reversible dioxygen binders, where the formed O_2 complex has partial superoxide character. Here, the location of the single β d-electron in a t_{2g} orbital orthogonal to the heme plane that overlaps with the π^* orbitals of the incoming O_2 molecule is certainly advantageous for dioxygen binding by lowering kinetic barriers for electron transfer. In addition, imidazole is a weaker ligand than imidazolate, which contributes to the stabilization of the iron- O_2 complex by lowering the σ -trans interaction between the bound imidazole and O_2 ligands. In this way, the hydrogen bond to imidazole could also be used to fine-tune the strength of the Fe- O_2 bond (cf. corresponding Fe(II)-NO complexes [48–51]). On the other hand, horseradish peroxidase and Cyt. P450s, members of Class A, are involved in peroxide/dioxygen activation. Here, the potential link to function is that a more strongly donating proximal ligand will promote heterolytic O–O bond cleavage, and hence, compound I formation. This, on the other hand, has to be avoided in hemoglobin and myoglobin, which is in agreement with the weaker imidazole ligand in this case. Finally, by adjusting the hydrogen bond to histidine, and hence, the donor strength of this ligand and the ground state of the high-spin ferrous heme, the Fe(II)/Fe(III) redox potential of the heme could also potentially be fine-tuned.

5. Conclusions

In conclusion, this review demonstrates how low-temperature MCD spectroscopy can be used to obtain detailed insight into the spectral assignments and electronic structures of ferrous and ferric heme complexes. In this way, the consequence of SCS effects, in

particular hydrogen bonding, on the electronic structures of hemes can be probed. In the case of high-spin ferric hemes, a large number of charge-transfer (CT) transitions are observed in the optical spectra of the complexes, and in particular, low-temperature MCD spectroscopy is a powerful method to resolve these transitions due to the fact that MCD intensity is a signed quantity. In addition, we have demonstrated that the magnetic saturation behavior of the MCD signals can be used to identify out-of-plane polarized (relative to heme) CT transitions; i.e. transitions between the axial ligand and the iron(III) center. We applied this methodology to the model complex [Fe(TPP)(Cl)] and Cytochrome P450cam, and in both cases, we identified the corresponding Cl \rightarrow Fe(III) and S \rightarrow Fe(III) CT transitions, respectively. In particular, the corresponding σ -type CT transitions are observed in both cases as intense MCD signals to higher energy of the Soret band of heme. These transitions can therefore be used as a sensitive marker of the electronic structure of the axial Fe(III)-X unit. In comparison, the S(σ) \rightarrow Fe(III) CT transition is observed at 28724, 28620, and 28570 cm^{-1} for wt, L358P, and Q360P Cyt P450cam, respectively. In the latter mutants, the hydrogen bonding network to the axial Cys ligand has been altered. Importantly, the small shift of the S(σ) \rightarrow Fe(III) CT transitions in the mutants compared to wt indicates that the hydrogen bonds only have a minor effect on the properties of the Fe–S bond, and hence, are more important for a stabilization of the thiolate against protonation or reaction with diatomics compared to a fine-tuning of the Fe–S bond. This result is further supported by resonance Raman spectroscopy.

In the case of five-coordinate high-spin ferrous heme-imidazole protein active sites, it has been noticed that hydrogen bonding to the proximal His varies within a wide range of hydrogen bond strengths. In order to investigate the significance of this finding, we performed low-temperature MCD measurements on corresponding five-coordinate high-spin ferrous-imidazole (no hydrogen bond) and -imidazolate (complete abstraction of the proton by strong acceptor) model complexes, and also compared these results to a corresponding ferrous-chloride complex as a simple model for Cyt. P450s. The obtained low-temperature MCD spectra of these high-spin ferrous complexes are rather simple, and are dominated by the Q, Q_v , and Soret ($\pi \rightarrow \pi^*$) transitions of the porphyrin macrocycle. However, the obtained absolute MCD intensities show distinct differences between these compounds. For the imidazole complex (Class N), an approximately 10 times larger MCD intensity is observed compared to the complexes with anionic ligands like imidazolate and chloride (Class A). Further data analysis in correlation to DFT calculations shows that this difference relates to a change in the ground state of the complexes: in the case of Class N compounds, the single β -spin electron of high-spin iron(II) occupies a d_{π} -type orbital, d_{xz} in the coordinate system used here, which is orthogonal to the heme plane (see Scheme 5). This allows for efficient spin-orbit coupling of the ground state to the low-lying d_{yz} (ligand-field) excited state (β - $d_{xz} \rightarrow \beta$ - d_{yz} excitation), which generates additional MCD C-term intensity through mechanism 2 in Scheme 3. As the hydrogen bond to the proximal imidazole increases in strength, the d_{xz} orbital that carries the single β -spin electron in the ground state rotates towards the plane of the heme, which is achieved by an increasing admixture of d_{xy} character. However, this increasing admixture of d_{xy} character quenches the additional MCD C-term intensity generated through mechanism 2. In the extreme of the imidazolate complex, i.e. the case where the proton has been completely abstracted by a strong acceptor (deprotonation), the orbital that carries the single β -spin electron has essentially transformed in an almost pure d_{xy} orbital (located in the heme plane), leading to a drop in total C-term MCD intensity by a factor of ~ 10 compared to the imidazole complex. In this way, the variation of the hydrogen bonding network of the proximal His ligand changes the ground state of the five-coordinate high-spin ferrous heme active site, and this can directly be monitored via MCD spectroscopy (C-term intensity).

Abbreviations

CT	charge-transfer
DFT	density functional theory
EPR	electron paramagnetic resonance
Hb	hemoglobin
HOMO	highest occupied molecular orbital
LUMO	lowest unoccupied molecular orbital
Mb	myoglobin
MCD	magnetic circular dichroism
P ²⁻	porphine ²⁻ , the simplest porphyrin ligand
rR	resonance Raman
SCS	second coordination sphere
SOC	spin-orbit coupling
SQUID	superconducting quantum interference device
TD	time-dependent
VTVH	variable-temperature variable-field
wt	wild-type
ZFS	zero-field splitting

Acknowledgement

This work was supported by the National Science Foundation (CHE 0846235).

References

- [1] R.H. Holm, P. Kennepohl, E.I. Solomon, *Chem. Rev.* 96 (1996) 2239–2314.
- [2] R.E. Dickerson, I. Geis, *Hemoglobin: Structure, Function, Evolution, and Pathology*, Benjamin-Cummings, Menlo Park, CA, 1983.
- [3] S. Yoshioka, T. Tosha, S. Takahashi, K. Ishimori, H. Hori, I. Morishima, *J. Am. Chem. Soc.* 124 (2002) 14571–14579.
- [4] A. Dey, T. Okamura, N. Ueyama, B. Hedman, K.O. Hodgson, E.I. Solomon, *J. Am. Chem. Soc.* 127 (2005) 12046–12053.
- [5] L.V. Michel, T. Ye, S.E.J. Bowman, B.D. Levin, M.A. Hahn, B.S. Russell, S.J. Elliott, K.L. Bren, *Biochemistry* 46 (2007) 11753–11760.
- [6] M.R. Cheesman, C. Greenwood, A.J. Thomson, *Adv. Inorg. Chem.* 36 (1991) 201–255.
- [7] J. Cheek, J.H. Dawson, *The Porphyrin Handbook*, Vol. 7, in: K.M. Kadish, K.M. Smith, R. Guilard (Eds.), Academic Press, New York, 2000, pp. 339–369.
- [8] J. Mack, M.J. Stillman, N. Kobayashi, *Coord. Chem. Rev.* 251 (2007) 429–453.
- [9] N. Kobayashi, N. Katsunori, *Chem. Commun.* (2007) 4077–4092.
- [10] J. Mack, Y. Asano, N. Kobayashi, M.J. Stillman, *J. Am. Chem. Soc.* 127 (2005) 17697–17711.
- [11] P.M.A. Gadsby, A.J. Thompson, *J. Am. Chem. Soc.* 112 (1990) 5003–5011.
- [12] J. Rawlings, P.J. Stephens, M.D. Kamen, *Biochemistry* 16 (1977) 1725–1729.
- [13] P.J. Stephens, *Adv. Chem. Phys.* 35 (1976) 197–264.
- [14] J.H. Dawson, M. Sono, *Chem. Rev.* 87 (1987) 1255–1276.
- [15] W.R. Browett, A.F. Fucaloro, T.V. Morgan, P.J. Stephens, *J. Am. Chem. Soc.* 105 (1983) 1868–1872.
- [16] P.J. Stephens, *Annu. Rev. Phys. Chem.* 25 (1974) 201–232.
- [17] E.I. Solomon, E.G. Pavel, K.E. Loeb, C. Campochiaro, *Coord. Chem. Rev.* 144 (1995) 369–460.
- [18] F. Neese, E.I. Solomon, *Inorg. Chem.* 38 (1999) 1847–1865.
- [19] V.S. Oganesyan, S.J. George, M.R. Cheesman, A.J. Thomson, *J. Chem. Phys.* 110 (1999) 762–777.
- [20] N. Lehnert, S. DeBeer George, E.I. Solomon, *Curr. Opin. Chem. Biol.* 5 (2001) 176–187.
- [21] F. Paulat, N. Lehnert, *Inorg. Chem.* 47 (2008) 4963–4976.
- [22] M.R. Cheesman, F.A. Walker, *J. Am. Chem. Soc.* 118 (1996) 7373–7380.
- [23] C. Hu, C.D. Sulok, F. Paulat, N. Lehnert, A.I. Zatsman, M.P. Hendrich, C.E. Schulz, W.R. Scheidt, *J. Am. Chem. Soc.* 132 (2010) 3737–3750.
- [24] F.A. Walker, *Coord. Chem. Rev.* 185 (1999) 471–534.
- [25] F.A. Walker, *Chem. Rev.* 104 (2004) 589–616.
- [26] T.G. Spiro, *Iron Porphyrins (Part Two)*, in: A.B.P. Lever, H.B. Gray (Eds.), Addison-Wesley Publishing Company, Reading, MA, 1983, pp. 89–159.
- [27] F. Paulat, V.K.K. Praneeth, C. Näther, N. Lehnert, *Inorg. Chem.* 45 (2006) 2835–2856.
- [28] P.J. Stephens, *J. Phys. Chem.* 52 (1970) 3489–3516.
- [29] S.B. Piepho, P.N. Schatz, *Group Theory in Spectroscopy with Applications in Magnetic Circular Dichroism*, John Wiley & Sons, New York, 1983.
- [30] M. Gouterman, *The Porphyrins*, Vol. III, Part A, in: D.H. Dolphin (Ed.), Academic Press, New York, 1979, pp. 1–156.
- [31] N. Lehnert, *The Smallest Biomolecules: Diatomics and their Interactions with Heme Proteins*, in: A. Ghosh (Ed.), Elsevier, Amsterdam, 2008, pp. 147–171.
- [32] T.G. Spiro, T.C. Streckas, *Proc. Natl Acad. Sci. USA* 69 (1972) 2622–2626.
- [33] M.G.I. Galinato, T. Spolidakis, D.P. Ballou, N. Lehnert, *Biochemistry* 50 (2011) 1053–1069.
- [34] M. Sono, M.P. Roach, E.D. Coulter, J.H. Dawson, *Chem. Rev.* 96 (1996) 2841–2887.
- [35] R. Tsai, C.A. Yu, I.C. Gunsalus, J. Peisach, W. Blumberg, W.H. Orme-Johnson, H. Beinert, *Proc. Natl Acad. Sci. USA* 66 (1970) 1157–1163.
- [36] F. Paulat, N. Lehnert, *Inorg. Chem.* 46 (2007) 1547–1549.
- [37] S. Nagano, T. Tosha, K. Ishimori, I. Morishima, T.L. Poulos, *J. Biochem. Chem.* 279 (2004) 42844–42849.
- [38] J.H. Dawson, R.H. Holm, J.R. Trudell, G. Barth, R.E. Linder, E. Bunnenberg, C. Djerassi, S.C. Tang, *J. Am. Chem. Soc.* 98 (1976) 3707–3709.
- [39] T.L. Poulos, J. Cupp-Vickery, H. Li, *Cytochrome P450 Structure, Mechanism, and Biochemistry*, Plenum Press, New York, 1995.
- [40] T.L. Poulos, *J. Biol. Inorg. Chem.* 1 (1996) 356–359.
- [41] J. Peisach, W.E. Blumberg, A. Adler, *Ann. N. Y. Acad. Sci.* 206 (1973) 310–327.
- [42] P. Nicholls, *Biochim. Biophys. Acta* 60 (1962) 217–225.
- [43] T. Mincey, T.G. Traylor, *J. Am. Chem. Soc.* 101 (1979) 765–766.
- [44] J. Teraoka, T. Kitagawa, *Biochem. Biophys. Res. Commun.* 93 (1980) 694–700.
- [45] M. Morrison, G.R. Schonbaum, *Annu. Rev. Biochem.* 45 (1976) 861–888.
- [46] J. Peisach, *Ann. N. Y. Acad. Sci.* 244 (1975) 187–203.
- [47] J.S. Valentine, R.P. Sheridan, L.C. Allen, P.C. Kahn, *Proc. Natl Acad. Sci. USA* 76 (1979) 1009–1013.
- [48] V.K.K. Praneeth, C. Näther, G. Peters, N. Lehnert, *Inorg. Chem.* 45 (2006) 2795–2811.
- [49] V.K.K. Praneeth, F. Neese, N. Lehnert, *Inorg. Chem.* 44 (2005) 2570–2572.
- [50] N. Lehnert, J.T. Sage, N.J. Silvernail, W.R. Scheidt, E.E. Alp, W. Sturhahn, J. Zhao, *Inorg. Chem.* 49 (2010) 7197–7215.
- [51] L.E. Goodrich, F. Paulat, V.K.K. Praneeth, N. Lehnert, *Inorg. Chem.* 49 (2010) 6293–6316.
- [52] T.L. Poulos, B.C. Finzel, A.J. Howard, *J. Mol. Biol.* 195 (1987) 687–700.
- [53] A.J. Thomson, M.K. Johnson, *Biochem. J.* 191 (1980) 411–420.
- [54] A.J. Thomson, M.K. Johnson, C. Greenwood, P.E. Gooding, *Biochem. J.* 193 (1981) 687–697.
- [55] W.R. Browett, Z. Gasyna, M.J. Stillman, *J. Am. Chem. Soc.* 110 (1988) 3633–3640.